COASTAL HAZARD ANALYSIS AT SAN ONOFRE NUCLEAR GENERATING STATION

Part 3: Tsunami Hazards



for

SOUTHERN CALIFORNIA EDISON
P.O. Box 128, MS D3D
5000 Pacific Coast Highway
San Clemente, CA 92672

Coastal Environments, Inc.
2166 Avenida de la Playa, Suite E
La Jolla, CA 92037

CE Reference No. 22-04
31 March 2022

TABLE OF CONTENTS

EXECUTIVE SUMMARY ..... **v**

1.0 INTRODUCTION **1**

2.0 PREVIOUS WORK **1**
- **2.1 HOUSTON AND GARCIA (1974)** **2**
- **2.2 INUNDATION COMPUTATIONS** **5**
- **2.3 USLU (2008)** **6**
- **2.4 THE SHI ET AL. (2016) SONGS REPORT** **7**

3.0 NUMERICAL MODELING PROGRAM **8**

4.0 TSUNAMI HAZARD TERMINOLOGY **9**

5.0 SEISMIC SOURCE DEFINITIONS **10**

6.0 NUMERICAL MODEL **11**
- **6.1 NUMERICAL MODELING BOUNDARY CONDITIONS** **11**
- **6.2 NUMERICAL MODELING INITIAL CONDITIONS** **11**

7.0 INPUT DATA **13**
- **7.1 EXTREME WATER LEVEL** **13**
- **7.2 NUMERICAL GRIDS** **13**
- **7.3 NOAA TSUNAMI UNIT SOURCES DATABASE** **14**
- **7.4 FAR-FIELD SEISMIC SOURCES** **15**
  - 7.4.1 Unit source sensitivity study 15
  - 7.4.2 Source specification 15
- **7.5 NEAR-FIELD SEISMIC SOURCES** **17**

8.0 COMPUTATIONS **33**
- **8.1 RESULTS FOR FAR-FIELD SEISMIC TSUNAMI CASES** **33**
  - 8.1.1 Eastern Aleutians 33
  - 8.1.2 Kuril Islands 35
- **8.2 RESULTS FOR LOCAL SEISMIC TSUNAMI CASES** **37**
  - 8.2.1 Source Local-sc1 37
  - 8.2.2 Source Local-sc2 37
  - 8.2.3 Source Local-sc3 38

9.0 RESULTS SUMMARY **61**

10.0 ABBREVIATIONS **62**

11.0 REFERENCES **63**

LIST OF APPENDICES

Appendix A. NOAA/PMEL Unit Source Parameters A-1

LIST OF TABLES

Table 2-1. 100-and 500-year tsunami runup* heights at San Onofre as computed by Houston and Garcia (1974) 4
Table 2-2. 100-and 500-year tsunami runup* heights at San Onofre as computed by Houston (1980) 5
Table 2-3. Maximum wave runup at San Onofre for earthquake- and landslide-generated tsunamis in southern California computed by Borrero et al. (2004) 5
Table 2-4. Wave height return periods for a numerical wave gauge offshore of San Diego, values from Uslu (2008) 7
Table 7-1. Bathymetry/topography numerical grids used for the hydrodynamic simulations 19
Table 7-2. Subduction zone 4-letter labeling used for the NOAA tsunami unit sources by Arcas (2015) 19
Table 7-3. Source specification for the far-field seismic scenarios modeled in this report 20
Table 7-4. Near-field fault parameters for the elastic dislocation model tsunami source 21
Table 7-5. Near-field composite seismic sources 21
Table 9-1. Table of maximum and minimum amplitudes occurring at the node offshore the SONGS site, and the maximum tsunami elevation and flow depth values inside the NUHOMS polygon for all simulated tsunami events 61

Table A-1. Earthquake parameters for the Aleutian-Alaska-Cascadia Subduction Zone NOAA/PMEL unit sources A-2
Table A-2. Earthquake parameters for the Kamchatka-Kuril-Japan-Izu-Mariana-Yap Subduction Zone NOAA/PMEL unit sources A-5

LIST OF FIGURES

Figure 4-1. Tsunami hazard terminology used to describe the computational results in this report 9
Figure 7-1. The Pacific Ocean bathymetry grid (grid *P*) of 4 arc-min spatial resolution used with MOST for the far-field tsunami simulations 22
Figure 7-2. Nested grids of increasing resolution used for the numerical computations 23
Figure 7-3. NOAA/PMEL's unit sources and labeling along the Japan subduction zone 24
Figure 7-4. Tsunami hazard sensitivity for the study site to the location of the unit sources 25

Figure 7-5. Definition of the five Eastern Aleutian (far-field) seismic sources using NOAA/PMEL's unit sources 26
Figure 7-6. Vertical seismic displacement for the Eastern Aleutian (far-field) seismic sources....27
Figure 7-7. Definition of the two Kuril (far-field) seismic sources using NOAA/PMEL's unit sources 28
Figure 7-8. Vertical co-seismic displacement for the two Kuril (far-field) seismic sources....28
Figure 7-9. Map showing seafloor deformation produced by local tsunami source 1 with all nine fault segments, with bathymetry and relocated seismicity 29
Figure 7-10. Map comparing rupture model for the 2016 Kaikoura, New Zealand earthquake with the Coastal Fault System located between Los Angeles and San Diego 30
Figure 7-11. Maps showing the simple rectangular fault models for the local tsunami cases 31
Figure 7-12. Vertical co-seismic displacement for the three composite near-field sources....32
Figure 8-1. Maps showing the maximum tsunami amplitudes (in part of the spatial extent) of grid *P* from the numerical simulation of all five Eastern Aleutian sources....39
Figure 8-2. Maps showing the maximum tsunami amplitudes inside the domains of grids AA, A, and B during the numerical simulation of the Eastern Aleutian source EA-sc1 40
Figure 8-3. Numerical simulation results for the Eastern Aleutian seismic source EA-sc1....41
Figure 8-4. Maps showing the maximum tsunami amplitudes inside the domains of grids AA, A, and B during the numerical simulation of the Eastern Aleutian source EA-sc2 42
Figure 8-5. Numerical simulation results for the Eastern Aleutian seismic source EA-sc2....43
Figure 8-6. Maps showing the maximum tsunami amplitudes inside the domains of grids AA, A, and B during the numerical simulation of the Eastern Aleutian source EA-sc3 44
Figure 8-7. Numerical simulation results for the Eastern Aleutian seismic source EA-sc3....45
Figure 8-8. Maps showing the maximum tsunami amplitudes inside the domains of grids AA, A, and B during the numerical simulation of the Eastern Aleutian source EA-sc4 46
Figure 8-9. Numerical simulation results for the Eastern Aleutian seismic source EA-sc4....47
Figure 8-10. Maps showing the maximum tsunami amplitudes inside the domains of grids AA, A, and B during the numerical simulation of the Eastern Aleutian source EA-sc5 48
Figure 8-11. Numerical simulation results for the Eastern Aleutian seismic source EA-sc5....49

Figure 8-12. Maps showing the maximum tsunami amplitudes (in part of the spatial extent) of grid *P* from the numerical simulation of all two Kuril sources 50
Figure 8-13. Maps showing the maximum tsunami amplitudes inside the domains of grids AA, A, and B during the numerical simulation of the Kuril source KU-sc1 51
Figure 8-14. Numerical simulation results for the Kuril seismic source KU-sc1 52
Figure 8-15. Maps showing the maximum tsunami amplitudes inside the domains of grids AA, A, and B during the numerical simulation of the Kuril source KU-sc2 53
Figure 8-16. Numerical simulation results for the Kuril seismic source KU-sc2 54
Figure 8-17. Maps showing the maximum tsunami amplitudes inside the domains of grids A and B during the numerical simulation of the near-field source Local-sc1 55
Figure 8-18. Numerical simulation results for the near-field seismic source Local-sc1 56
Figure 8-19. Maps showing the maximum tsunami amplitudes inside the domains of grids A and B during the numerical simulation of the near-field source Local-sc2 57
Figure 8-20. Numerical simulation results for the near-field seismic source Local-sc2 58
Figure 8-21. Maps showing the maximum tsunami amplitudes inside the domains of grids A and B during the numerical simulation of the near-field source Local-sc3 59
Figure 8-22. Numerical simulation results for the near-field seismic source Local-sc3 60

EXECUTIVE SUMMARY

The objective of this report is to assess tsunami hazards at the San Onofre Nuclear Generating Station (SONGS). Numerous cases are discussed in this study with the objective of determining the worst-case scenario. This study considered 10 extreme tsunami cases, seven generated in the far-field and three from near-field and local areas. The numerical results are summarized in Section 9 and Table 9-1. Full inundation simulations at high resolution were performed for the seven far-field and three local worst-case seismic sources. The simulations produced runup results that allow the evaluation of potential flooding at the site.

The analysis presented herein conservatively assumes that the SONGS seawall is not present, exposing the NIA at ground elevation of about 6.1 m (20 ft) MLLW. The numerical modeling initial conditions considered an extreme water level (EWL), which accounts for, among other things, the H++ scenario, as well as astronomical tides, storm surge, limited wave setup caused by breaking waves, and mean sea level rise in response to climate change. Based on that updated modeling, the EWL estimated for 2050 is 3.17 m (10.4 ft) MLLW.

The far-field tsunami cases were initially assessed by comparing the time series of amplitudes from the National Oceanic and Atmospheric Administration's Pacific Marine Environmental Laboratory (NOAA/PMEL) unit-source database at a location offshore of San Onofre. This far-field source sensitivity study shows which subduction zones produce the highest wave amplitudes near the site. Figure 7-4 suggests that the unit sources from the Alaska-Aleutians subduction zone produce the highest tsunami amplitudes offshore SONGS for M9.5 earthquake scenarios, since the high-amplitude source area in the eastern Aleutian region is the longest across all Pacific subduction zones. We have thus focused our attention on the eastern Aleutians to define the worst-case tsunami scenario and analyze five cases for the eastern Aleutian source area. Two sources from the Kuril Islands were also examined since Shi et al. (2016) showed that sources from the Kurils produced significant tsunami wave amplitudes at San Onofre. The largest tsunami amplitudes offshore and the main tsunami impact at the SONGS NUHOMS Independent Spent Fuel Storage Installation (ISFSI) originates in the eastern Aleutians from source EA-sc3. This produces a tsunami elevation of 9.1 m (MLLW), and flow depth of 2.8 m around the NUHOMS ISFSI, respectively. A description of all far-field sources considered in this study is given in Section 7.4.2. The results for far-field seismic tsunami simulations are discussed in Section 8.1.

Near-field seismic tsunami generation can mainly occur in the Coastal Fault System (CFS), as detailed in Part II of this report. The CFS stretches from Santa Monica to northern Baja California, Mexico. The northern section from Santa Monica to San Diego is well mapped, but the southern part to Punta Banda, Mexico where the Agua Blanca fault passes offshore, with similar faulting, is poorly mapped (e.g., Legg, 1985). A nine-segment model representing the prominent offshore fault sections between Dana Point and La Jolla was used to evaluate the local tsunami potential at the SONGS ISFSI (Table 7-4). The largest local earthquake scenario consists of all nine segments (Table 7-5, source Local-sc1,). Two other composite source models used the four segments of the Newport-Inglewood and Oceanside (Rose Canyon) strike-slip fault, with oblique-slip on the north and south segments of the South Coast Offshore fault (Table 7-5, source Local-sc3), and the San Mateo-San Onofre-Carlsbad oblique-reverse fault, with

strike-slip on the San Onofre segment (Table 7-5, source Local-sc2). From the three highest-case local seismic sources considered, source Local-sc1 produces the highest tsunami at the NUHOMS ISFSI, with maximum elevation of 7.2 m (MLLW), and maximum flow depth of 1.2 m.

Geopentech (2010) provides an extensive discussion of potential sub-marine landslide tsunami sources in southern California. Two potentially large sources were analyzed based on screening carried out in Geopentech (2010). These included a slide from the Thirtymile Bank formation landward into the San Diego Trough, and from the Fortymile Bank formation into North San Clemente Basin. Geopentech (2010) simulations of tsunami runup at the SONGS seawall was significantly higher for these two sources than for other potential offshore landslide locations considered, which produced height three to 10 times smaller. Shi et al. (2016) likewise considered the Thirtymile Bank and Fortymile Bank sources and estimated high water elevations at the San Onofre cliffs adjacent to SONGS. The results were 6.6 m (MLLW) for Thirtymile Bank, and 5.7 m (MLLW) for Fortymile Bank, also smaller than the present analysis. Both of these elevations imply insignificant flooding at the surface grade elevation of the NUHOMS ISFSI.

Based on a review of these earthquake and landslide scenarios, the worst-case hypothetical tsunami would be if a magnitude 9.53 earthquake occurred in the eastern Aleutians and the tsunami source was distributed along the entire subduction zone. For that event, the maximum potential water elevation at the SONGS site would be 9.08 m (29.8 ft) MLLW, with flow depth (i.e., water depth above ground surface) of 2.77 m (9.1 ft) around the NUHOMS ISFSI. The extreme case water level of 9.08 m (29.8 ft) MLLW would be 0.49 m (1.6 ft) greater than the 8.59 m (28.2 ft) MLLW elevation for the top of the existing NIA seawall, but would be below the top of the NUHOMS ISFSI concrete module height of 9.91 m (32.5 ft) MLLW.

The flow depth elevation analyzed in the new extreme hypothetical scenario of 9.08 m (29.8 ft) MLLW is lower than the top elevation of the NUHOMS ISFSI of 9.91 m (32.5 ft) MLLW by about 0.82 m (2.7 ft), and much lower than the NUHOMS ISFSI water submergence design depth of 15.24 m (50 ft). Moreover, although the NIA seawall was conservatively assumed not present for the updated tsunami propagation model, the continued presence of the NIA seawall at elevation 8.59 m (28.2 ft) MLLW reduces or eliminates the exposure of the NUHOMS ISFSI to most of the worst-case projected tsunami hazards from near and far-field sources. Further, as acknowledged in the Coastal Commission's 2001 Adopted Findings, inundation has been factored into the ISFSI design, and it would not adversely affect the stability of the site.

As part of this analysis, Coastal Environments has reviewed the 2001 and 2015 SONGS ISFSI Coastal Development Permit (CDP) and staff report materials and found that the Coastal Commission's conclusions in those reports remain correct.

COASTAL HAZARD ANALYSIS AT SAN ONOFRE NUCLEAR GENERATING STATION

Part 3: Tsunami Hazards

1.0 INTRODUCTION

This is a report to assess the hazards at the San Onofre Nuclear Generating Station (SONGS) located in California, from earthquake-generated tsunamis. The analysis was done through deterministic worst-case scenarios, both for far-field and near-field tsunamis. Maximum magnitude far-field earthquake scenarios along the Pacific subduction zones were designed based on recent studies. The far-field tsunami impact on SONGS was initially assessed by comparing the time series of pre-computed tsunami amplitudes from the NOAA/PMEL unit-source database, in a location offshore of the SONGS site. Near-field tsunami earthquake sources were re-evaluated from existing studies, and new worst-case scenarios were introduced. In all cases, the scenarios exceeded earlier estimates. Full inundation simulations at high resolution were performed for seven far-field and three local worst-case seismic sources. The simulations produced runup results, which allow the evaluation of potential flooding at the site.

2.0 PREVIOUS WORK

In performing any hazard assessment, the first step is to examine the available historic record in catalogs or scientific publications. California is believed to have a long history of tsunamis, although few had been historically documented before 1992.

The first comprehensive calculation of tsunami hazards for California is the work of Houston and Garcia (1974) and of Houston (1980). Both reports focused on the hazard in southern California from far-field events. McCulloch (1985) focused on the hazards in the Los Angeles region primarily from far-field events, but also considered several local events. Following the 1992 magnitude 7.1 Cape Mendocino earthquake, which triggered an about 1 m tsunami, McCarthy et al. (1993) analyzed the historic records of tsunamis in California and assessed very qualitatively the hazard over the entire State.

Synolakis et al. (1998) reviewed pre-1997 studies and observed that the earlier runup estimates did not include inundation calculations. When performed with the newer generation of inundation models available then, runup estimates were up to 100% higher than what the earlier calculations suggested, depending on the nearshore topography. Borrero et al. (2001) studied nearshore tectonic, landslide and slump sources in East Santa Barbara Channel and produced runup estimates ranging from 2 m to 13 m in Santa Barbara County.

Eisner et al. (2001) argued that California presents nontrivial challenges for assessing tsunami hazards, including a short historic record and the possibility of nearshore events with less than 20 min propagation times to the target coastlines. More specifically, whereas in Japan and in Greece over 1,000-year historic records exist, in California there are no known tsunami records before the 19th century, except the 1700 Cascadia tsunami. Several tsunamis have been reported since 1800, but in most cases the information is not sufficient for reasonable inferences

of the inundation. Quantitative measurements of inundation exist for the 1964 Alaskan tsunami and for most post-2010 transpacific tsunamis that have been recorded in tide gages, but none appear to exist for SONGS.

Legg et al. (2004) examined tsunami hazards associated with the Catalina fault. Several earthquake scenarios with moment magnitudes ranging between 7.0 and 7.6 were used as initial conditions for tsunami simulations, and up to 4 m runup was predicted along the southern California coastline. Barberopoulou et al. (2011) assessed tsunami hazards in San Diego Bay, California, using what was then recently identified offshore tsunami sources and recently available high resolution bathymetric/topographic data.

As a preamble, and following Synolakis et al. (2001), it is important to define the terms runup and inundation, which are sometimes misused (also see Section 4.0). Wave runup is the rush of water up a structure or a beach; it is also called the uprush. The maximum runup is the vertical height above still water (or the initial position of the shoreline) that the rush of water reaches to, as it climbs onshore. The term inundation height is a term sometimes used interchangeably with runup, but other times it refers to either the maximum flow depth or runup along a particular transect. The term tsunami elevation is the local height the tsunami flood reaches with respect to the datum, defined by the initial position of the shoreline.

Often in the field, it is hard to identify tsunami elevations at more than one location, although of course they can be computed everywhere. Specific knowledge of the maximum wave runup on a given beach is essential both in shore protection and in the design of coastal structures. In earlier pre-1990s studies the term tsunami height offshore was used interchangeably with the maximum runup height. References to offshore tsunami heights are generally not useful in inundation predictions as the tsunami height varies substantially with depth, particularly in the extreme nearshore region.

Inundation refers to the horizontal distance the wave penetrates inland. Depending on land use, either runup or inundation are relevant, and most often both. An inundation map includes a line corresponding to the maximum penetration of the tsunami wave triggered by the event under study.

Here, the most extensive historic studies for tsunami hazards in southern California are briefly summarized.

2.1 HOUSTON AND GARCIA (1974)

The earliest comprehensive attempt of quantifying the tsunami hazard in California is by Houston and Garcia (1974). They performed a Probabilistic Tsunami Hazard Assessment (PTHA) study to establish the 100- and 500-year tsunami runup elevations on the west coast of the US by far-field earthquake sources. Due to the limited historical data of tsunami activity on the west coast (at the time of the report), the authors identified tsunamigenic earthquakes only emanating from the Alaska-Aleutian and South America subduction zones.

The tsunamigenic potential of the Cascadia subduction zone was not known at that time, which would have considerably changed the outcome of their study. They only considered two

subduction zones to generate tsunamis which they propagated through the Pacific Ocean using a linear shallow-water numerical code and coarse bathymetric grid (20 arc-min). The coarse grid tsunami propagation calculations were stopped at 500 m depth.

Then, a non-linear model and finer grid resolution (2 miles cell size) was used to propagate tsunamis from the deep ocean over the continental slope and shelf to a vertical-wall coast. (Back then, neither the analysis or the computational power existed to perform inundation computations and predict the wave runup, see Synolakis (2003) for a discussion of the evolution of tsunami inundation computations). The nearshore grids extended to one and a half wavelengths of a 30-min period wave from the shore, so that at least three typical tsunami waves could propagate to the shore before being reflected from the boundary.

As written above, inland inundation computations were not performed, and the term "runup" in Houston and Garcia (1974) actually corresponds to the tsunami elevation at the initial position of the shoreline. Titov and Synolakis (1998) showed that models which do not perform runup/inundation calculations, a.k.a. *threshold models*, have significant discrepancies compared to models which compute inundation. Yet, threshold models were standard before the development of more advanced hydrodynamic models and the availability of more computational power. Even today (Spring 2022), some engineering studies are still performed by threshold models simply because the design firms or their consultants are either not aware or have no access to inundation models (Synolakis and Kânoğlu, 2015).

Houston and Garcia (1974) discretized the Alaska-Aleutian subduction zone (AASZ) into 12 segments, and the South America subduction zone (SASZ) into three. The finer discretization of the AASZ was due to the realization that the US West Coast tsunami hazard is more sensitive to the location of AASZ earthquakes rather than the location of earthquakes generated in the SASZ.

The initial conditions for the propagation computations were approximated by ellipses of uplift, with the ellipse major axis parallel to the trench and the spatial size held constant and independent of what they referred to as tsunami intensity. This was standard back then, as there was no understanding of the dipolar nature of the seafloor motion associated with earthquakes. In each of the segments of AASZ and SASZ, Houston and Garcia (1974) generated tsunamis of "intensities" from 2 to 5 in increments of 0.5 (105 sources in total), where the intensity (i) is given by (Soloviev, 1970):

$$i = log_2(\ \overline{2}H_{avg}) \tag{2-1}$$

where H_{avg} is the average runup over a coast segment considered as appropriate. The probability $n(i)$ of a certain tsunami intensity i being generated during any given year is given by the following expression:

$$n\ i\ = p_1 e^{p_2 i} \tag{2-2}$$

where p_1 and p_2 are empirical parameters which were estimated as $p_1 = 0.074$, $p_2 = -0.63$ and $p_1 = 0.113$, $p_2 = -0.71$ for SASZ and AASZ respectively, with these parameters being uniformly applicable along each trench.

Post the 1992 Nicaraguan tsunami, the concept of the tsunami intensity as derived from historic reports has been debunked, because it was observed that runup can vary substantially over adjacent beaches, begging the question of how to define an appropriate segment in real coastlines with substantial cross shore variations. As Ambraseys and Synolakis (2010) pointed out, "The only justification for ever using an intensity scale is to quantify information in a single index from various historic sources, for the purposes of comparison of effects of different earthquakes in the same locale. Hydrodynamic computational models provide detailed geographic distributions of inundation heights, overland flow depths and flow velocities, allowing for a comprehensive determination of risk."

Each of the 105 sources of variable location and tsunami intensity produced 2-hr time series along the US west coast. The time-series were extended to 24 hr. by adding a sinusoidal signal with amplitude 40% that of the maximum amplitude of the modeled time-series. Astronomical tidal variation at each coastal cell was calculated from available data for the year 1964, during which modal factors are near their average values of the 18.6-year cycle. The tidal signal was calculated with a 15 min time interval. The 24-hr tsunami time-series was then linearly superimposed to the tidal signal, varying the starting time (shifting the starting time by 15 min at each iteration). The maximum amplitude of the combined tsunami and tidal signal was assigned a probability equal to the probability of the tsunami with intensity *i* occurring and the probability of the waves arriving at that particular 15 min period of the yearly tidal cycle.

Maximum elevations at the shoreline and their corresponding probabilities of occurrence were re-organized in descending order for each coastal location. The probabilities were summed (from smaller to larger) until the desired probability *P* was reached, which corresponds to the return period $T=1/P$. Table 2-1 shows the resulting 100- and 500-year tsunami runup heights at San Onofre.

Table 2-1. 100-and 500-year tsunami runup* heights at San Onofre as computed by Houston and Garcia (1974). Values in the report are in *ft* and were converted to *m*.

100-year "runup"* (m)	500-year "runup"* (m)
1.74	3.38

*see how runup is defined in Houston and Garcia (1974).

Houston (1980) later updated the 100- and 500-year tsunami wave heights, for the southern California coastal stretch from Point Conception to Ensenada, Mexico. He used a different numerical model for nearshore computations, which allowed for variable spatial size. He modeled only large earthquake sources (initial wavelengths greater than 100 miles) to justify the use of a linear non-dispersive shallow water model for the trans-Pacific wave propagation. Table 2-2 shows the resulting 100- and 500-year tsunami runup heights at San Onofre.

Table 2-2. 100-and 500-year tsunami runup* heights at San Onofre as computed by Houston (1980). Values in the report (for gage 152, plate 76 in the report) are in *ft* and were converted to *m*.

100-year "Runup"* (m)	500-year "Runup"* (m)
1.18	1.43

*see how runup is defined in Houston (1980).

2.2 INUNDATION COMPUTATIONS

The breakthrough in terms of tsunami hazard assessment came in the 1990s with advancement in numerical models and the capability of computing onland inundation and runup (see Synolakis and Bernard 2006 for details in the development of hydrodynamic codes). Based on excellent comparisons between numerical and field runup data for the 1993 Hokkaido-Nansei-Oki tsunami in Japan (Titov and Synolakis, 1997), as well as comparisons of model predictions with laboratory measurements by Titov and Synolakis (1995, 1998), the contemporary state-of-the-art methodology for estimating tsunami risk from near- and far-field for California was set.

Following the 1998 Papua New Guinea tsunami (Synolakis et al., 2002a), the tsunami hazard potential of submarine landslides was re-discovered. In light of those new findings and with more detailed information about the local tectonic setting and bathymetry off southern California, Borrero et al. (2001), Borrero (2002) and Borrero et al. (2004) examined the tsunamigenic potential of local earthquakes and landslides in southern California; the wave runup values at San Onofre for the earthquake and landslide scenarios considered by Borrero et al. (2004) are shown in Table 2-3. The local sources database was incorporated in preparing the first- and second-generation tsunami inundation maps used for evacuation planning for California (Eisner et al., 2001; Barberopoulou et al., 2009, 2011).

Table 2-3. Maximum wave runup at San Onofre for earthquake- and landslide-generated tsunamis in southern California computed by Borrero et al. (2004) - runup data is inferred from Figure 2 of Borrero et al. (2004).

Source Name	M_w	Maximum Runup (m)
Earthquake Scenarios		
Santa Catalina	7.6	1.0
Lasuen Knoll	7.1	1.0
San Mateo Thrust	7.0	4.2
Landslide Scenarios		
Palos Verdes Slide 1	--	0.3
Palos Verdes Slide 2	--	0.3

In the first decade of the 21st century, tsunamis generated around the world allowed for validation of computational models (Synolakis et al., 2008). Major advances in numerical codes and computational power and the availability of higher resolution bathymetric and topographic data allowed for full inundation computations for design earthquake scenarios with unprecedented accuracy. Also, geological studies re-evaluated the tsunamigenic potential of subduction zones by identifying tsunami evidence in the field and linking them to historical

tsunami records. Through these studies, new tsunami events with long return periods were added to the tsunami catalogs.

The most important finding concerning the tsunami hazard of California is the 1700 trans-Pacific tsunami that originated from the Cascadia Subduction Zone (CSZ) (Atwater et al., 2016). Even though it had been identified as an event in the Japanese tsunami records, with ~3 m maximum tsunami height (Satake et al., 1996), its source was not local, and it remained unidentified until the work of Atwater (1987) and Satake et al. (1996).

2.3 USLU (2008)

Uslu (2008), in his PhD thesis entitled, "Deterministic And Probabilistic Tsunami Studies In California From Near-Field And Far-Field Sources," used all potential tsunami sources known until then, applying high-resolution bathymetric/topographic data and a validated numerical code with full inundation computation capabilities.

In the deterministic part of his work, Uslu (2008) modeled tsunami scenarios for San Francisco Bay, Crescent City and Humboldt Bay to re-evaluate tsunami hazard for each location. For the far-field sources (sources located at distance greater that 1800 km travelling at depths >1 km, he took advantage of the FACTS (Facility for the Analysis and Comparison of Tsunami Simulations) tsunami sources database of NOAA/PMEL and designed new, composite scenarios of tsunami sources. Based on source directivity and on evidence of past tsunami events in California, he only included the Alaska-Aleutian, Kurils-Japan and South American subduction zones in the analysis. The only historical events included were the Chile 1960 and Alaska 1964 earthquakes. The rest of his far-field sources were plausible scenarios with moment and slip magnitudes ranging from M_w 8.7-9.4 and 5-25 m, respectively.

In the near-field, he put together a list of potential tsunamigenic earthquake sources in California and Cascadia that had been published until then. For Cascadia, six different scenarios were included with earthquake moment magnitudes ranging between M_w 8.44-9.02. The rest of the local earthquake sources were on faults in central and southern California and San Francisco Bay with M_w ranging 6.6-7.66. The latter are threats only for near-field coastal locales. Finally, he considered three landslide sources, two in southern California (Goleta and Palos Verdes, Borrero et al., 2001) and one in San Francisco Bay (Farallon Islands). The landslide sources were implemented using static dipole-shaped initial conditions, per Borrero (2001) and Synolakis et al. (2002a).

For the probabilistic part of his work, Uslu (2008) generated tsunami sources in the Kuril, West and East Aleutian, Central and South American subduction zones. Each subduction zone was discretized in a number of segments along its (along-strike) length, and 20 earthquake scenarios (of magnitudes ranging between M_w 7.65-9.3) were fit in each segment, resulting in hundreds of runs for each subduction zone. All the earthquake scenarios were implemented as combinations of FACTS sources, for which the amplitudes across the Pacific Ocean had been precomputed. For each run, the maximum wave height was evaluated just offshore seven locations across California, with local depth varying between 31-448 m. The nearest locations to SONGS in Uslu (2008) are in Los Angeles and San Diego.

In computing the return period of certain offshore wave heights, Uslu (2008) employed both time-dependent and time-independent probabilistic hazard assessment methodologies (Table 2-4). In the time-independent seismic hazard assessment methodology, the memory-less Poisson distribution was employed, where subduction zones have no memory of past seismicity.

Table 2-4. Wave height return periods for a numerical wave gauge offshore of San Diego (at coordinates: 242.68^{o}E 32.713^{o}N and local depth 83 m), values from Uslu (2008).

Wave Height (m)	0.50	1.00	1.50
Time-independent return period (yrs.)	67	218	335
Time-dependent return period (yrs.)	52	189	360

Uslu (2008) went further with his analysis and resolved the nearshore hydrodynamics of each scenario at three harbors, Crescent City, San Francisco and Los Angeles, using the MOST model (see Section 6.0 for model description). The aforementioned probabilistic analysis was also performed for the three harbors. It was found that the tsunami risk in California decreases from north to south. The northern California coastline is more susceptible to tsunamis originating from the Alaska-Aleutians subduction zones, whereas southern California is exposed to tsunamis originating from the central and south American subduction zones as well as from Alaska-Aleutians. Landslide scenarios were not considered in Uslu's probabilistic analysis.

Barberopoulou et al. (2011) considered far-field and near-field sources, including landslides from the Coronado Canyon and Thirtymile Bank to reassess the tsunami hazard in San Diego bay. None of their earthquake or slide scenarios exceeded 4 m wave runup, although they noted that the Strand - the spit fronting San Diego Bay - would experience overland flooding. The Coronado Canyon slide as examined directed large waves further south of the harbor mouth.

2.4 THE SHI ET AL. (2016) SONGS REPORT

Shi et al. (2016) did another analysis of tsunami hazards at SONGS including far-field and near-field earthquake tsunamis and landslides tsunamis, as provided by Geopentech (2010). They did not include the historical analysis provided by these studies in the report.

In terms of far-field sources, Shi et al. (2016) considered sources in the Eastern and Western Aleutians, in the Kurils and in Chile. They did not perform a sensitivity analysis to examine how other possible source combinations around the Pacific might result in higher amplification at the site - such analysis is standard, at least since Uslu (2008). For due diligence, one would have to consider sources around the Pacific rim, refer to the consequences of not doing so in Synolakis and Kânoğlu (2015). It shows the wave height just offshore at Fukushima, Japan from unit sources around the Pacific, and indicates that the wave height from other sources is comparable to that from the one source they considered in Chile. While sources in Alaska may have the highest impact, one cannot possibly expect *a priori* and without analysis that all the other subduction zones in the world may have less impact on the site, than Alaska. Such analysis is performed in this report in Section 7.4.1 (Figure 7-4).

3.0 NUMERICAL MODELING PROGRAM

Program Name: Method of Splitting Tsunamis (MOST).

Program Revision: v4, last revised by NOAA/PMEL on 1/10/2012.

Computer Type and Description: Apple Mac Mini (2018) personal computer,3 GHz Intel Core i5 processor, 8 GB memory.

Computer Program Validated: Yes.

Model Validation References: Titov and Synolakis (1995, 1997, 1998).

4.0 TSUNAMI HAZARD TERMINOLOGY

The following terminology is used to describe the computational results in this report (see Figure 4-1):

- Runup (or runup elevation): the elevation above the still water level at the furthest inland location reached by the waves.
- Inundation distance: the horizontal distance between the shoreline (corresponding to the still water level) and the furthest inland point reached by the waves.
- Tsunami elevation: the vertical difference between the wave amplitude (over land) and the still water level.
- Flow depth: the vertical difference between the wave amplitude (over land) and the ground.

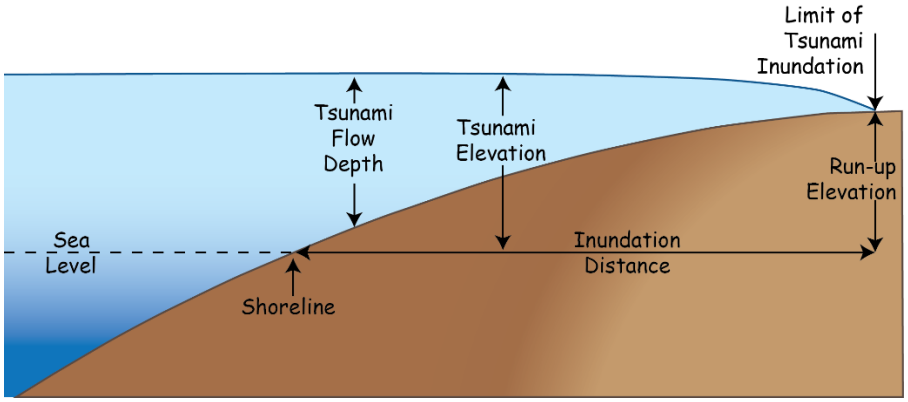


Figure 4-1. Tsunami hazard terminology used to describe the computational results in this report (Source: http://ds.iris.edu/aed2/c/alaska/popups/tsunamis/tsu_1.html).

5.0 SEISMIC SOURCE DEFINITIONS

This section lists a number of parameters used to define the seismic source. The seismic moment M_0 is a measure of the energy released by an earthquake. The seismic moment is defined as:

$$M_0 = \mu L W \Delta u, \tag{5-1}$$

where μ is the elastic modulus of elasticity, L is the fault rupture length, W is the fault rupture width, and Δu is the slip magnitude (i.e., the distance covered by the relative motion between the two fault planes during the seismic rupture). In the cases of composite sources (seismic sources composed of individual sub faults), the seismic moment of the composite source ($M_{0,comp}$) is the sum of the seismic moments of the N individual sub faults ($M_{0,i}$):

$$M_{0,comp} = \sum_{i}^{N} M_{0,i} \tag{5-2}$$

The moment magnitude M_w is a measure of the magnitude of an earthquake based on the seismic moment. The moment magnitude is expressed as (Hanks and Kanamori, 1979):

$$Mw = (2/3) \log_{10} (M_0) - 10.7, \tag{5-3}$$

where the seismic moment M_0 is expressed in *dyne cm* (10^{-7} *N m*).

6.0 NUMERICAL MODEL

The results from the numerical simulations presented in this report were produced using the MOST (Method Of Splitting Tsunamis) model (Titov and Synolakis, 1995, 1998). MOST has been extensively validated and used for tsunami hazard assessments in the United States and is currently maintained and in operational use at NOAA/PMEL. Variants of MOST have been in continuous use for tsunami hazard assessments in California, since the mid 1990's (Titov et al., 2016).

MOST solves the 2+1 Nonlinear Shallow Water equations (Titov and Synolakis, 1995, 1998):

$$h_t + (uh)_x + (vh)_y = 0, \tag{6-1}$$

$$u_t + uu_x + vu_y + gh_x = gd_x, \tag{6-2}$$

$$v_t + uv_x + vv_y + gh_y = gd_y, \tag{6-3}$$

where $h = \eta(x, y, t) + d(x, y, t)$, $\eta(x, y, t)$ =wave amplitude; $d = (x, y, t)$ =undisturbed water depth; $u(x, y, t)$ and $v(x, y, t)$ are the depth-averaged velocities along-longitude (x) and along-latitude (y), respectively. The governing equations are solved in characteristic form through an explicit finite difference scheme using the method of fractional steps of Janenko (1971).

6.1 NUMERICAL MODELING BOUNDARY CONDITIONS

Section 7.2 describes the nested numerical grids. Briefly, numerical computations were stopped at 5 m depth in grids P, AA and A, at which depth waves are reflected back (solid wall boundary condition). Runup and inundation computations were only performed in grids B and C, for which a moving boundary condition was used as described in Titov and Synolakis (1995). For runup/inundation computations, a bottom friction term is included in the momentum equations using a Manning's roughness coefficient of $n = 0.03$ s/m$^{1/3}$ which corresponds to a weedy earth channel surface material.

The hydrodynamic information (free surface elevation η and the two depth-averaged velocity components u, v along the longitude and latitude, respectively) were passed from the domain of the coarser-resolution grids to the boundaries of the finer-resolution numerical grids. An absorbing boundary condition was applied at the open (sea) boundaries of the numerical grids.

6.2 NUMERICAL MODELING INITIAL CONDITIONS

The initial conditions of the hydrodynamic simulations presented in this report are defined by the co-seismic seafloor deformation. Fault ruptures due to earthquakes deform the surface of the earth in all three Cartesian components. The surface deformation due to finite rectangular faults is computed through the analytical equations of Okada (1985) in an elastic half-space, implemented through the Matlab code of Beauducel (2011). The inputs for the Okada (1985) analytical equations are the fault rupture location (longitude, latitude), depth of the

rupture, the fault rupture dimensions (length L and width W), the slip magnitude (Δu), and the dip, rake and strike angles (see Aki and Richards, 1980, for definitions). The Matlab code output is the surface displacement in all three Cartesian components.

The vertical component of the seafloor deformation was directly translated to the free surface of the sea (Derakhti et al., 2019). This simplification is allowed since the seafloor rise speed due to the fault rupture is much faster compared to the speed of wave propagation. Numerical simulations were thus initiated using the vertical free surface deformation computed using the Okada (1985) analytic equations, with zero initial velocities.

In the cases of composite sources (seismic sources composed of individual subfaults), the vertical co-seismic deformation of the composite source was computed by adding the vertical deformation resulting from the rupture of the individual subfaults, i.e., the analytic equations of Okada (1985) were applied for each individual subfault rupture.

7.0 INPUT DATA

7.1 EXTREME WATER LEVEL

Water surface elevation is dependent on astronomical tides, storm surge, limited wave setup caused by breaking waves, and mean sea level rise (MSLR) in response to climate change. The 1% annual probability of exceedance extreme water level due to tides, storm surge and wave setup at La Jolla, CA, was estimated by the NOAA in 2018 (https://tidesandcurrents.noaa.gov/est/stickdiagram.shtml?stnid=9410230) as $h_{EWL,NOAA}$ = 2.37 m, MLLW (1.54 m, MSL). The sea level rise projection estimate by OPC (Ocean Protection Council) from 2000 to 2050 is h_{MSLR}=0.85 m (2.8 ft) (OPC, 2018). Since the NOAA estimate was published in 2018, we adjusted the projection of OPC to reflect the changes from 2018 to 2050 by $h_{MSLR,cor}$ = -0.045 m. The extreme water level (h_{EWL}) estimate for 2050, considering tides, storm surge, wave setup, MSLR is the sum of the NOAA extreme water level estimate in 2018 and the adjusted OPC estimate:

$$h_{\mathrm{EWL}} = h_{EWL,NOAA} + h_{MSLR} + h_{MSLR,cor} = 3.18 \text{ m, with respect to MLLW.} \quad (7\text{-}1)$$

7.2 NUMERICAL GRIDS

During shoaling, as the waves propagate unto shallower water the cell size of the numerical grid needs to be reduced to accurately resolve the steepening wave profiles (increasing non-linearity), and the decrease of the wavelength. In MOST, wave shoaling is accounted for by using nested grids of increasing spatial resolution.

For the far-field simulations, a bathymetry grid of 4 arc-min (~7421 m at equator; grid cell size varies along latitudes) resolution named grid P was used which is available with the ComMIT model (COMmunity Model Interface for Tsunami, Titov et al., 2011). The bathymetry grid (Figure 7-1) is based on the Smith and Sandwell (1994) 2 arc-min data. For the far-field simulations, also a 30 arc-sec (~779 m) bathymetry/topography grid named grid AA was used that covers the Channel Islands, Santa Monica Bay and San Pedro Bay (Figure 7-2*a*). The bathymetry/topography information was downloaded from the 2021 global dataset of the General Bathymetric Chart of the Oceans (GEBCO, 2021). The 15 arc-sec original dataset was sub-sampled to 30 arc-sec for the purposes of this study.

Another three nested grids were used with both far- and near-field sources, namely grids A, B and C. The coarsest grid (grid A) which covers the largest area has 6 arc-sec (~156 m) resolution, whereas the intermediate (grid B) and finest grids (grid C) have 1 arc-sec (~26 m) and 1/6 arc-sec (~4 m) spatial resolutions, respectively (Figure 7-2*b*-*d*). Grid A was built based on the 3 arc-sec NOAA/NGDC Coastal Relief Model for Southern California (NGDC, 2003), sub-sampled to 6 arc-sec. Grid B was built based on the San Diego 1/3 arc-sec NOAA/NGDC Tsunami Inundation Digital Elevation Model (NGDC, 2010), sub-sampled to 1 arc-sec.

Grid C is composed by two datasets, a 0.5 m resolution topobathymetry grid provided by the Coastal Environments firm (CE), and the 1/3 arc-sec San Diego NOAA/NGDC Tsunami Inundation Digital Elevation Model - the area covered by the 0.5 m resolution topobathymetry grids is denoted with the red polygon in Figure 7-2*d*. The bathymetry data of the 0.5 m resolution

topobathymetry grid is the result of merging two multibeam surveys carried out by Coastal Environment in 2016 with topobathymetry data downloaded from the NOAA website (https://www.fisheries.noaa.gov/inport/item/55359), prepared by the USGS Coastal National Elevation Database. The inland data of the CE grid derive from the 2016 Lidar[1] data that was combined with the 2008 Lidar data. The 2008 Lidar data were used to add the grade elevation of SONGS structures behind the existing seawall. The two (CE and NOAA/NGDC) high-resolution topobathymetry grids were combined to create grid C with a 1/6 arc-sec resolution.

In summary, five nested grids were used for the far-field numerical simulations (grids P, AA, A, B and C) and three nested grids were used for the near-field numerical simulations (grid A, B and C). The grid sizes, spatial extents and resolutions are summarized in Table 7-1. All the DEMs used for the numerical simulations were referenced to the design Extreme Water Level vertical datum (see Section 7.1) and the World Geodetic System of 1984 (WGS 84) horizontal datum, in spherical coordinates.

7.3 NOAA TSUNAMI UNIT SOURCES DATABASE

NOAA/PMELAs part of its real-time tsunami forecasting system, the NOAA/PMEL has discretized the circum-Pacific subduction-zones into sub-faults of size 100x50km (along-strike length x along-dip width). The sub-faults are prescribed a strike angle that follows the plate boundaries defined by Bird (2003). The dip angle and the down-dip extend of unit sources are based on the best knowledge of local fault geometry (e.g., Kirby, 2006). While the pre-defined fault geometry of the unit sources, i.e., dip and strike angles, is assumed to be accurately represented, it has also been shown by Titov et al. (1999) that these parameters do not have a big effect in the far-field tsunami amplitudes.

As an example, Figure 7-3 shows the sub-faults and the NOAA labeling for the Japan subduction zone. The numbers represent the source column number which runs along the subduction zone and the letters in front of the numbers represent the source row name in the down-dip direction. The rows go from shallowest to deepest in the following order: B, A, Z, Y, X, W, V. Source rows C and D represent normal faulting sources which were not considered in this report. Finally, the sources are assigned a four-lettered code, depending on which subduction zone they are part of (see Table 7-2).

For the purposes of tsunami modeling, rake angle is fixed at 90^{o}, thus representing pure thrust rupture. The surface deformation from the rupture of each sub-fault has been computed using the analytical equations of Okada (1985) for 1m slip magnitude, thus calling the sub-fault *unit* sources. The tsunami amplitudes and velocities across the Pacific basin were computed using MOST on a 4 arc-min grid and have been stored in an on-line database at 16 arc-min resolution.

Since surface deformation and deep-water propagation are linear functions of slip magnitude, the tsunami amplitudes across the Pacific Ocean can be readily obtained for any

[1] Light Detection and Ranging (Lidar), is a remote sensing method that uses light in the form of a pulsed laser to measure ranges (variable distances) to the Earth.

combination of unit-sources and slip magnitudes. Therefore, the variation of slip magnitude during seismic rupture can be accounted for by creating more complex faulting scenarios (Titov et al., 2011). This linear property of deep water tsunami propagation is the basis of NOAA's tsunami source inversion procedure during real time tsunami forecasts, which is described in more detail by Percival et al. (2009).

7.4 FAR-FIELD SEISMIC SOURCES

7.4.1 Unit source sensitivity study

SONGS is located along the coast of southern California and therefore only tsunami sources around the Pacific Ocean are considered. To identify which subduction zones around the Pacific direct more energy towards the study area, we performed a sensitivity analysis by utilizing the NOAA/PMEL unit sources database. The tsunami amplitude time series for each unit source are available at discrete nodes with 16arc-min spacing. We selected the closest node directly offshore from the SONGS site (see inset of Figure 7-4) and compared the maximum (positive) amplitude from each unit source. Figure 7-4 shows the maximum amplitude from all the row B (shallowest) unit sources considered here.

All unit sources have the same dimensions (100 x 50 km) and the same slip magnitude (1 m), and consequently have the same moment magnitude (assuming earth's rigidity μ is constant everywhere). Therefore, in this type of sensitivity test, earthquake magnitude is not per se important. Maximum amplitude varies between sources due to differences in location, fault geometry (dip angle), the distance from source to site, and the oceanic bathymetry/topography that refracts/reflects the waves and dictates where the tsunami energy is beamed towards (directivity). Consequently, it cannot be immediately concluded, without taking earthquake magnitudes into consideration, where the worst-case tsunami source for the study area is located.

From Figure 7-4 it is evident that the unit sources from the Alaska-Aleutians subduction zone produce the highest amplitudes offshore the SONGS site. The Alaska-Aleutians unit sources produce progressively higher maximum amplitudes near the site as we move from the Western to the Eastern Aleutians. The high-amplitude patch across the Eastern Aleutian sources is also the longest across all Pacific subduction zones. Attention thus focused on Eastern Aleutians in search of the worst-case tsunami scenario. Sources from the Kurils were also examined, since the Shi et al. (2016) report showed that sources from the Kurils produced significant wave amplitudes at the SONGS site. In the following section, we describe all the far-field sources considered in this study.

7.4.2 Source specification

The subduction zones located around the Pacific Rim produce great earthquakes along the subduction megathrust (M>8). The large vertical displacements of the seafloor generate tsunamis that propagate across the entire Pacific Ocean Basin, which may continue to oscillate back-and-forth for days (e.g., 22 May 1960 Chile (M_w9.5) earthquake, 27 March 1964 Alaska (M_w9.2) earthquake, and the 11 March 2011 Tohoku, Japan, (M_w9.0) earthquake). In addition, explosive volcanism produced by subduction processes in the volcanic arc may produce basin-wide tsunamis as recently observed from the 15 January 2022 Tonga (M_s5.8) explosive subsea

eruption. Assessments of tsunami hazards to southern California ports (Los Angeles and San Diego) determined that the Eastern Aleutians-Alaska region produced the greatest inundation hazards from Pacific Rim earthquake sources of M_w9.0 (Uslu, 2008; Barberopoulou et al., 2011; Thio et al., 2010; Kirby et al., 2013). Other significant distant sources include Chile and Kuril-Kamchatka regions where the shape of the subduction zone focuses the tsunami energy toward California. Here, we model five variations of the Eastern Aleutian-Alaska subduction source and two variations of the Kuril-Kamchatka subduction source to evaluate the range of inundation that may be expected for extreme M_w9.5 events.

The NOAA 100-km by 50-km unit sources were used to create the models. The magnitude, rupture area and slip magnitude of all the far-field sources modeled in this report are outlined in Table 7-3. The unit sources corresponding to each source are also provided using NOAA/PMEL's labels - the full list of parameters of all NOAA/PMEL unit sources used to define the far-field sources are provided in Tables A-1 and A-2 of Appendix A. The slip distribution across the unit sources for the Eastern Aleutians and Kurils far-field composite sources are depicted in Figures 7-5 and 7-6, respectively. The vertical co-seismic displacement fields used as initial conditions for the hydrodynamics simulations are shown in Figures 7-7 and 7-8 for the Eastern Aleutians and Kurils far-field sources, respectively.

Eastern Aleutians – Alaska subduction source regions include up to six rows of source patches in the down-dip direction and as many as 15 columns of patches parallel to the trench. The extra width in this region results from the shallow dip of the subduction which was demonstrated in the 1964 M_w9.2 Prince William Sound earthquake (Johnson et al., 1996). Source models were designed to address the issues of focusing tsunami energy by source geometry and tapered slip distributions, and distribution of high-slip areas that may increase runup and inundation at the SONGS location.

The magnitude of the design event was kept at the 9.5 level. A two-row by 15 column model with uniform 33.25-m slip for a 1500-km length by 100-km width rupture (source EA-sc3 in Table 7-3) was similar to the model used by Shi et al. (2016). For 800-km length ruptures with six rows (300-km width), both a uniform slip model (source EA-sc2 in Table 7-3) and two tapered models with the 20-m high-slip patches were created: one with the slip patch located deeper in the central part of the subduction zone (source EA-sc1 in Table 7-3), and the second with the patch near the trench (source EA-sc4 in Table 7-3). The fifth model used a 1000-km length with the six rows for 300-km width, and larger (30-40 m) slip patch closer to the trench (source EA-sc5 in Table 7-3).

The Kurils - Kamchatka models included one 1200-km by 100-km (two rows) uniform slip (41.57 m) version (source KU-sc1 in Table 7-3) and a second slip patch version with maximum slip of 50-60 meters near the northeast end of the subduction zone (source KU-sc2 in Table 7-3). The latter model was designed to focus energy toward California by putting the high-slip patches closer to Alaska and North America.

7.5 NEAR-FIELD SEISMIC SOURCES

Previous estimates of earthquake and tsunami hazards for the SONGS site considered large strike-slip earthquakes along the Newport-Inglewood (South Coast Offshore Zone of Deformation as described before 1981 NRC hearings) and the Rose Canyon fault continuation to the south. The strike-slip character at the time was considered unlikely to produce a significant tsunami. The Oceanside blind thrust (OBT) fault (Rivero et al., 2000; Rivero and Shaw, 2011) was proposed to represent a severe earthquake and tsunami hazard because this low-angle fault surface dips eastward and lies directly beneath the site at about 7-8 km depth. Maloney et al. (2016) concluded that the OBT is inactive based on lack of Quaternary deformation observed in offshore seismic reflection profiles.

What was not recognized then is that the OBT and the larger Thirtymile Bank detachment fault system provide slip surfaces that enable interaction between the shallow steep strike-slip faults of the Coastal Fault System. The Thirtymile Bank detachment continues on a shallow dip to the east beneath the OBT/detachment and the coast, possibly connected to the ancient (Mesozoic) subduction megathrust. It is uncertain whether the detachments are offset or terminated by the steep Newport-Inglewood and other strike-slip faults of the Inner Borderland. However, accurately located seismicity data (Hauksson et al., 2012, Figure 7-9) and earthquake focal mechanisms provide evidence for activity on both vertical strike-slip and moderate to shallow-dipping detachments that may act as blind thrusts or oblique-reverse faults. Fault interaction between the steep strike-slip and oblique-slip faults with the low-angle detachments may produce large, complex, multi-fault earthquakes (Legg et al., 2018) similar to those observed recently in New Zealand (M_w7.8 Kaikoura, Hamling et al., 2017) and northern Baja California (M_w7.2 El Mayor-Cucapah, Fletcher et al., 2014).

The major local earthquake tsunami source for the San Onofre area is the nearby Coastal Fault System which includes the Newport-Inglewood-Rose Canyon strike-slip fault zone along the continental shelf edge, and the San Mateo, San Onofre, and Carlsbad oblique reverse-slip faults that lie beneath the continental slope to the west (Figure 7-10). The Newport-Inglewood–Rose Canyon (NIRC) fault zone lies about 7 km offshore from the ISFSI. Although considered to be a strike-slip fault zone, branch and secondary faults adjacent to the NIRC include the San Mateo-Carlsbad, San Onofre, and Oceanside fault zones which exhibit seafloor uplift (Figure 7-10). The combined fault zones form a Coastal Fault System that stretches from Santa Monica to San Diego and beyond with similar poorly mapped faults offshore northern Baja California as far south as Punta Banda where the Agua Blanca fault passes offshore (Legg, 1985, others). A simple nine-segment model representing the prominent fault sections offshore between Dana Point and La Jolla is used to evaluate the local tsunami potential to the ISFSI (Table 7-4).

Elastic dislocation models (Okada, 1985) were used to determine the seafloor uplift for simple rectangular fault segments (Figure 7-11) with different strike, dip, rake and slip for each segment determined from seismic reflection profile observations (Sorlien et al., 2006) and seafloor morphology. The models are very simple compared to actual slip distributions modeled from historic earthquakes but are sufficient to provide reasonable estimates of the static seafloor deformation for tsunami source and propagation models. Similar models were used for tsunami inundation modeling offshore California (Synolakis et al., 2002b; Legg et al., 2004; Borrero et al., 2004).

The largest earthquake source (Local-sc1, Table 7-5) used all nine segments with parameters given in Table 7-4. Two other composite source models used the four segments of the Newport-Inglewood and Oceanside (Rose Canyon) strike-slip fault, with oblique-slip on the north and south segments of the South Coast Offshore fault (source Local-sc3, Table 7-5), and the San Mateo-San Onofre-Carlsbad oblique-reverse fault, with strike-slip on the San Onofre segment (source Local-sc2, Table 7-5).

The slip values used were based on observations from the M_w7.8 Kaikoura earthquake, which had up to 25-m of strike-slip and 9-m of reverse-slip near a major left-step (restraining bend) between the Jordan thrust and Kekerengu faults (Hamling et al., 2017). We put the maximum slip on the South San Mateo fault with oblique-reverse rake (Table 7-4). Larger slip with oblique-reverse rake was also placed on the South Carlsbad segment where the strike bends more to the southeast (restraining bend). The resulting magnitudes are: M_w7.62 for the 9-segment model, M_w7.44 for the 4-segment South Coast Offshore model, and M_w7.41 for the 5-segment San Mateo-San Onofre-Carlsbad model. The seafloor uplift for the three composite sources, computed using the Okada (1985) analytical equations, ranges from a maximum of 4 m for the scenarios with the San Mateo segments, and over 2.5 m for the oblique-slip on the Newport-Inglewood-Rose Canyon-Oceanside model (Figure 7-12). The large uplift occurs on the northern fault segment offshore from the San Joaquin Hills and does not include potential uplift on the San Joaquin Hills blind thrust, which would mostly occur on land.

Offshore landslides along the steep escarpments that bound the major basins of the Inner Borderland have been considered as potential tsunami sources. Some of these were modeled including the San Pedro Basin debris slide (Borrero et al., 2004) and large basement-involved landslides (Legg and Kamerling, 2003; Shi et al., 2016). The frequency of large submarine slides capable of producing significant tsunamis appears to be very low, 7,500 years or greater. Continued acquisition of high-resolution multi-beam bathymetry provides better data to enable more accurate identification of slope failures around the Borderland (Brothers et al., 2019). The landslide areas mapped near San Onofre from older surveys (Clarke et al., 1987) are now recognized as the complex seafloor deformation along the San Mateo-San Onofre-Carlsbad fault zone at the base of the continental slope. Therefore, we have not attempted additional modeling of submarine landslides at this time.

Table 7-1. Bathymetry/topography numerical grids used for the hydrodynamic simulations.

Grid name	Data source	Longitude range (^oE)	Latitude range (^oN)	Grid cell size (arc-sec)	Grid cell size* (m)	Grid size (N_{LON}*N_{LAT})
P	NOAA/PMEL	120.0167-292.0167	-73.9598-62.0001	240	~7421	2581*2879
AA	GEBCO (2021)	237.00-243.39	32.0-34.0	30	778.8	768*360
A	NOAA/NGDC	240.7-243.0	32.3-34.2	6	155.8	1381*1141
B	NOAA/NGDC	242.2517-242.5483	33.2617-33.4783	1	26.0	1069*781
C	NOAA/NGDC-CE	242.4253-242.4597	33.3503-33.3747	1/6	4.3	745*529

*Cell size in meters computed at equator for grid P and latitude 33^{o}N for grids AA, A, B and C.

Table 7-2. Subduction zone 4-letter labeling used for the NOAA tsunami unit sources (Arcas, 2015).

Subduction Zone	NOAA/PMEL 4-letter code
Aleutian-Alaska-Cascadia	acsz
Central and South America	cssz
Eastern Philippines	epsz
Kamchatka-Bering	kbsz
Kamchatka-Kuril-Japan-Izu-Mariana-Yap	kisz
Manus-Oceanic Convergent Boundary	mosz
New Guinea	ngsz
New Zealand-Kermadec-Tonga	ntsz
New Britain-Solomons-Vanuatu	nvsz
New Zealand-Puysegur	nzsz
Ryukyu-Kyushu-Nankai	rnsz

Table 7-3. Source specification for the far-field seismic scenarios modeled in this report.

Source Name	Subduction zone*	Location	M_w**	Length (km)	Width (km)	Slip (m)	Fault model specification***
EA-sc1	acsz	Alaska	9.36	varies	varies	varies	4m*(b31, b38) + 8m*(b32-b33, b36-b37, a31, a38, z31, z38, y31) + 8.67m*(y38, x31, w31-w36) + 10m*(b34-b35, a32, a37, z32, z37, y32, y37) + 15m*(a33-a36, z33, z36, y33, y36, x32, x37) +20m*(z34-z35, y34-y35, x33-x36)
EA-sc2	acsz	Alaska	9.52	varies	varies	20	b30-b38, a30-a37, z30-z37, y30-y37, x30-x37, w30-w36
EA-sc3	acsz	Alaska	9.53	1500	100	33.25	b25-b39, a25-a39
EA-sc4	acsz	Alaska	9.32	varies	varies	varies	2m*(w31-w33, w36) + 4m*(z31, z38, y31, y38, x31, w34-w35) + 6m*(a31, a38) + 8.67m*(b31, b38, y32, y37, x32-x33, x36-x37) + 10m*(b32, b37, a32, a37, z32, z37, x34-x45) + 15m*(a33, a36, z33, z36, y33-y36) +20m*(b33-b36, a34-a35, z34-z35)
EA-sc5	acsz	Alaska	9.53	varies	varies	varies	8m*(w30-w31) + 10m*(b30, z30, y30, y38, x30-x31, x37, w32-w36) + 15m*(b39, a30, z31, z38, y31-y32, y37, x32-x36) + 20m*(b31-b38, a31, a38-a39, z32, z37, y33-y36) + 30m*(a32, a37, z33-z36) +40m*(a33-a36)
KU-sc1	kisz	Kurils	9.53	1200	100	41.57	b4-b15, a4-a15
KU-sc2	kisz	Kurils	9.53	1200	100	varies	30m*(b4, b13-b15, a14-a15) + 40m*(b5, b9-b12, a4, a10-a13) + 50m*(b6-b8, a5, a8-a9) + 60m*(a6-a7)

∗Refer to Table 7-2 for description of subduction zones.
∗∗M_w computed using modulus of elasticity μ = 45 GPa.
∗∗∗Refer to Appendix A for unit source earthquake parameters.

Table 7-4. Near-field fault parameters for the elastic dislocation model tsunami source.

Segment (#)	Segment Description	Length (km)	Width (km)	Strike (^{o})	Dip (^{o})	Slip (m)	Rake (^{o})	Top (km)	M_0* (Nm/10^{19})	M_w*
	S. Coast Offshore	**84.5**	**12**					**0.5**	**12.49**	**7.36**
1	S. Coast Offshore N	22.32	12	138.1	90	2	180	0.5	1.61	6.77
2	S. Coast Offshore m	35.34	12	129.3	80	4	165	0.5	5.09	7.10
3	S. Coast Offshore S	26.84	12	144.7	80	6	105	0.5	5.80	7.14
	San Mateo Reverse	**15.70**	**14**					**1.0**	**3.53**	**7.00**
4	San Mateo Reverse N	10.40	14	319.0	60	4	115	1.0	1.75	6.79
5	San Mateo Reverse S	5.30	14	339.0	60	8	105	1.0	1.78	6.80
	San Onofre Trend	**15.33**	**5**					**1.0**	**0.46**	**6.41**
6	San Onofre Trend	15.33	5	294.2	90	2	180	1.0	0.46	6.41
	Carlsbad Reverse N	**21.49**	**50**					**1.0**	**10.46**	**7.31**
7	Carlsbad Reverse N0	13.37	50	294.2	30	4	105	1.0	8.02	7.24
8	Carlsbad Reverse N1	8.12	50	133.2	30	2	165	1.0	2.44	6.89
	Oceanside	**26.63**	**12**					**0.5**	**3.83**	**7.02**
9	Oceanside	26.63	12	302.4	90	4	165	0.5	3.83	7.02

∗M_0 and M_w computed using modulus of elasticity μ = 30 GPa.

Table 7-5. Near-field composite seismic sources.

Source (#)	Segments* (#)	M_0** (Nm/10^{19})	M_w**
Local-sc1	1-9	30.77	7.62
Local-sc2	4-8	14.45	7.41
Local-sc3	1-3, 9	16.33	7.44

∗Refer to Table 7-4 for description of segments.

∗∗M_0 and M_w computed using modulus of elasticity μ = 30 GPa.

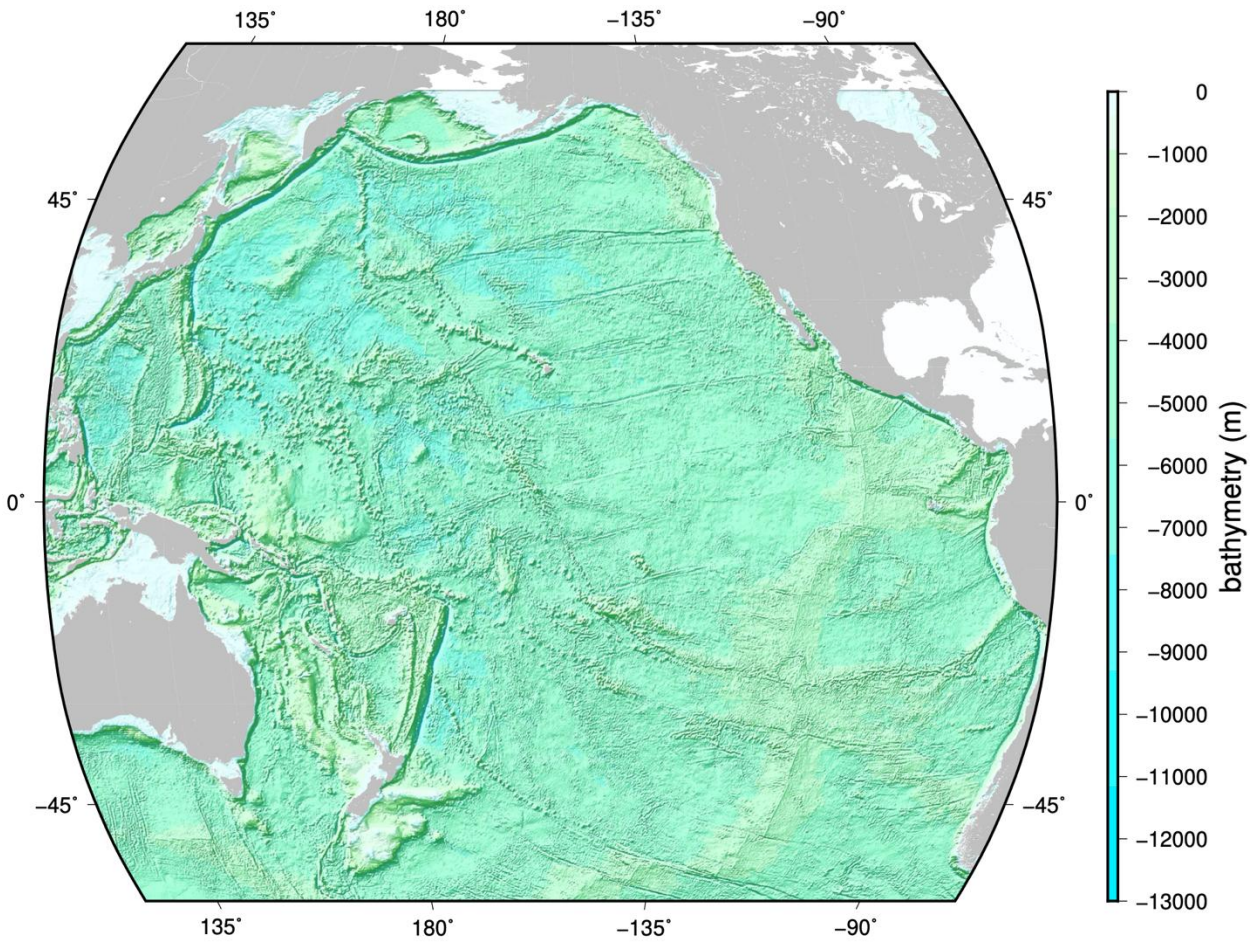


Figure 7-1. The Pacific Ocean bathymetry grid (grid *P*) of 4 arc-min spatial resolution used with MOST for the far-field tsunami simulations.

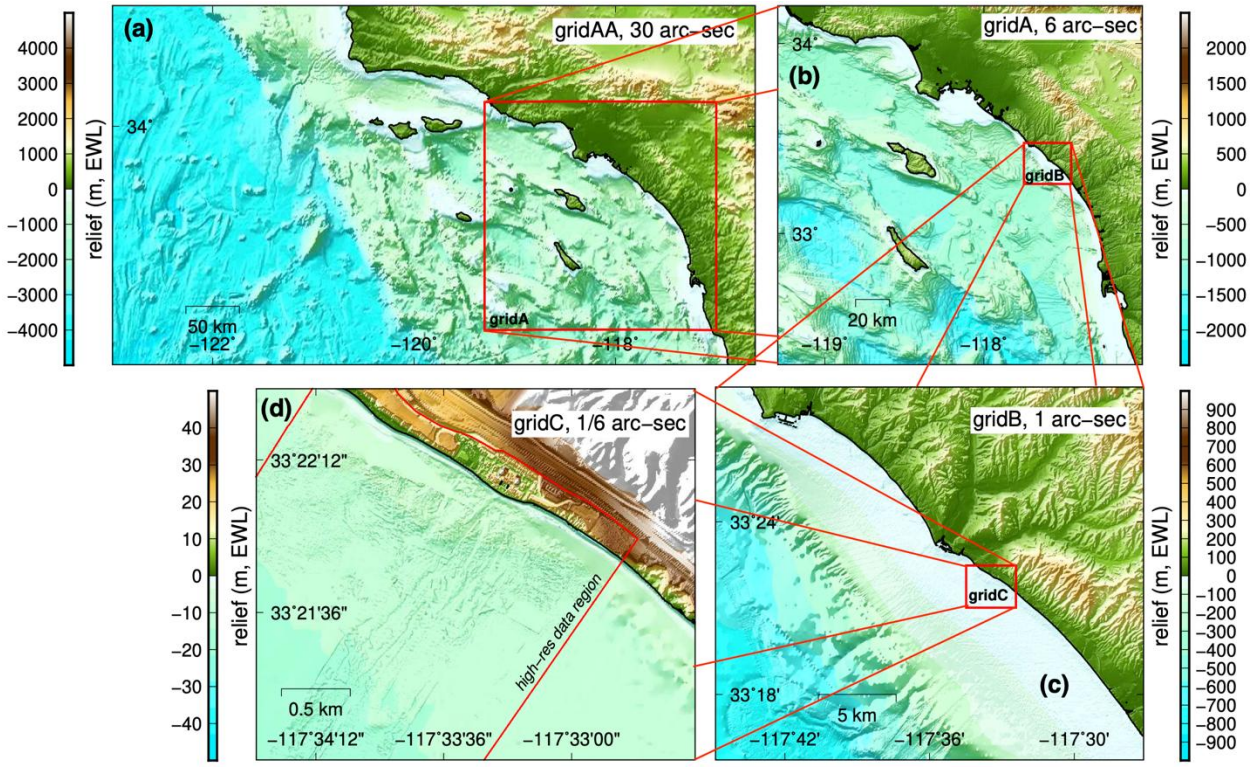


Figure 7-2. Nested grids of increasing resolution (grid AA: 30 asc-sec; grid A: 6 arc-sec; grid B: 1 arc-sec; grid C: 1/6 arc-sec) used for the numerical computations.

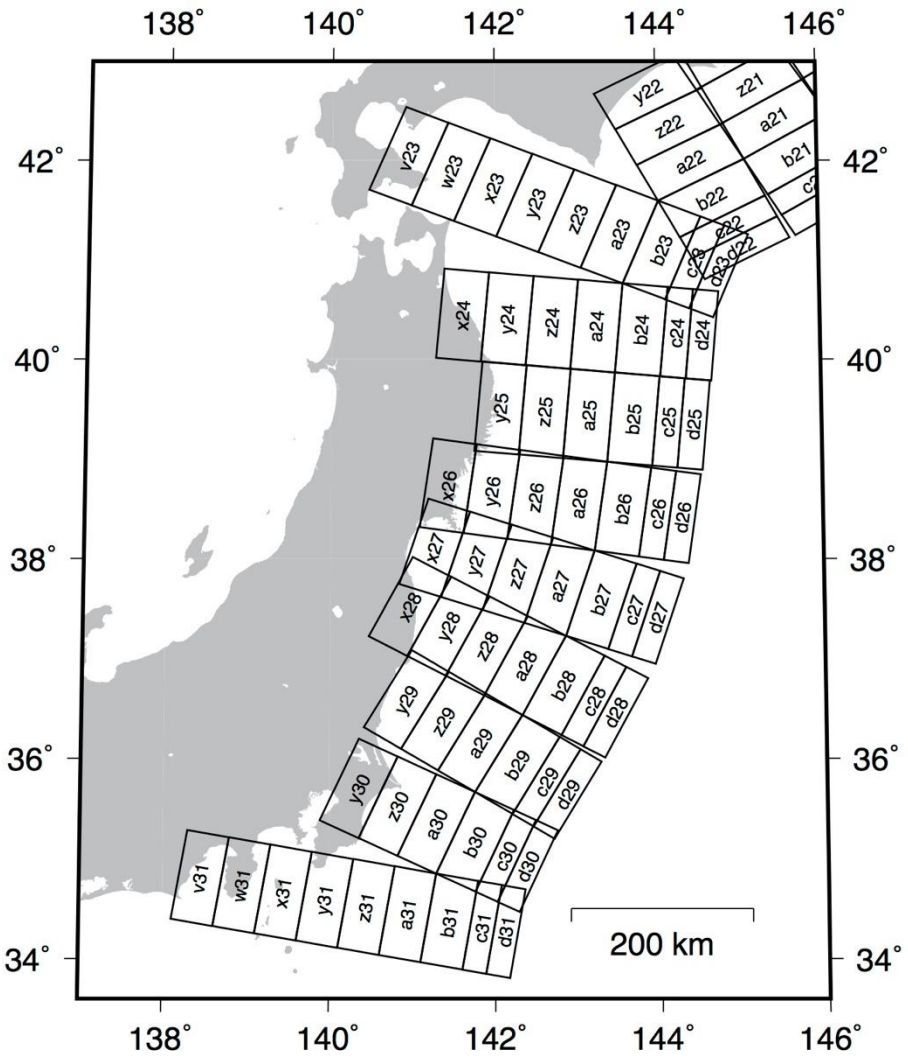


Figure 7-3. NOAA/PMEL's unit sources and labeling along the Japan subduction zone (kisz).

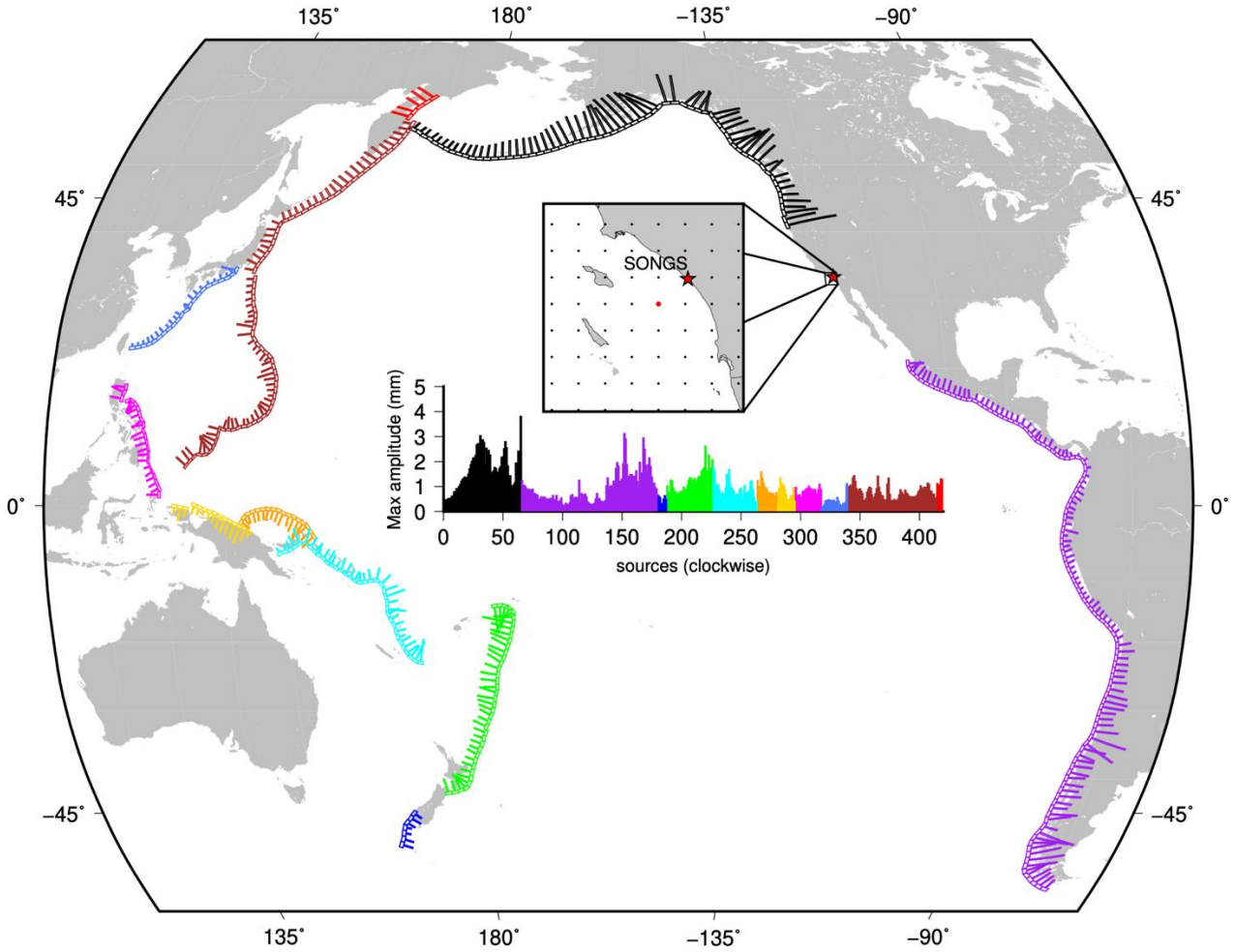


Figure 7-4. Tsunami hazard sensitivity for the study site to the location of the unit sources (only shallowest (row B) unit sources shown here). The length of the bars shows the relative maximum amplitude offshore SONGS from each unit source. The inset bar figure shows the maximum amplitude values, moving clockwise around the Pacific Ocean, starting from W. Aleutians and ending at N. Kamchatka. The inset map figure shows the NOAA/PMEL unit source output grid nodes with 16 arc-min spacing (black dots) and the grid node selected to extract the unit source maximum amplitudes (red dot) relative to the location of SONGS (red star).

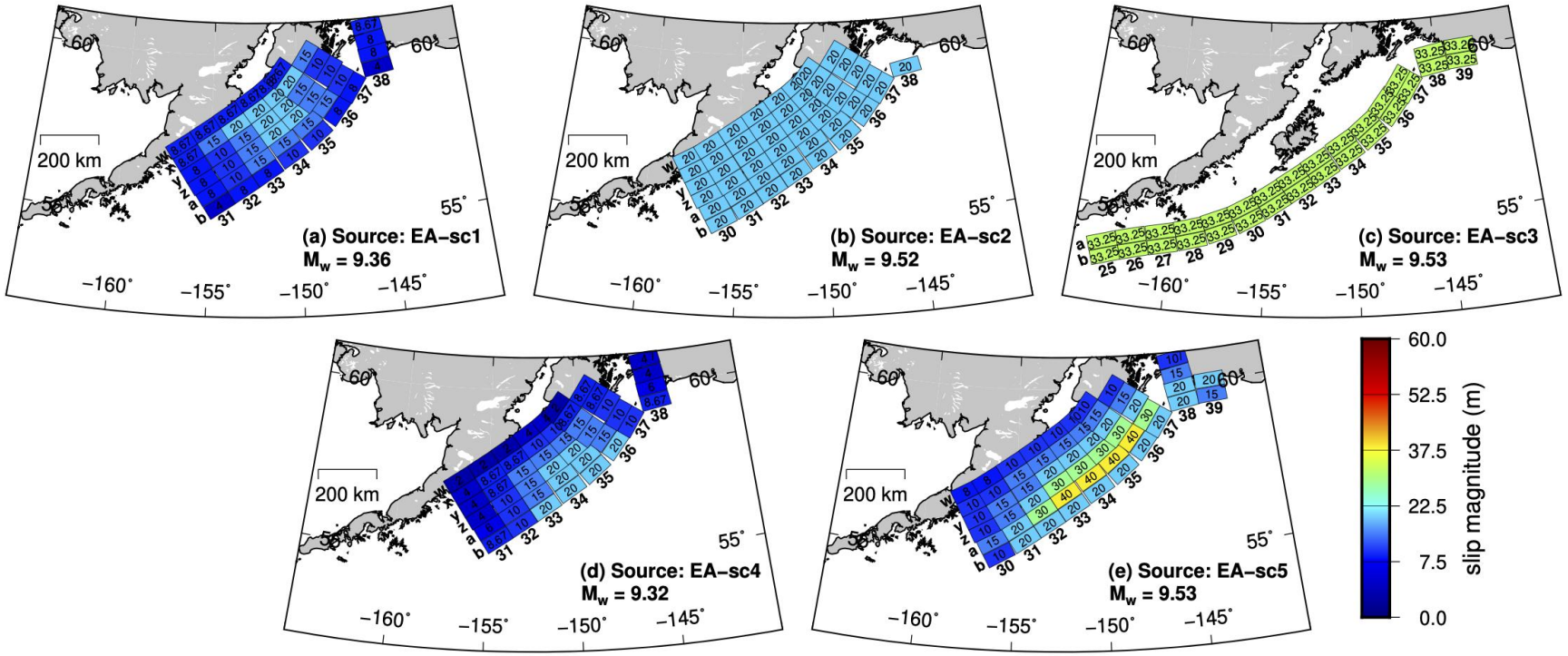


Figure 7-5. Definition of the five Eastern Aleutian (far-field) seismic sources using NOAA/PMEL's unit sources - see Table 7-3 for sources description and Appendix A for the earthquake parameters of the unit sources.

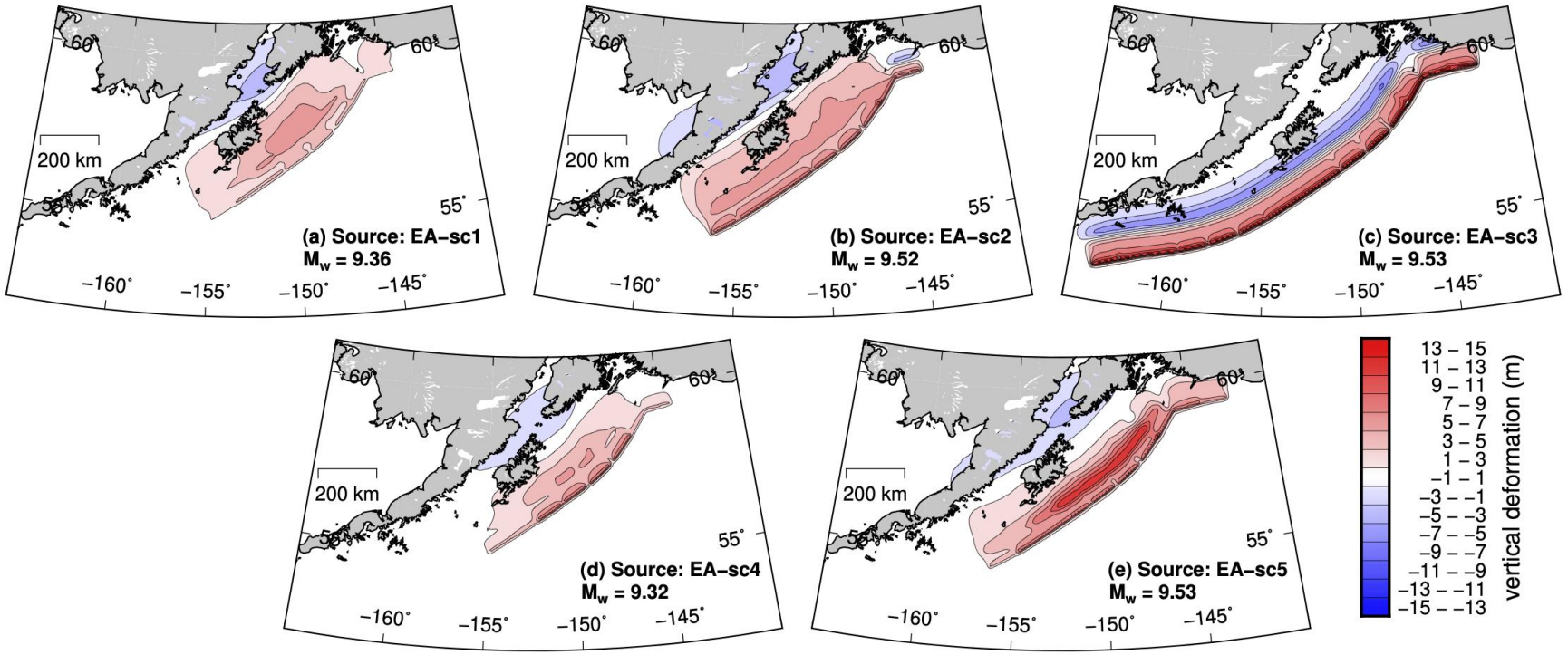


Figure 7-6. Vertical co-seismic displacement for the five Eastern Aleutian (far-field) seismic sources. Contours of vertical deformation drawn every 2 m starting from ±1 m. Blue and red colors show negative (subsidence) and positive (uplift) vertical deformation, respectively.

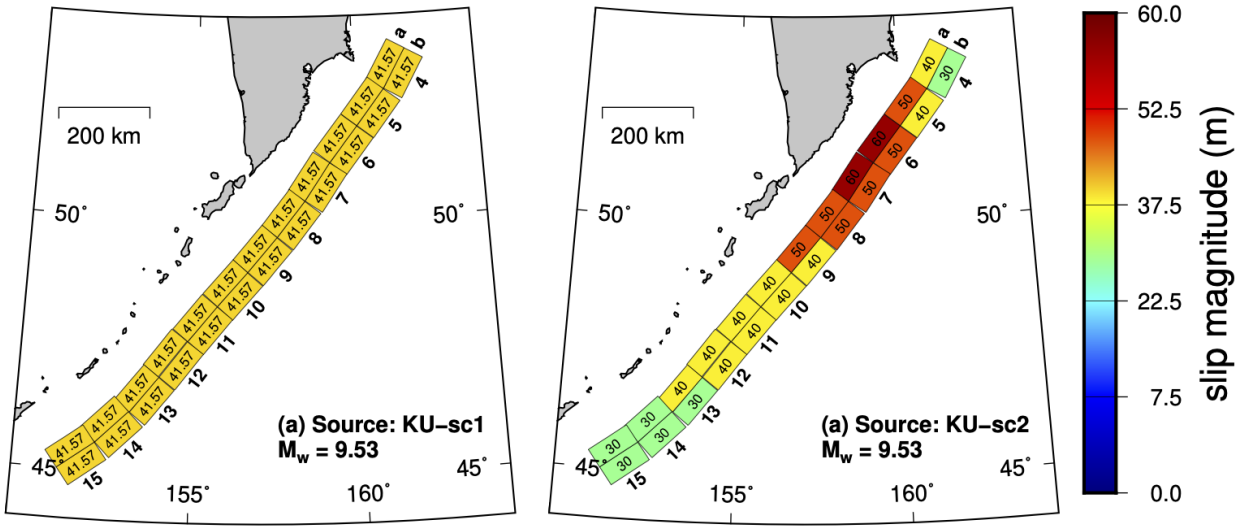


Figure 7-7. Definition of the two Kuril (far-field) seismic sources using NOAA/PMEL's unit sources - see Table 6-3 for source descriptions and Appendix A for the earthquake parameters of the unit sources.

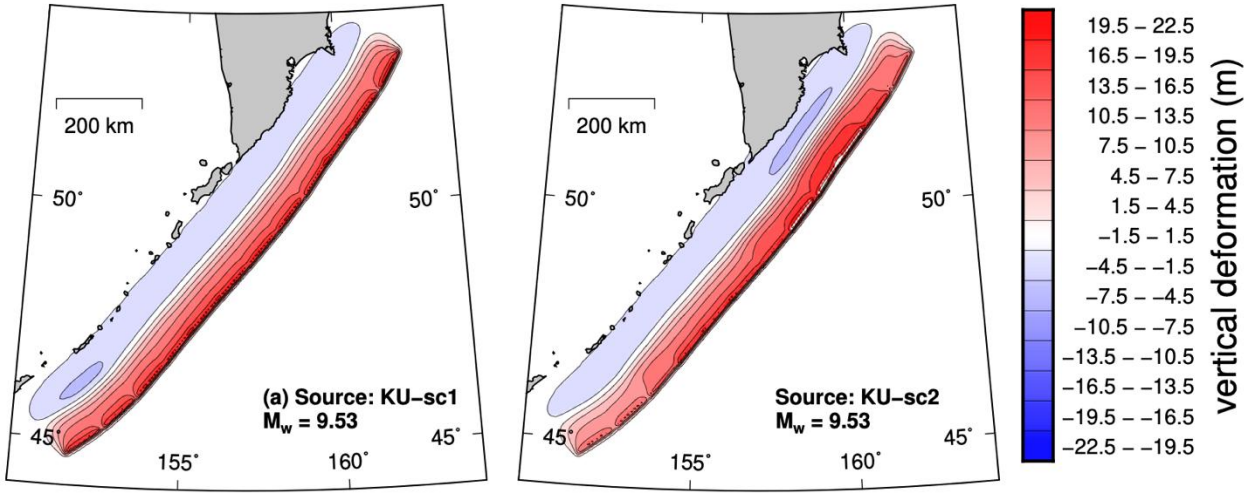


Figure 7-8. Vertical co-seismic displacement for the two Kuril (far-field) seismic sources. Contours of vertical deformation drawn every 3 m starting from ±1.5 m. Blue and red colors show negative (subsidence) and positive (uplift) vertical deformation, respectively.

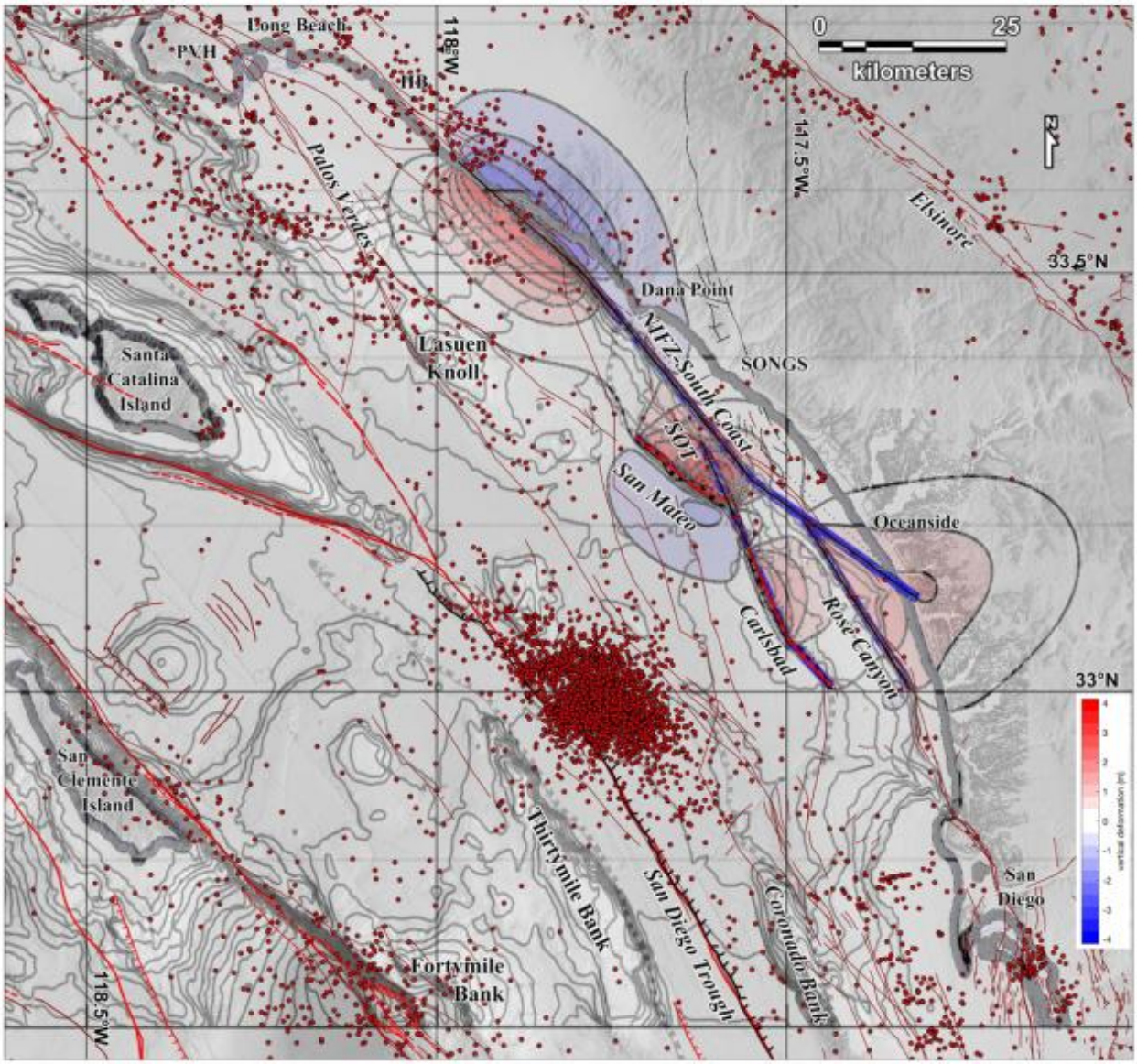


Figure 7-9. Map showing seafloor deformation produced by local tsunami source 1 with all nine fault segments, with bathymetry and relocated seismicity (M > 2, 1981-2019; Hauksson et al., 2012, 2019 update). Modeled uplift matches bathymetry in most areas, except north of Dana Point where the San Joaquin Hills blind thrust (Grant et al., 2002) is absent from this model.

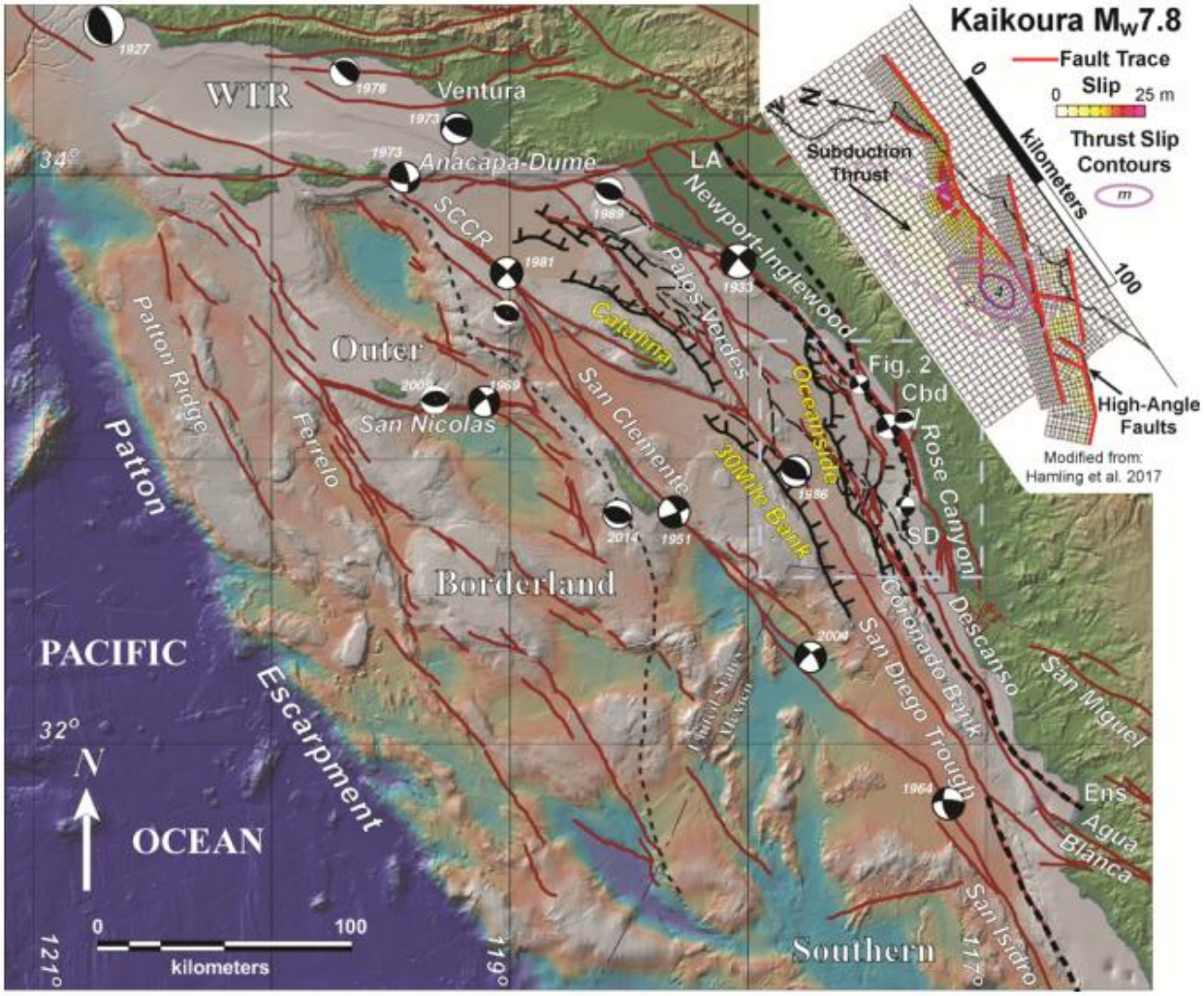


Figure 7-10. Map comparing rupture model for the 2016 Kaikoura, New Zealand earthquake with the Coastal Fault System located between Los Angeles (LA) and San Diego (SD) (Source: Legg et al. (2018)).

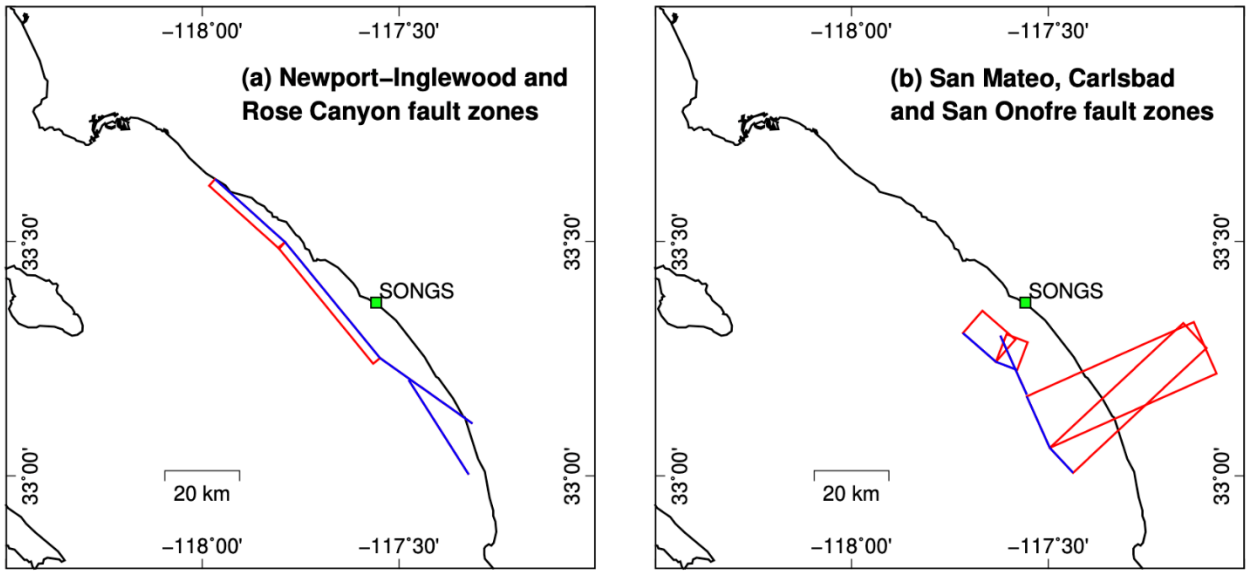


Figure 7-11. Maps showing the simple rectangular fault models for the local tsunami cases. (a) Four-segments with strike-slip and oblique-slip used for the Newport-Inglewood and Rose Canyon fault zones. (b) Two-segments each with oblique-slip used for the San Mateo and Carlsbad faults, and one-segment strike-slip model for the San Onofre Trend. Blue lines are upper tip of fault segments, red outlines deep fault extent.

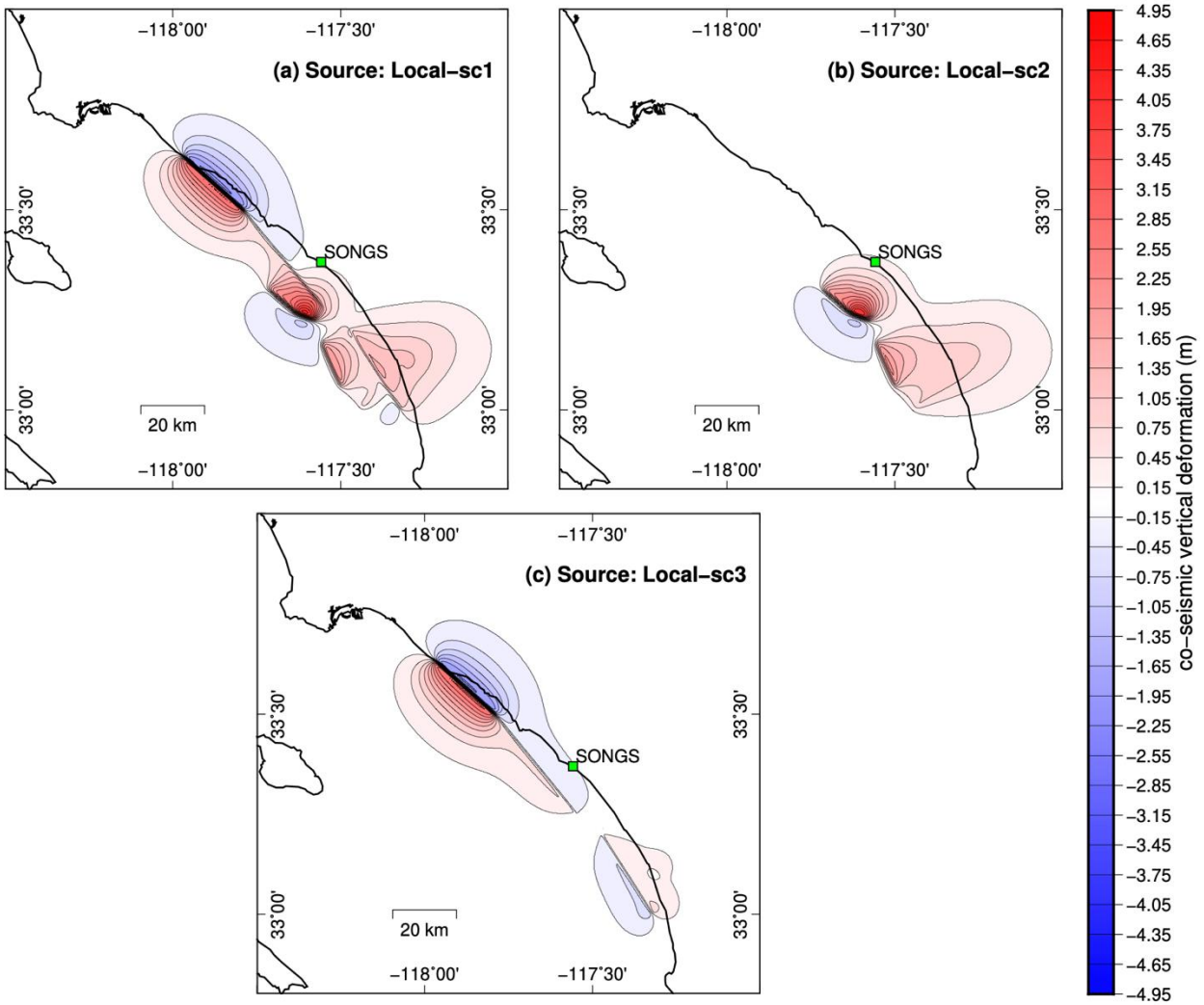


Figure 7-12. Vertical co-seismic displacement for the three composite near-field sources - see Table 6-5. Contours of vertical deformation drawn every 0.3 m starting from ±0.15 m. Blue and red colors show negative (subsidence) and positive (uplift) vertical deformation, respectively.

8.0 COMPUTATIONS

8.1 RESULTS FOR FAR-FIELD SEISMIC TSUNAMI CASES

8.1.1 Eastern Aleutians

The distribution of maximum wave amplitudes across the Pacific Ocean for all five Eastern Aleutians sources is shown in Figure 8-1. The plots show how seismic sources from the Eastern Aleutians have an efficient directivity towards the West Coast of the United States. Sources EA-sc3 and EA-sc5 (subplots *c* and *e* in Figure 8-1, respectively), both assigned M_w9.5, beam the most tsunami energy towards southern California and the SONGS site compared to the other Eastern Aleutian sources considered in this report. Source EA-sc2 (subplot *b* in Figure 8-1), also with M_w9.5 but being assigned a smaller maximum slip magnitude, does not produce maximum wave amplitudes in southern California as high as the other two M_w9.5 Eastern Aleutian sources. Sources EA-sc1 and EA-sc4 (subplots *a* and *d* in Figure 8-1, respectively), which were assigned smaller magnitudes (M_w9.4 and M_w9.3, respectively), produce the smallest maximum wave amplitudes across the Pacific Ocean.

Source EA-sc1

Maximum wave amplitudes produced during the numerical simulations inside the domains of grids AA, A and B for source EA-sc1 are shown in Figure 8-2. Maximum wave amplitude in grid AA is more pronounced along the NW coastline section of the grid (i.e., the west-facing coastline stretch near Lompoc), the section between Oxnard and Carpinteria, the section between Long Beach and Huntington Beach, and San Diego. SE of the SONGS site, computed maximum wave amplitude is somewhat higher compared to just offshore SONGS. This local amplification just SE of SONGS is the result of complex reflection patters at the shoreline, with the Channel Islands also playing a significant role in the distribution of maximum amplitudes along the mainland coastline. The observations made for the maximum amplitudes computed across grids AA, A and B for source EA-sc1 are common between all Eastern Aleutian sources.

The results for the finest-resolution grid (grid C) are shown in Figure 8-3. The maximum tsunami amplitude in the numerical domain ranges between 1.5 and 2.0 m (inferred from the color bar of Figure 8-3*a*). Time series of wave amplitude extracted from a numerical tide gauge located just offshore SONGS at a depth of 5.57 m (EWL) show the maximum and minimum amplitudes of 1.88 and -2.73 m (EWL) occurring ~6 and ~7.8 hr. after the seismic rupture, respectively (Figure 8-3*e*). Wave runup along the coastline stretch of the grid is relatively uniform. The simulation (which assumes that the seawall is not present) yields a maximum runup of 2.0 m (EWL), and the waves would not produce runup/inundation at the SONGS site (Figure 8-3*c*).

Source EA-sc2

Maximum wave amplitudes for source EA-sc2 produced during the numerical simulations inside the domains of grids AA, A and B are shown in Figure 8-4. The same

maximum wave amplitude patterns are observed as for source EA-sc1, but with higher amplitudes. The local wave amplification just SE of the SONGS site appearing in the grid B domain is also more pronounced.

The results for the finest-resolution grid (grid C) are shown in Figure 8-5. The maximum tsunami amplitude in the numerical domain ranges between 2.5 and 4.5 m (inferred from the color bar of Figure 8-5*a*). Time series of wave amplitude extracted from a numerical tide gauge located just offshore SONGS at a depth of 5.57 m (EWL) show the maximum and minimum amplitudes of 3.34 and -5.30 m (EWL) occurring ~6 and ~7.8 hr. after the seismic rupture, respectively (Figure 8-5*e*). Wave runup along the coastline stretch of the grid is relatively uniform. The simulation (which assumes that the seawall is not present) yields a maximum runup of 4.1 m (EWL) at the eastern grid boundary and 3.4 m (EWL) at the SONGS site (at longitudes between -117.5594 and -117.5574^{o}W). The waves would produce runup/inundation at the SONGS site (Figure 8-5*c*-*d*). Maximum tsunami elevation and maximum flow depth around the NUHOMS ISFSI would be 3.4 m (EWL) and 0.6 m, respectively.

Source EA-sc3

Maximum wave amplitudes produced during the numerical simulations inside the domains of grids AA, A and B for source EA-sc3 are shown in Figure 8-6. The same maximum wave amplitude patterns are observed as for sources EA-sc1 and EA-sc2, but with even higher amplitudes. The local wave amplification just SE of SONGS appearing in the grid B domain is the most pronounced across all Eastern Aleutian source simulations.

The results for the finest-resolution grid (grid C) are shown in Figure 8-7. The maximum tsunami amplitude in the numerical domain ranges between 4.0 and 5.5 m (inferred from the color bar of Figure 8-7*a*). Time series of wave amplitude extracted from a numerical tide gauge located just offshore SONGS at a depth of 5.57 m (EWL) show the maximum and minimum amplitudes of 5.03 and -5.09 m (EWL) occurring ~7 and ~6.9 hr. after the seismic rupture, respectively (Figure 8-7*e*). The third crest is the highest, but with almost equal amplitude to the first rise. These wave amplitudes are the highest across all sources considered in this study. The simulation (which assumes that the seawall is not present) yields a maximum runup of 7.0 m (EWL) at a steep topographic node and 5.9 m (EWL) at the SONGS site (at longitudes between -117.5594 and -117.5574^{o}W). The maximum runup produced for source EA-sc3 is also the highest across all seismic sources considered in this study. The waves would produce runup/inundation at the SONGS site (Figure 8-7*c*-*d*). Maximum tsunami elevation and maximum flow depth around the NUHOMS ISFSI would be 5.9 m (EWL) and 2.8 m, respectively.

Source EA-sc4

Maximum wave amplitudes produced during the numerical simulations inside the domains of grids AA, A and B for source EA-sc4 are shown in Figure 8-8. The same maximum wave amplitude patterns are observed as with the other Eastern Aleutian simulations. EA-sc4 is one of the two Eastern Aleutian sources assigned a smaller magnitude of *Mw*9.3 (the other being source EA-sc1). Compared to EA-sc1, maximum amplitudes for EA-sc4 are higher because of the 20 m-slip patches in the source being assigned to the shallower unit sources (Figure 7-5).

The results for the finest-resolution grid (grid C) are shown in Figure 8-9. The maximum tsunami amplitude in the numerical domain ranges between 1.5 and 3.0 m (inferred from the color bar of Figure 8-9*a*). Time series of wave amplitude extracted from a numerical tide gauge located just offshore SONGS at a depth of 5.57 m (EWL) show the maximum and minimum amplitudes of 2.22 and -2.99 m (EWL) occurring ~7 and ~7.7 hr. after the seismic rupture, respectively (Figure 8-9*e*). The third crest is the highest, but with almost equal amplitude to the first rise. Wave runup along the coastline stretch of the grid is relatively uniform. The simulation (which assumes that the seawall is not present) yields a maximum runup of 2.73 m (EWL) near the eastern grid boundary and 2.46 m (EWL) at SONGS (at longitudes between -117.5594 and -117.5574^{o}W). The waves would not produce runup/inundation at the SONGS site (Figure 8-9*c*).

Source EA-sc5

Maximum wave amplitudes produced during the numerical simulations inside the domains of grids AA, A and B for source EA-sc5 are shown in Figure 8-10. The same maximum wave amplitude patterns and similar amplitudes are observed as for source EA-sc3, with both sources being assigned equal magnitude (M_w9.5), but different source characteristics (see Table 7-3). The local wave amplification just SE of the SONGS site appearing in the grid B domain is pronounced as with source EA-sc3.

The results for the finest-resolution grid (grid C) are shown in Figure 8-11. The maximum tsunami amplitude in the numerical domain ranges between 4.0 and 5.0 m (inferred from the color bar of Figure 8-11*a*). Time series of wave amplitude extracted from a numerical tide gauge located just offshore SONGS at a depth of 5.57 m (EWL) show the maximum and minimum amplitudes of 4.73 and -5.44 m (EWL) occurring ~6 and ~7.9 hr. after the seismic rupture, respectively (Figure 8-11*e*). The first rise is the highest, but with almost equal amplitude to the third rise. Wave runup along the coastline stretch of the grid is relatively uniform. The simulation (which assumes that the seawall is not present) yields a maximum runup of 5.75 m (EWL) at a steep topographic point and 5.51 m (EWL) at the SONGS site (at longitudes between -117.5594 and -117.5574^{o}W). The waves would produce runup/inundation at the SONGS site (Figure 8-11*c-d*). Maximum tsunami elevation and maximum flow depth around the NUHOMS ISFSI would be 5.5 m (EWL)and 2.7 m, respectively.

8.1.2 Kuril Islands

The distribution of maximum wave amplitudes across the Pacific Ocean for the two Kuril sources is shown in Figure 8-12. Both the two Kuril sources considered were assigned magnitude M_w9.5, equal to three worst-case scenarios for the Eastern Aleutian seismic sources. However, the maximum slip magnitude assigned to the Kuril sources is higher compared to the Eastern Aleutian sources.

Figure 8-12 shows that the maximum wave amplitudes from the Kuril sources are not directed towards southern California, but to the west of the islands of Hawaii. Kuril source KU-sc2 (subplot *b* in Figure 8-12), which was assigned a variable slip distribution with higher maximum slip values, produces somewhat higher maximum amplitudes in southern California compared to the uniform slip scenario KU-sc1 (subplot *a* in Figure 8-12), but the amplitudes in

southern California are deficient compared to the Eastern Aleutian worst-cases scenarios. Based on Figure 8-12, tsunami impact at SONGS from the two Kuril sources is not expected to be higher compared to the Eastern Aleutian worst-case scenarios. The high-resolution results for the Kuril far-field source are presented below.

Source KU-sc1

Maximum wave amplitudes produced during the numerical simulations inside the domains of grids AA, A and B for source KU-sc1 are shown in Figure 8-13. The same maximum wave amplitude general patterns are observed as for the Eastern Aleutian sources.

The results for the finest-resolution grid (grid C) are shown in Figure 8-14. The maximum tsunami amplitude in the numerical domain ranges between 1.5 and 3.0 m (inferred from the color bar of Figure 8-14*a*). Time series of wave amplitude extracted from a numerical tide gauge located just offshore SONGS at a depth of 5.57 m (EWL) show the maximum and minimum amplitudes of 2.01 and -2.73 m (EWL) occurring ~11.7 and ~11.0 hr. after the seismic rupture, respectively (Figure 8-14*e*). The maximum amplitude near the SONGS site is produced by the sixth wave. Wave runup along the coastline stretch of grid C increases from west to east. The simulation (which assumes that the seawall is not present) yields a maximum runup of 2.9 m (EWL) at the eastern grid boundary and 2.2 m (EWL) at the SONGS site (at longitudes between -117.5594 and -117.5574^{o}W), and the waves would not produce runup/inundation at the SONGS site (Figure 8-14*c*-*d*).

Source KU-sc2

Maximum wave amplitudes produced during the numerical simulations inside the domains of grids AA, A and B for source KU-sc2 are shown in Figure 8-15. The same maximum wave amplitude general patterns are observed as for Kuril source KU-sc1, but with somewhat higher maximum amplitudes due to the higher maximum slip values assigned to source KU-sc2 compared to the uniform slip source KU-sc1 - both sources were assigned the same magnitude (M_w9.5).

The results for the finest-resolution grid (grid C) are shown in Figure 8-16. The maximum tsunami amplitude in the numerical domain ranges between 2.0 and 3.5 m (inferred from the color bar of Figure 8-16*a*). Time series of wave amplitude extracted from a numerical tide gauge located just offshore SONGS at a depth of 5.57 m (EWL) show the maximum and minimum amplitudes of 2.62 and -2.99 m (EWL) occurring ~11.7 and ~11.1 hr. after the seismic rupture, respectively (Figure 8-16*e*). The maximum amplitude near the SONGS site is produced by the sixth wave, as is the case with source KU-sc1. Wave runup along the coastline stretch of grid C increases from west to east. The simulation (which assumes that the seawall is not present) yields a maximum runup of 3.4 m (EWL) at the eastern grid boundary and 2.8 m (EWL) at the SONGS site (at longitudes between -117.5594 and -117.5574^{o}W). The waves would produce runup/inundation at the SONGS site (Figure 8-16*d*), but the inundation does not reach the NUHOMS ISFSI.

8.2 RESULTS FOR LOCAL SEISMIC TSUNAMI CASES

8.2.1 Source Local-sc1

Maximum wave amplitudes produced during the numerical simulations inside the domains of grids A and B for near-field source Local-sc1 are shown in Figure 8-17. Source Local-sc1 is a combination of all nine fault rupture segments listed in Table 7-4. Maximum amplitudes are observed along the coastal stretch between Long Beach and Oceanside. Wave energy is also beamed towards the SE coast of San Clemente Island. Figure 8-17*b* shows highly localized maximum wave amplitude patterns due to the complex characteristics of the fault rupture, the proximity of the source to the coastline, but also due to reflections off the coastline.

The results for the finest-resolution grid (grid C) are shown in Figure 8-18. The maximum tsunami amplitude in the numerical domain ranges between 2.0 and 5.0 m (inferred from the color bar of Figure 8-18*a*). Time series of wave amplitude extracted from a numerical tide gauge located just offshore SONGS at a depth of 5.57 m (EWL) show the maximum and minimum amplitudes of 4.16 and -3.85 m (EWL) occurring ~8 and ~13 min after the seismic rupture, respectively (Figure 8-18*e*). The maximum amplitude near the SONGS site is produced by the first wave. Wave runup along the coastline stretch of grid C ranges between 3.5 to 5.6 m (EWL). The simulation (which assumes that the seawall is not present) yields a maximum runup of 4.8 m (EWL) at the SONGS site (at longitudes between -117.5594 and -117.5574^{o}W). The waves would produce runup/inundation at the SONGS site (Figure 8-18*c*-*d*). Maximum tsunami elevation and maximum flow depth around the NUHOMS ISFSI would be 4.0 m (EWL) and 1.2 m, respectively.

8.2.2 Source Local-sc2

Maximum wave amplitudes produced during the numerical simulations inside the domains of grids A and B for near-field source Local-sc2 are shown in Figure 8-19. Source Local-sc2 is a combination of the San Mateo, San Onofre and Carlsbad segments listed in Table 7-4. Maximum amplitudes are thus more pronounced along the coastal stretch between San Clemente and Oceanside compared to the coastal stretch between San Clemente and Long Beach that is more impacted in source Local-sc1. Similar to source Local-sc1, wave energy is also beamed towards the SE coast of San Clemente Island. Figure 8-19*b* also shows highly localized maximum wave amplitude patterns as with source Local-sc1.

The results for the finest-resolution grid (grid C) are shown in Figure 8-20. The maximum tsunami amplitude in the numerical domain ranges between 1.5 and 4.0 m (inferred from the color bar of Figure 8-20*a*). Time series of wave amplitude extracted from a numerical tide gauge located just offshore SONGS at a depth of 5.57 m (EWL) show the maximum and minimum amplitudes of 2.92 and -3.98 m (EWL) occurring ~9 and ~13 min after the seismic rupture, respectively (Figure 8-20*e*). The maximum amplitude near the SONGS site is produced by the first wave. Wave runup along the coastline stretch of grid C ranges between 2.9 to 4.8 m (EWL). The simulation (which assumes that the seawall is not present) yields a maximum runup of 3.8 m (EWL) at the SONGS site (at longitudes between -117.5594 and -117.5574^{o}W). The waves would produce runup/inundation at the SONGS site (Figure 8-20*c*-*d*). Maximum tsunami

elevation and maximum flow depth around the NUHOMS ISFSI would be 3.4 m (EWL) and 0.4 m, respectively.

8.2.3 Source Local-sc3

The maximum wave amplitudes produced during the numerical simulations inside the domains of grids A and B for near-field source Local-sc3 are shown in Figure 8-21. Source Local-sc3 is a combination of the South Coast and Oceanside segments listed in Table 7-4. Maximum amplitudes are thus subdued along the coastal stretch between San Clemente and Oceanside compared to sources Local-sc1 and Local-sc2. Contrary to sources Local-sc1 and Local-sc2, more wave energy is beamed towards Catalina Island than toward San Clemente Island.

The results for the finest-resolution grid (grid C) are shown in Figure 8-22. The maximum tsunami amplitude in the numerical domain ranges between 0.5 and 2.5 m (inferred from the color bar of Figure 8-22*a*). Time series of wave amplitude extracted from a numerical tide gauge located just offshore SONGS at a depth of 5.57 m (EWL) show the maximum and minimum amplitudes of 1.38 and -1.65 m (EWL) occurring ~97 and ~26 min after the seismic rupture, respectively (Figure 8-22*e*). Wave runup along the coastline stretch of grid C ranges between 1.7 to 3.2 m (EWL). The simulation yields a maximum runup of 2.6 m (EWL) at the SONGS site (at longitudes between -117.5594 and -117.5574^{o}W). The waves would not produce runup/inundation at the SONGS site (Figure 8-22*c*-*d*).

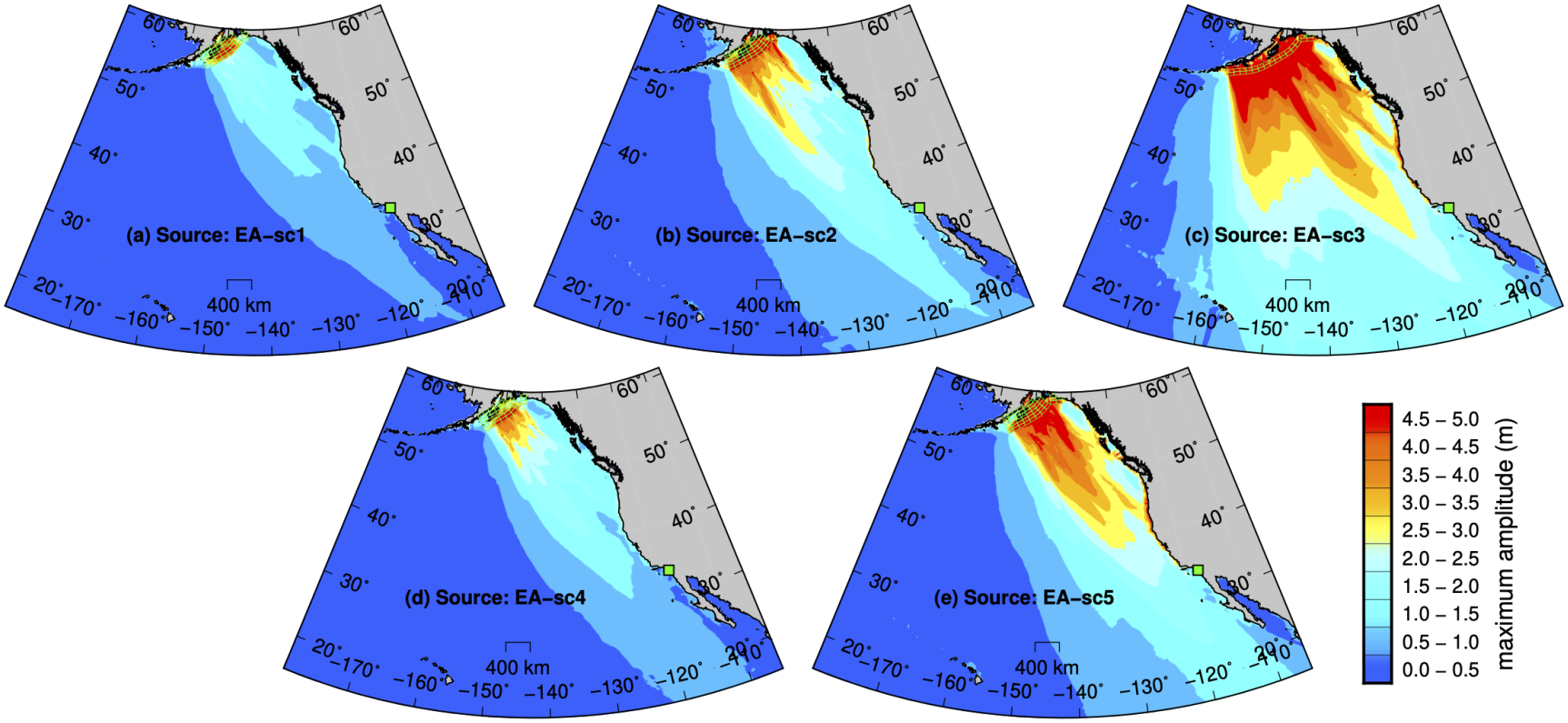


Figure 8-1. Maps showing the maximum tsunami amplitudes (in part of the spatial extent) of grid *P* from the numerical simulation of all five Eastern Aleutian sources - see Table 7-3 for information on the sources.

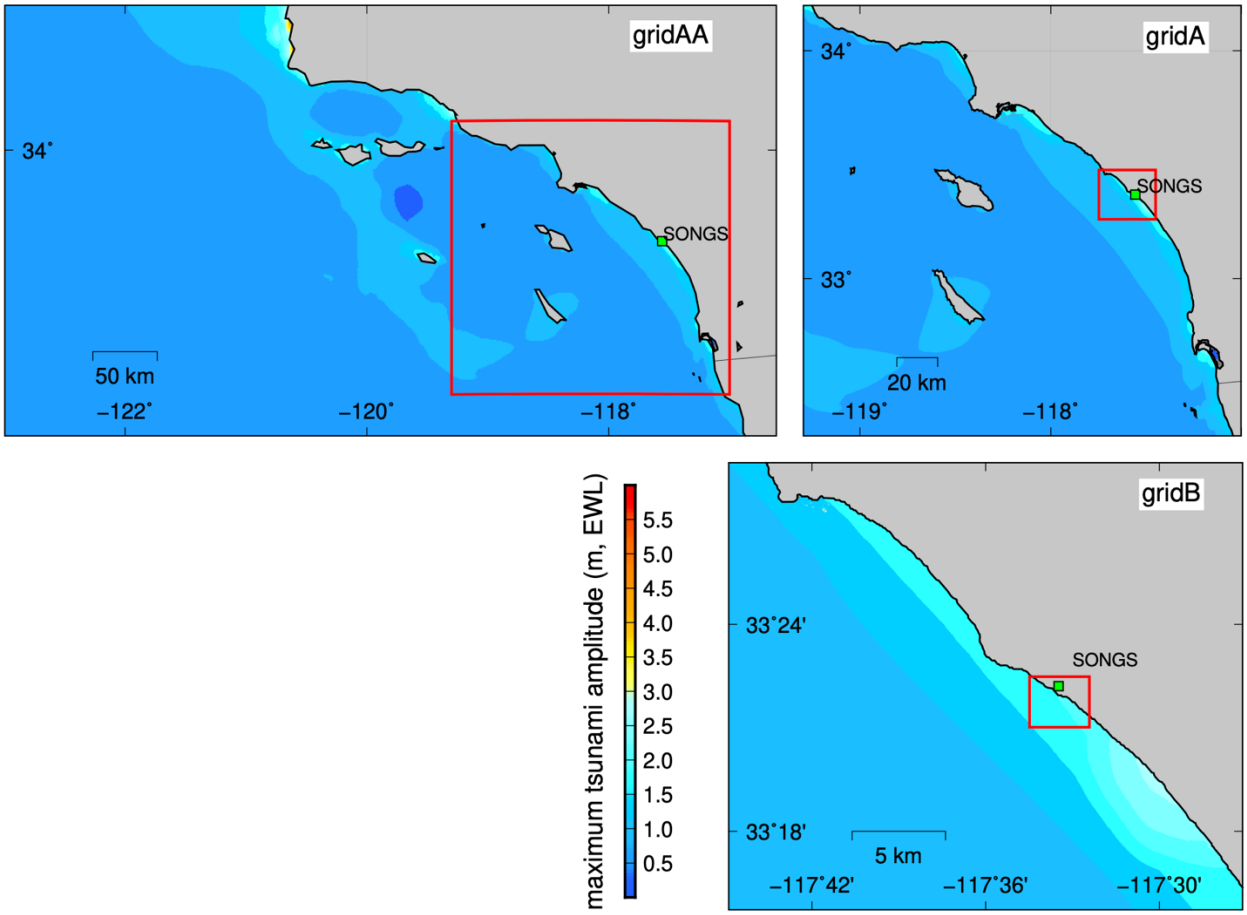


Figure 8-2. Maps showing the maximum tsunami amplitudes inside the domains of grids AA, A, and B during the numerical simulation of the Eastern Aleutian source EA-sc1 - see Table 7-3 for information on the sources.

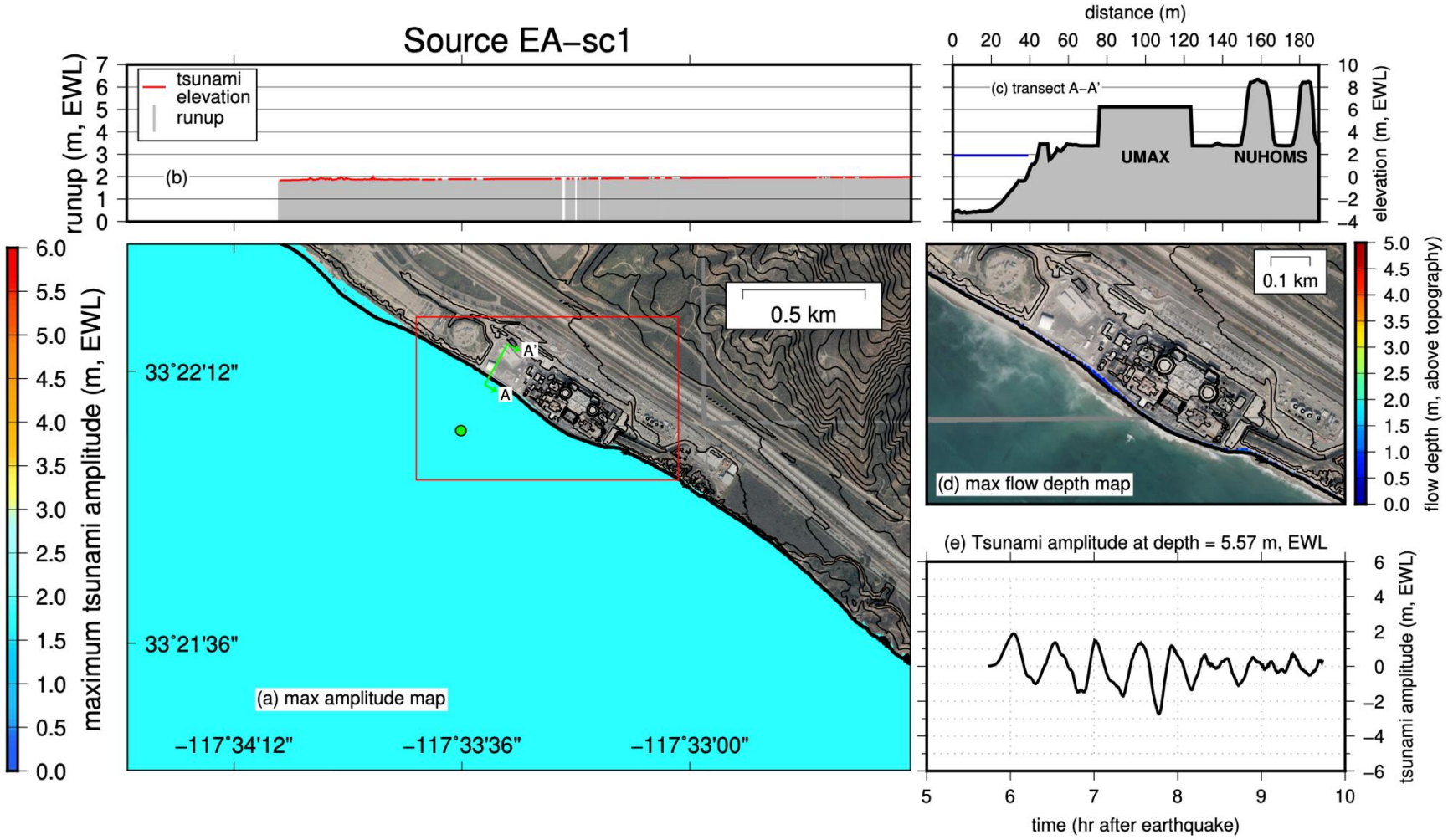


Figure 8-3. Numerical simulation results for the Eastern Aleutians seismic source EA-sc1. (a) Maximum tsunami amplitude across the domain of grid C. (b) Maximum runup and tsunami elevation distribution across the coastline in grid C. (c) Transect of maximum tsunami elevation across the SONGS site - see (a) for position of transect. (d) Maximum flow depth distribution across the SONGS site. (e) Time series of free surface elevation just offshore the SONGS site - time series extracted from the location shown with the green dot in (a).

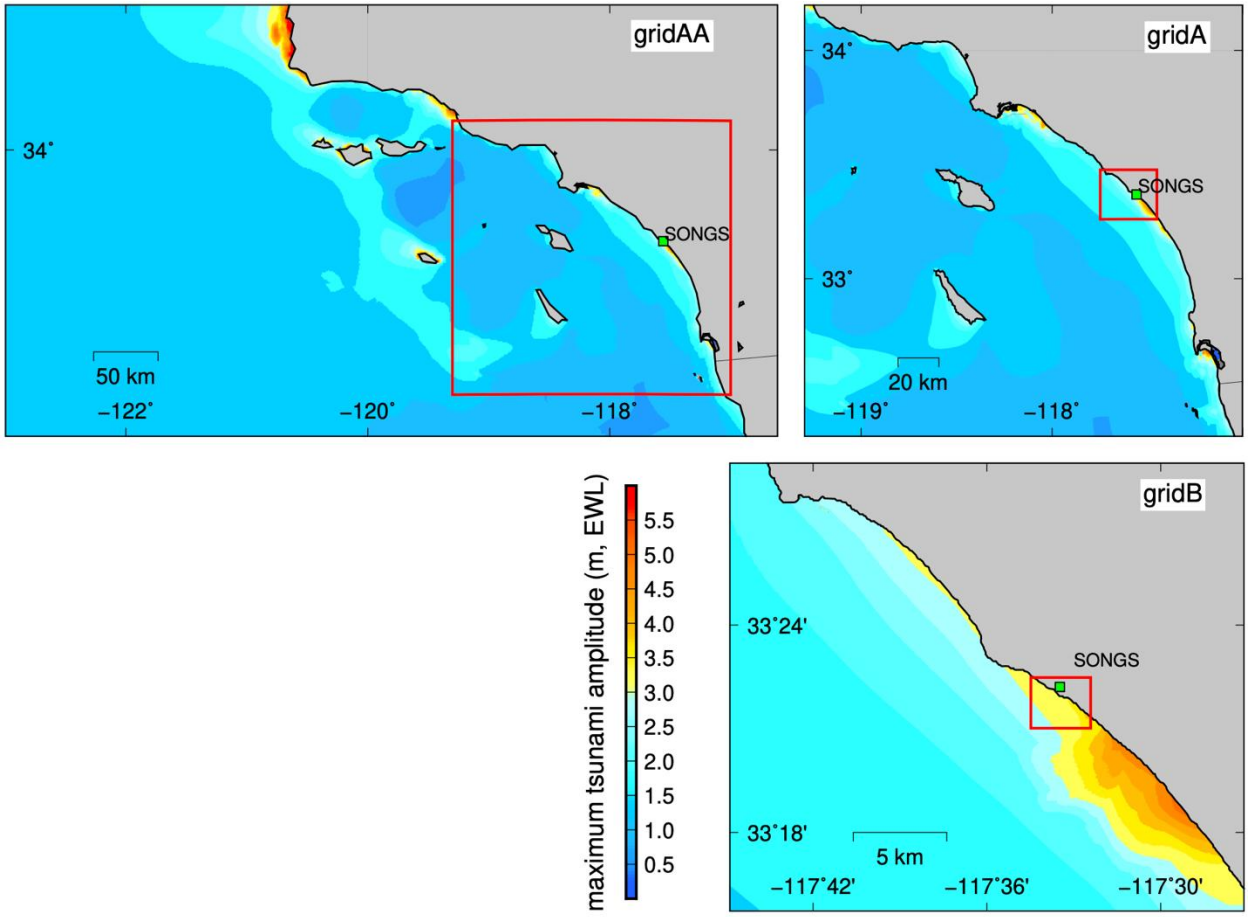


Figure 8-4. Maps showing the maximum tsunami amplitudes inside the domains of grids AA, A, and B during the numerical simulation of the Eastern Aleutian source EA-sc2 - see Table 7-3 for information on the sources.

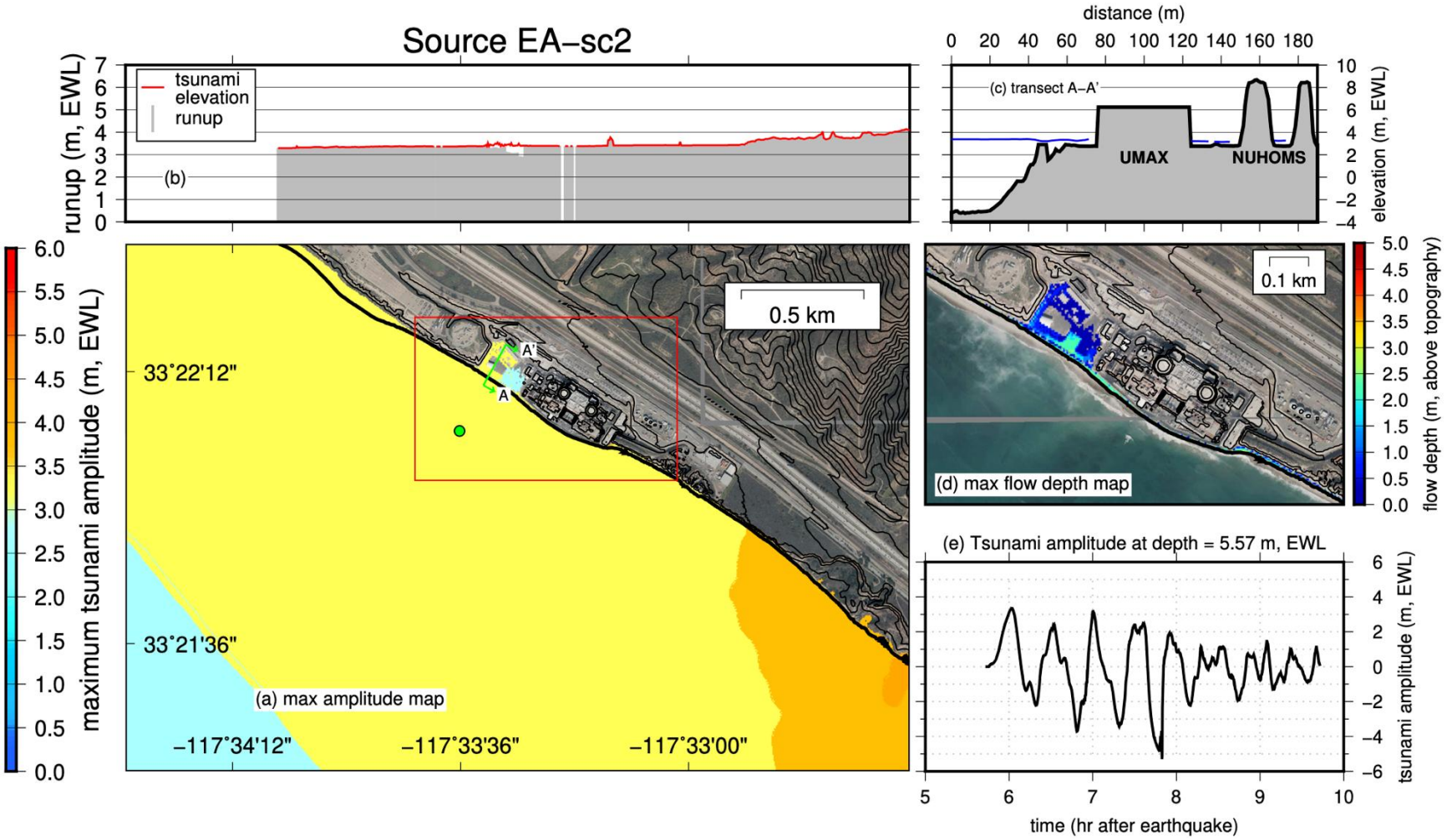


Figure 8-5. **Numerical simulation results for the Eastern Aleutians seismic source EA-sc2. (a) Maximum tsunami amplitude across the domain of grid C. (b) Maximum runup and tsunami elevation distribution across the coastline in grid C. (c) Transect of maximum tsunami elevation across the SONGS site - see (a) for position of transect. (d) Maximum flow depth distribution across the SONGS site. (e) Time series of free surface elevation just offshore the SONGS site - time series extracted from the location shown with the green dot in (a).**

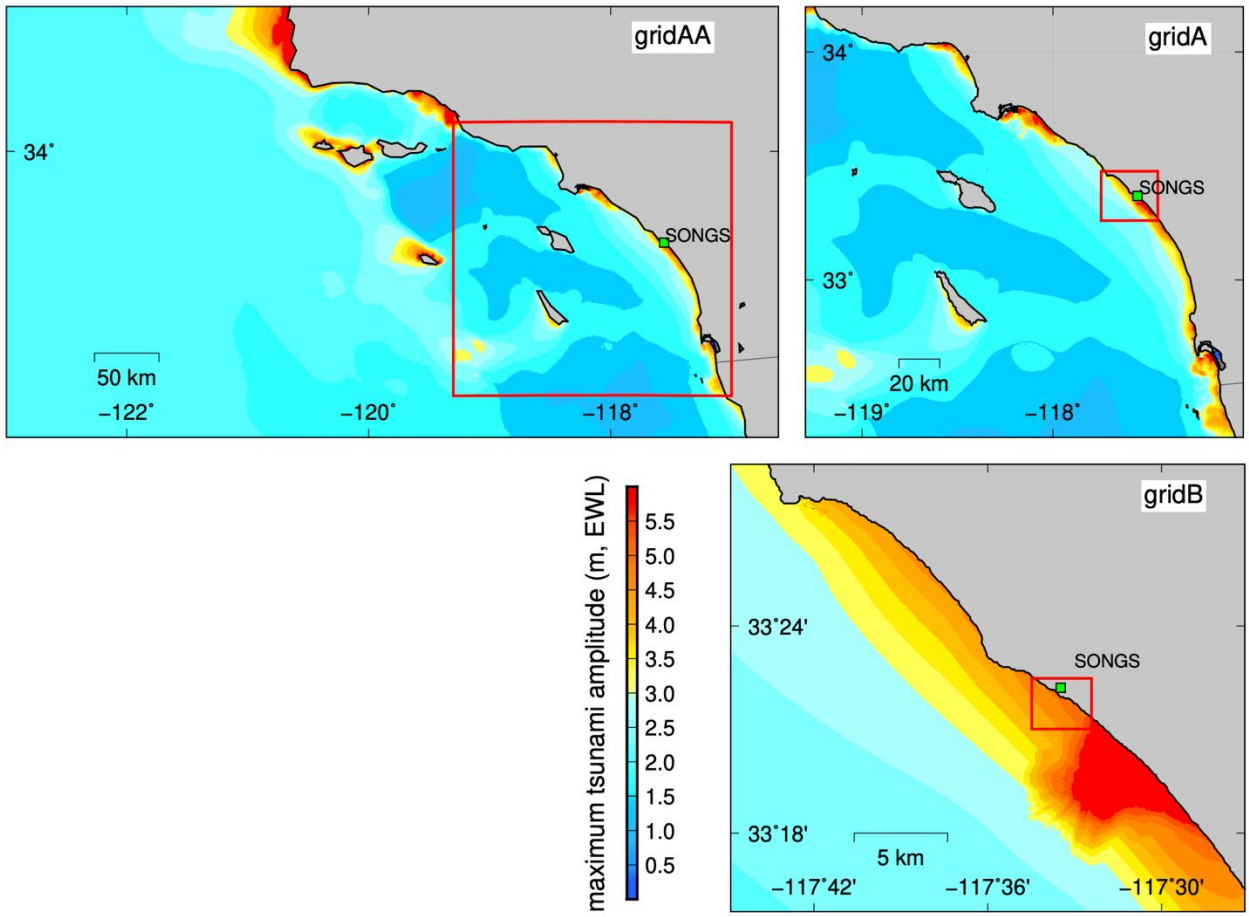


Figure 8-6. Maps showing the maximum tsunami amplitudes inside the domains of grids AA, A, and B during the numerical simulation of the Eastern Aleutian source EA-sc3 - see Table 7-3 for information on the sources.

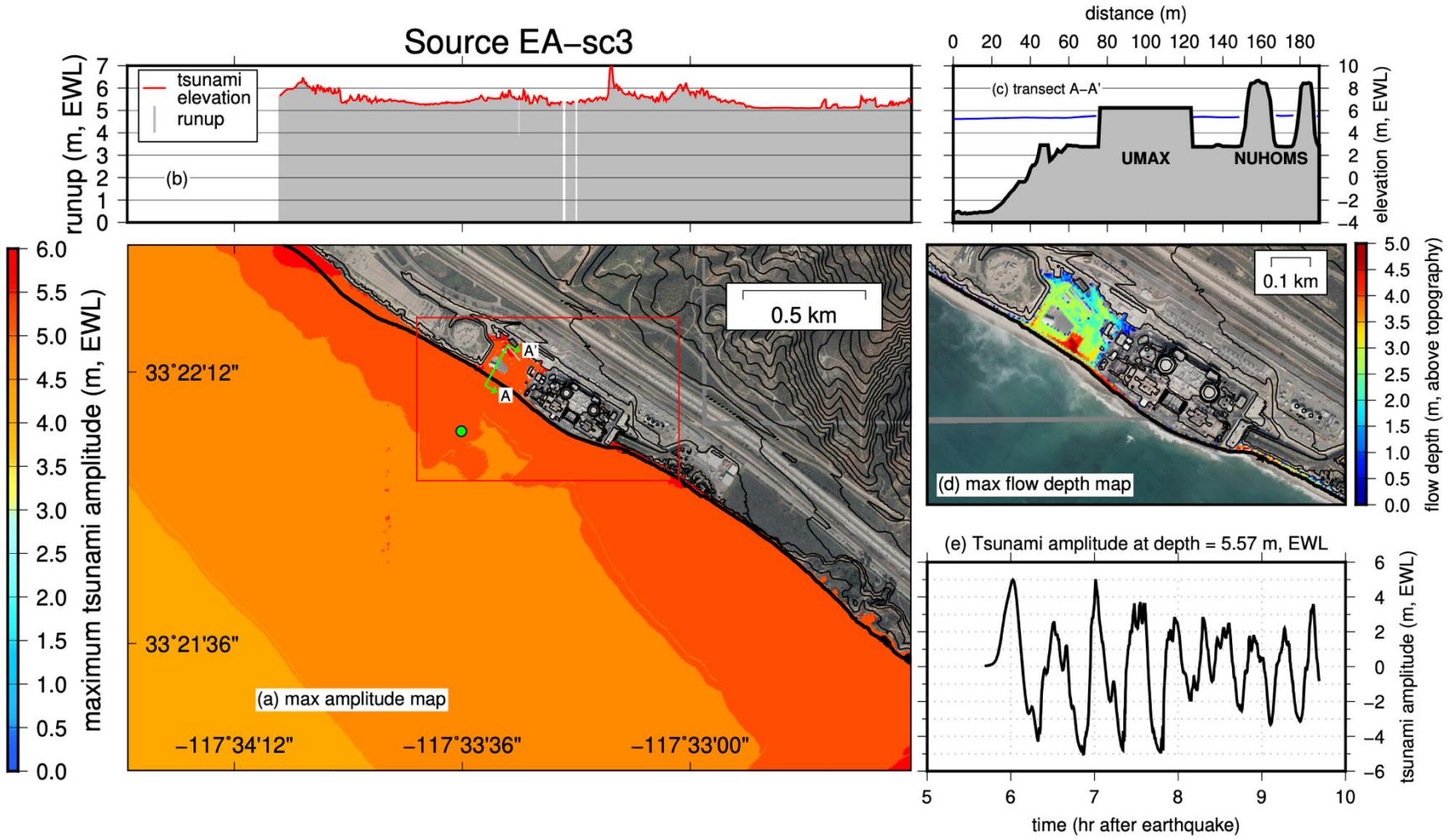


Figure 8-7. Numerical simulation results for the Eastern Aleutians seismic source EA-sc3. (a) Maximum tsunami amplitude across the domain of grid C. (b) Maximum runup and tsunami elevation distribution across the coastline in grid C. (c) Transect of maximum tsunami elevation across the SONGS site - see (a) for position of transect. (d) Maximum flow depth distribution across the SONGS site. (e) Time series of free surface elevation just offshore the SONGS site - time series extracted from the location shown with the green dot in (a).

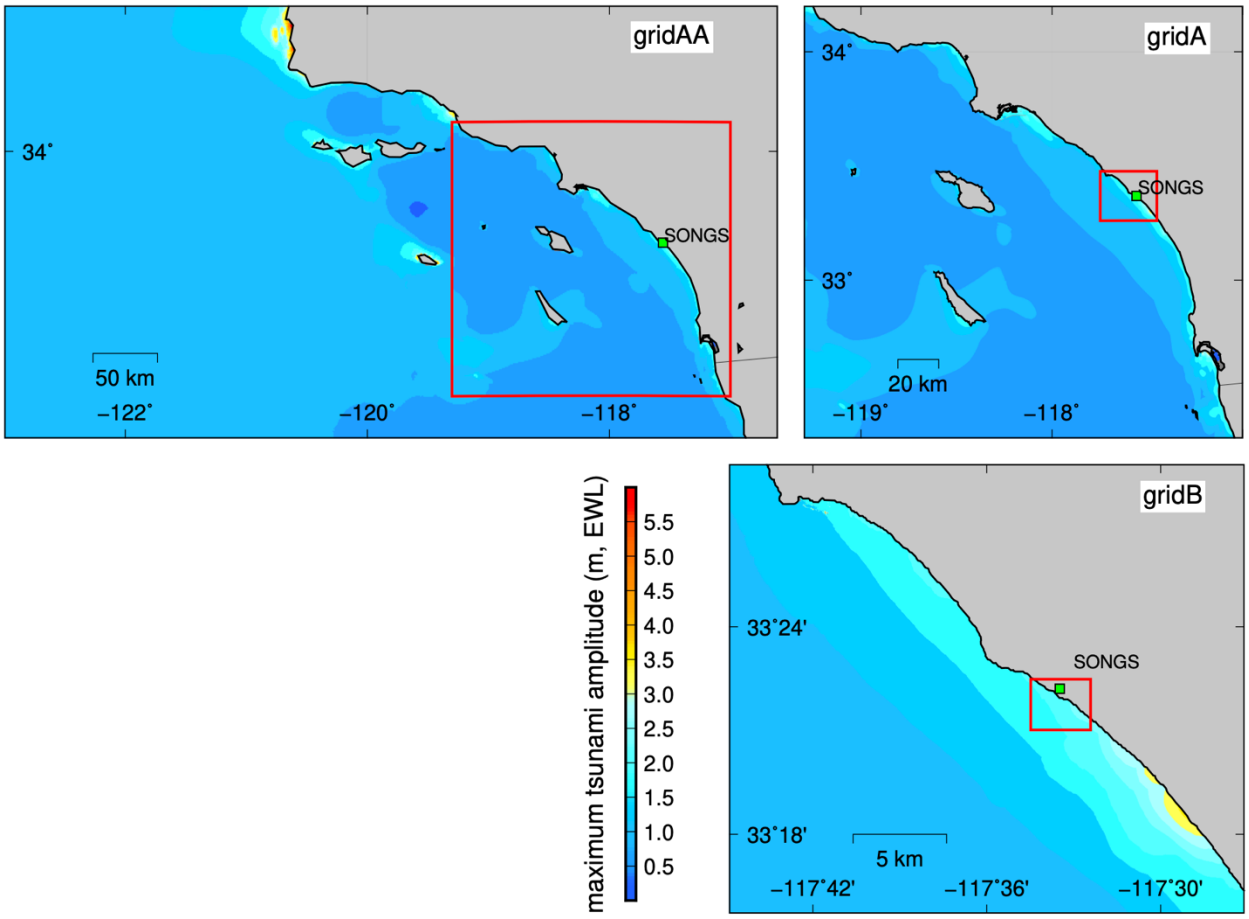


Figure 8-8. Maps showing the maximum tsunami amplitudes inside the domains of grids AA, A, and B during the numerical simulation of the Eastern Aleutian source EA-sc4 - see Table 7-3 for information on the sources.

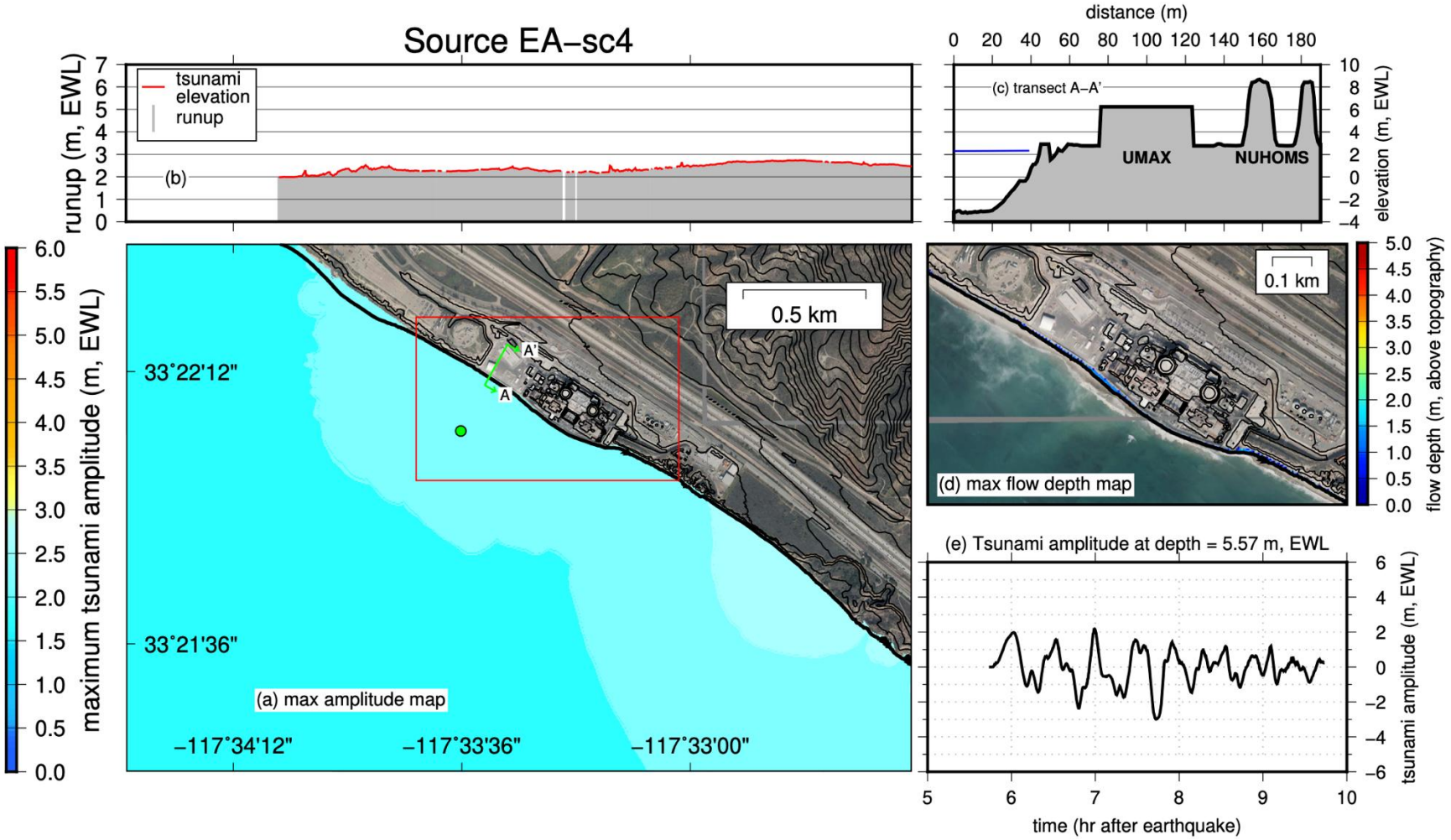


Figure 8-9. Numerical simulation results for the Eastern Aleutians seismic source EA-sc4. (a) Maximum tsunami amplitude across the domain of grid C. (b) Maximum runup and tsunami elevation distribution across the coastline in grid C. (c) Transect of maximum tsunami elevation across the SONGS site - see (a) for position of transect. (d) Maximum flow depth distribution across the SONGS site. (e) Time series of free surface elevation just offshore the SONGS site - time series extracted from the location shown with the green dot in (a).

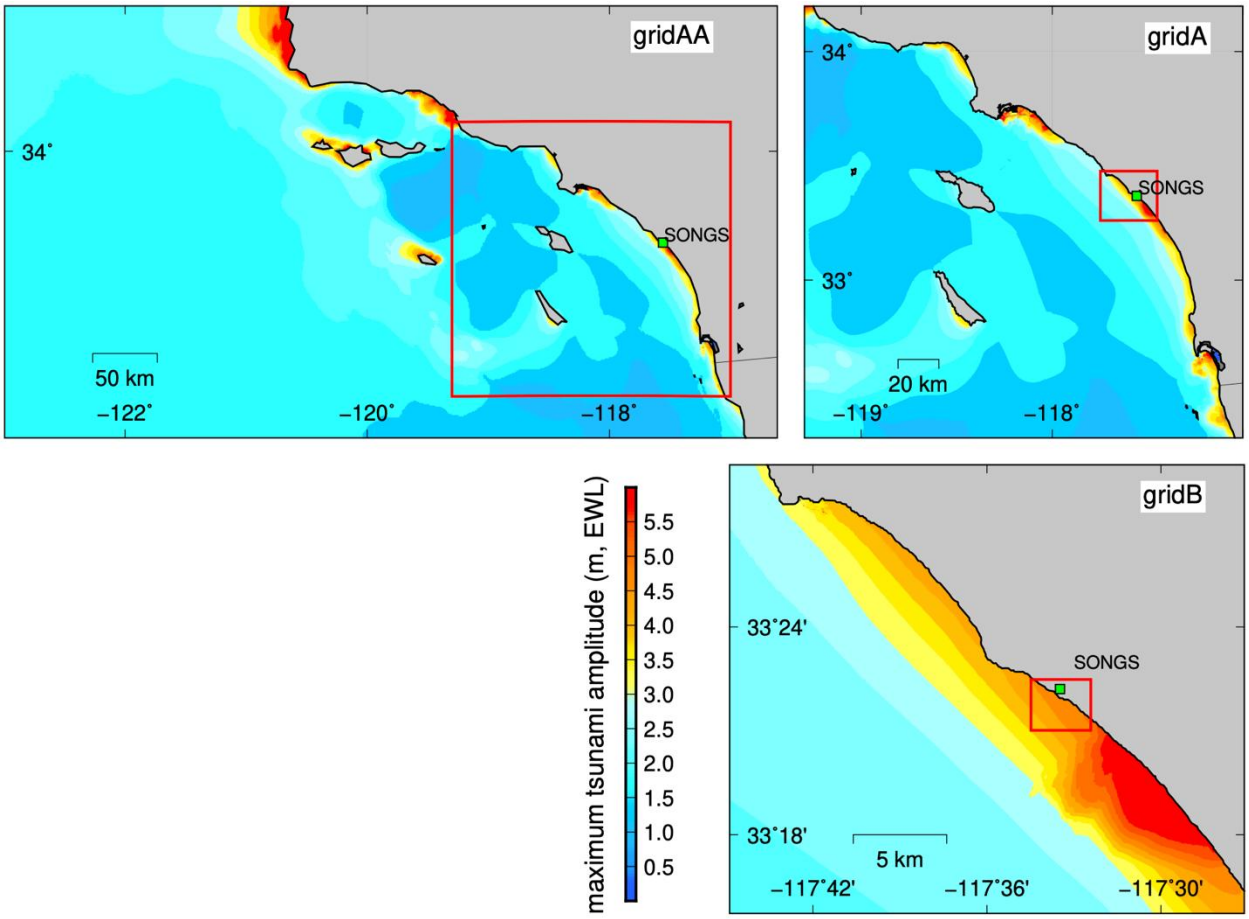


Figure 8-10. Maps showing the maximum tsunami amplitudes inside the domains of grids AA, A, and B during the numerical simulation of the Eastern Aleutian source EA-sc5 - see Table 7-3 for information on the sources.

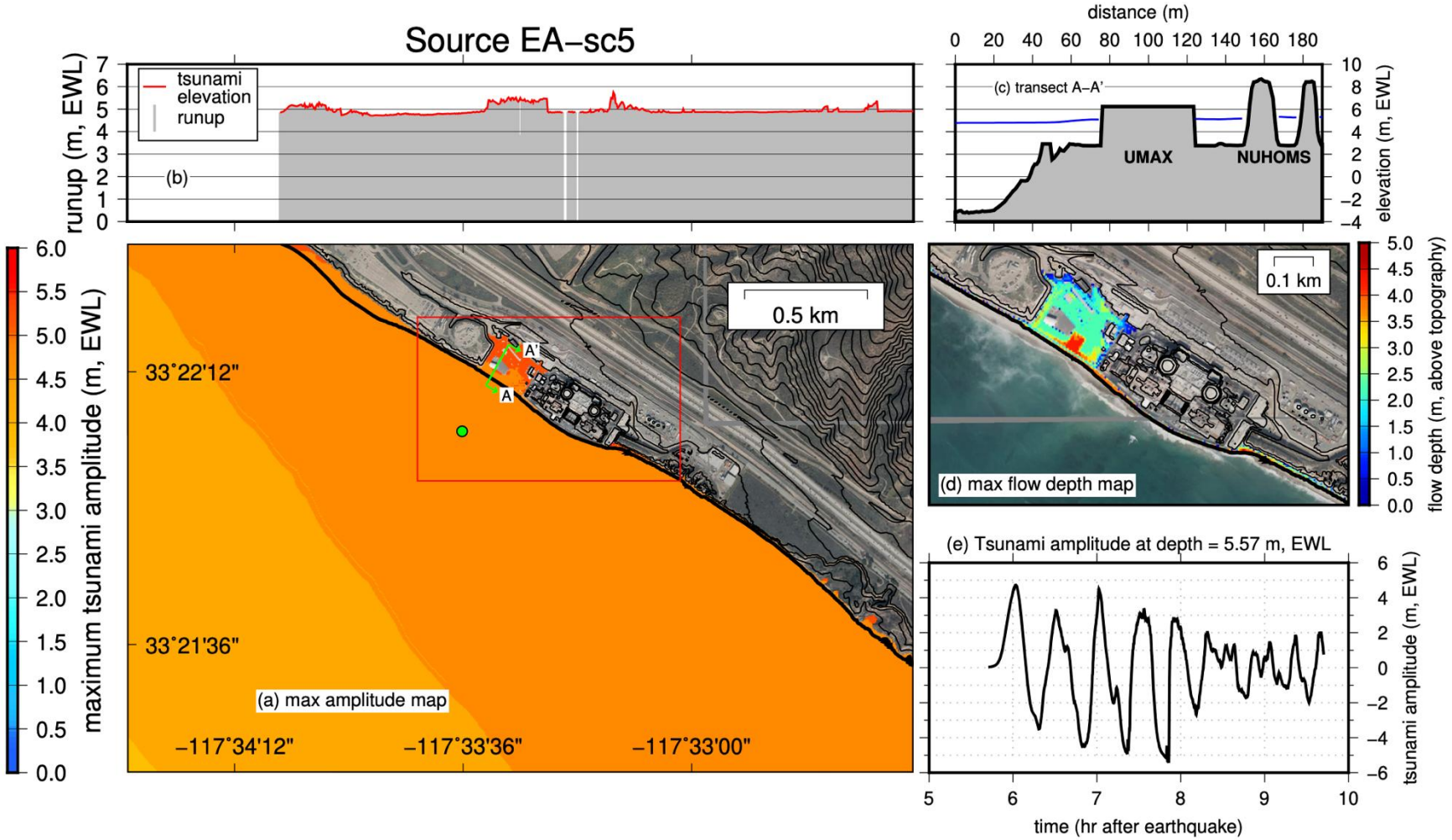


Figure 8-11. Numerical simulation results for the Eastern Aleutians seismic source EA-sc5. (a) Maximum tsunami amplitude across the domain of grid C. (b) Maximum runup and tsunami elevation distribution across the coastline in grid C. (c) Transect of maximum tsunami elevation across the SONGS site - see (a) for position of transect. (d) Maximum flow depth distribution across the SONGS site. (e) Time series of free surface elevation just offshore the SONGS site - time series extracted from the location shown with the green dot in (a).

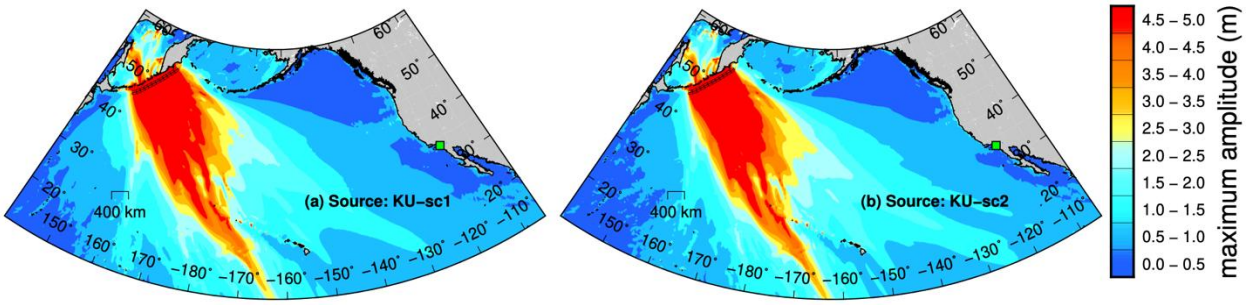


Figure 8-12. Maps showing the maximum tsunami amplitudes (in part of the spatial extent) of grid *P* from the numerical simulation of all two Kurils sources – see Table 7-3 for information on the sources.

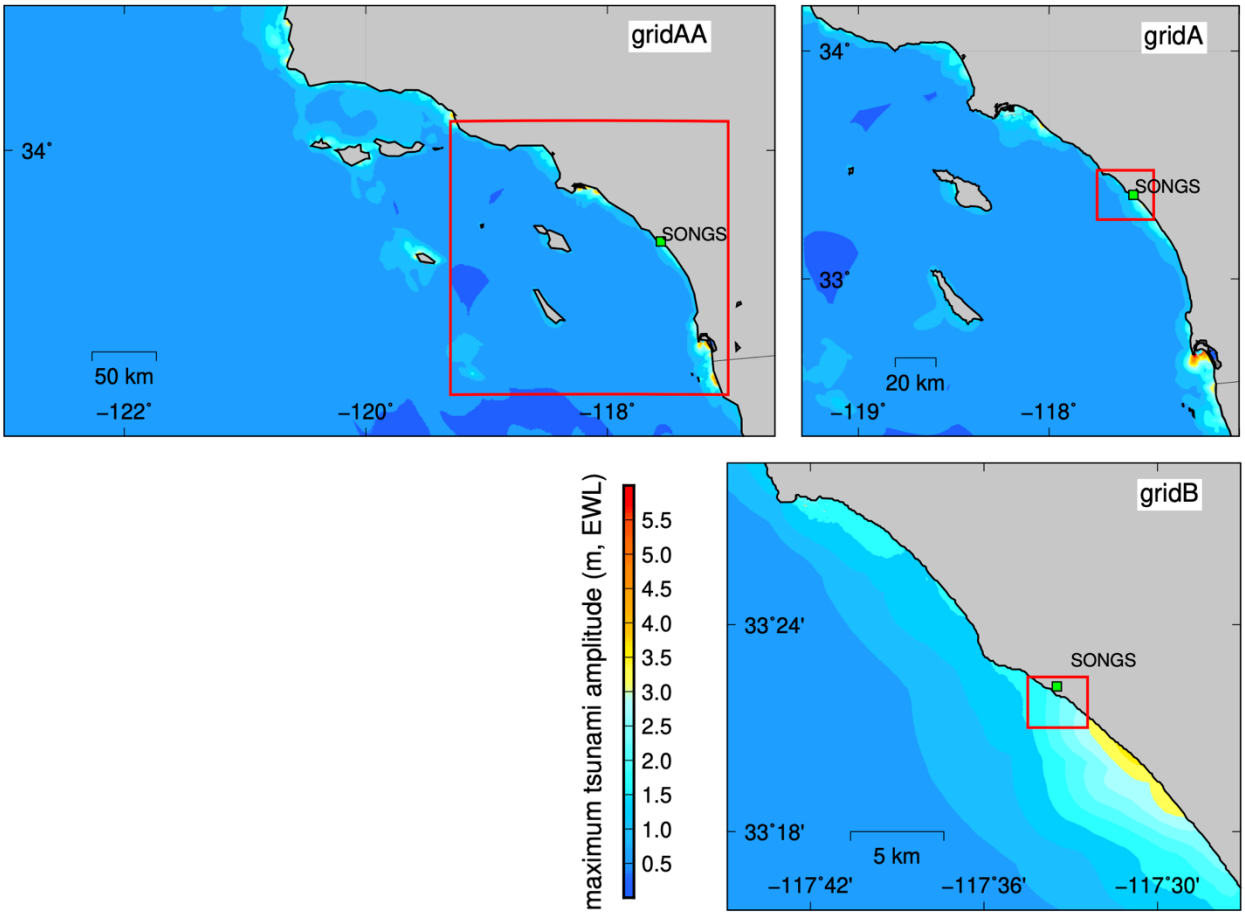


Figure 8-13. Maps showing the maximum tsunami amplitudes inside the domains of grids AA, A, and B during the numerical simulation of the Kurils source KU-sc1 - see Table 7-3 for information on the sources.

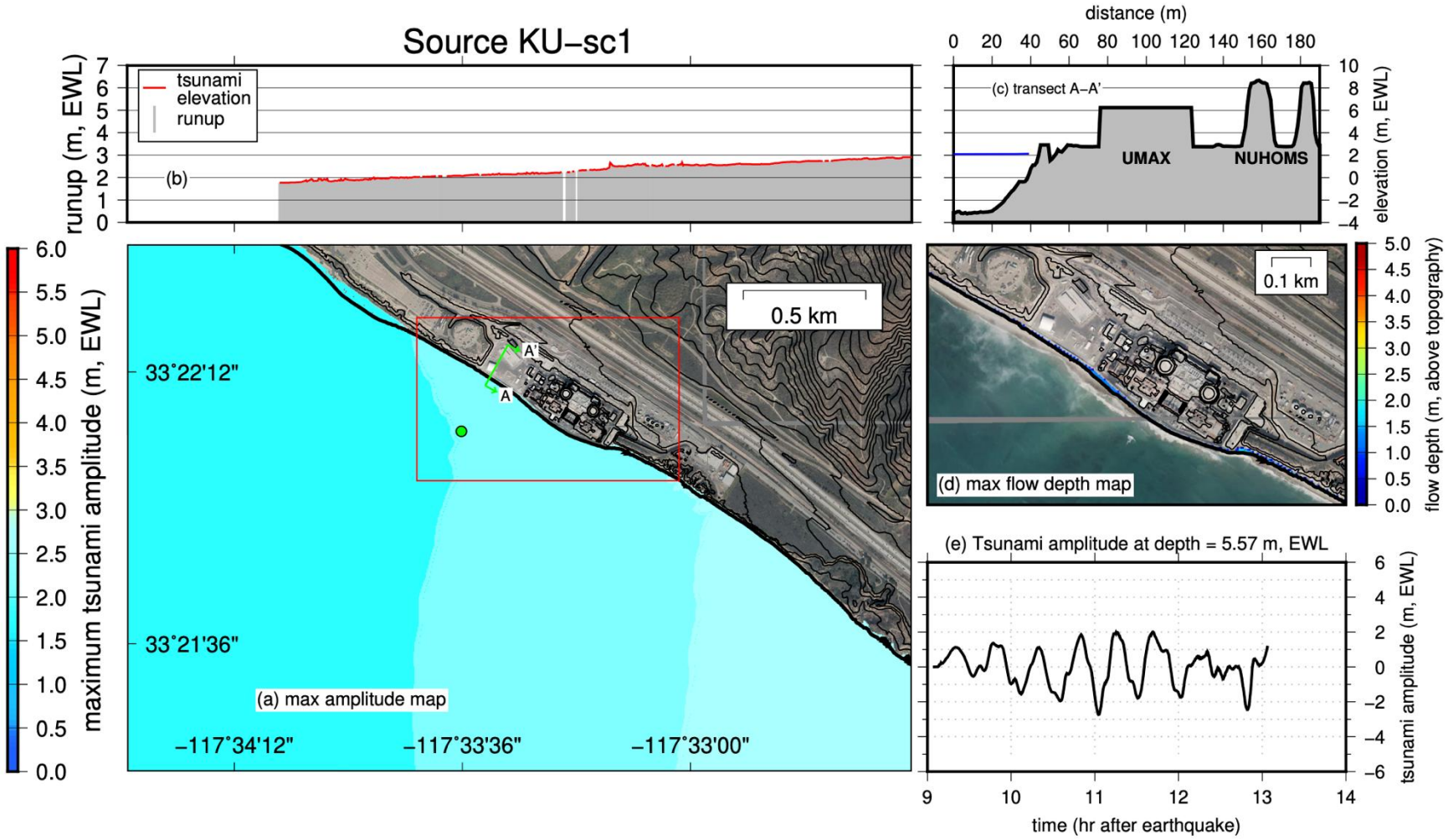


Figure 8-14. Numerical simulation results for the Kurils seismic source KU-sc1. (a) Maximum tsunami amplitude across the domain of grid C. (b) Maximum runup and tsunami elevation distribution across the coastline in grid C. (c) Transect of maximum tsunami elevation across the SONGS site - see (a) for position of transect. (d) Maximum flow depth distribution across the SONGS site. (e) Time series of free surface elevation just offshore the SONGS site - time series extracted from the location shown with the green dot in (a).

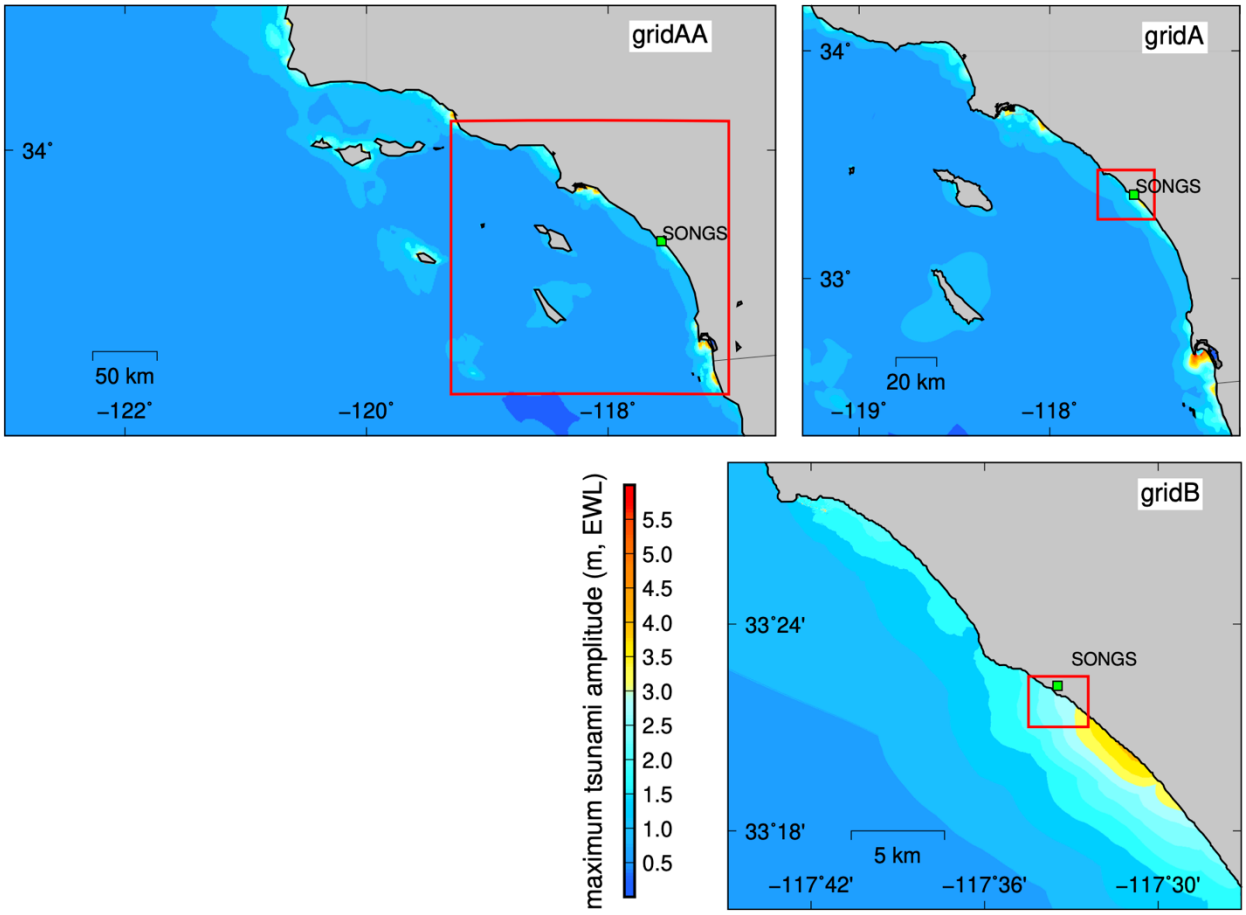


Figure 8-15. Maps showing the maximum tsunami amplitudes inside the domains of grids AA, A, and B during the numerical simulation of the Kurils source KU-sc2 - see Table 7-3 for information on the sources.

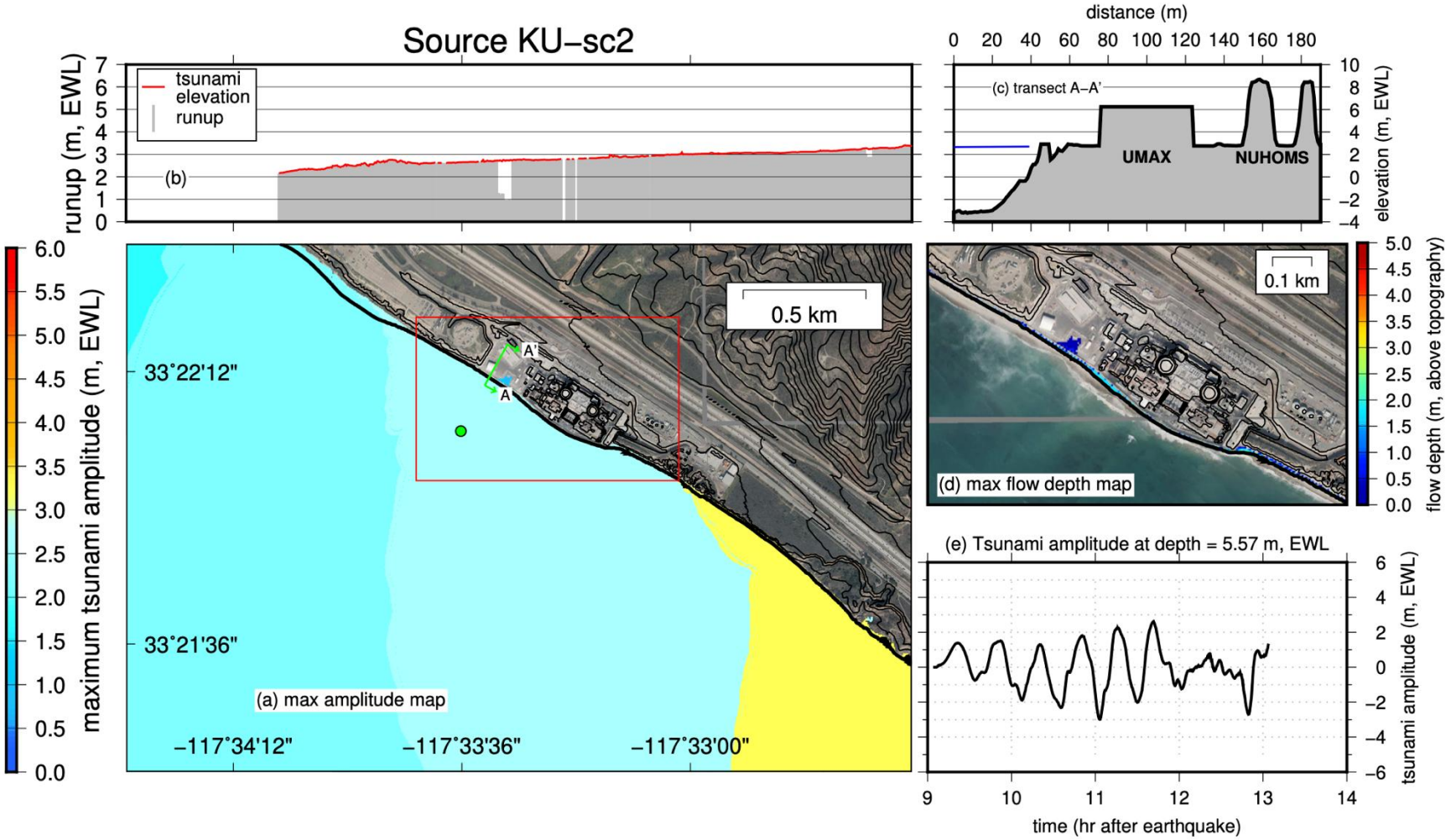


Figure 8-16. Numerical simulation results for the Kurils seismic source KU-sc2. (a) Maximum tsunami amplitude across the domain of grid C. (b) Maximum runup and tsunami elevation distribution across the coastline in grid C. (c) Transect of maximum tsunami elevation across the SONGS site - see (a) for position of transect. (d) Maximum flow depth distribution across the SONGS site. (e) Time series of free surface elevation just offshore the SONGS site - time series extracted from the location shown with the green dot in (a).

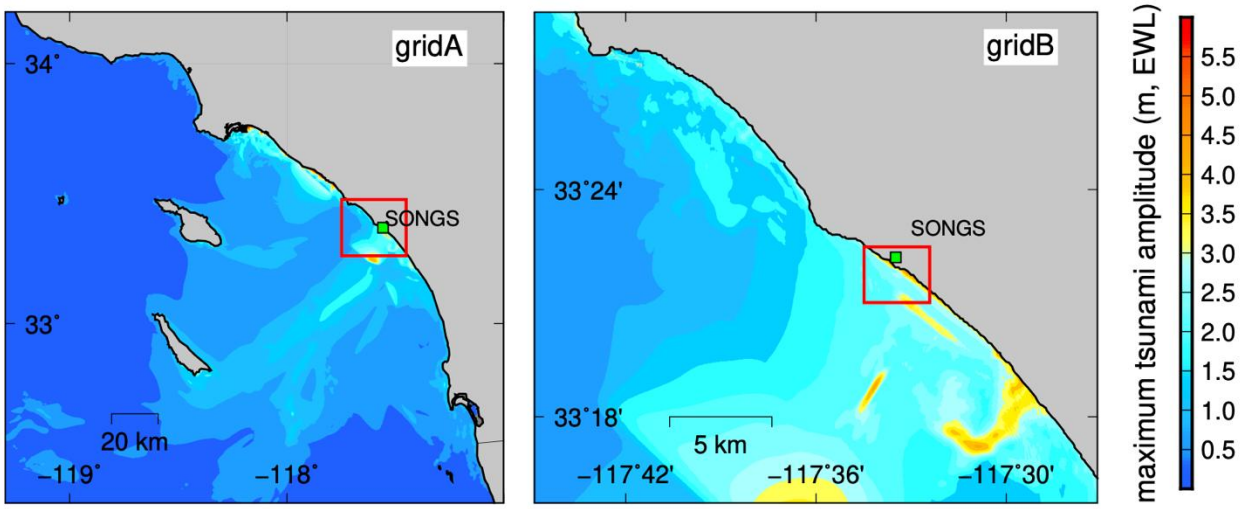


Figure 8-17. Maps showing the maximum tsunami amplitudes inside the domains of grids A and B during the numerical simulation of the near-field source Local-sc1 - see Table 7-5 for information on the sources.

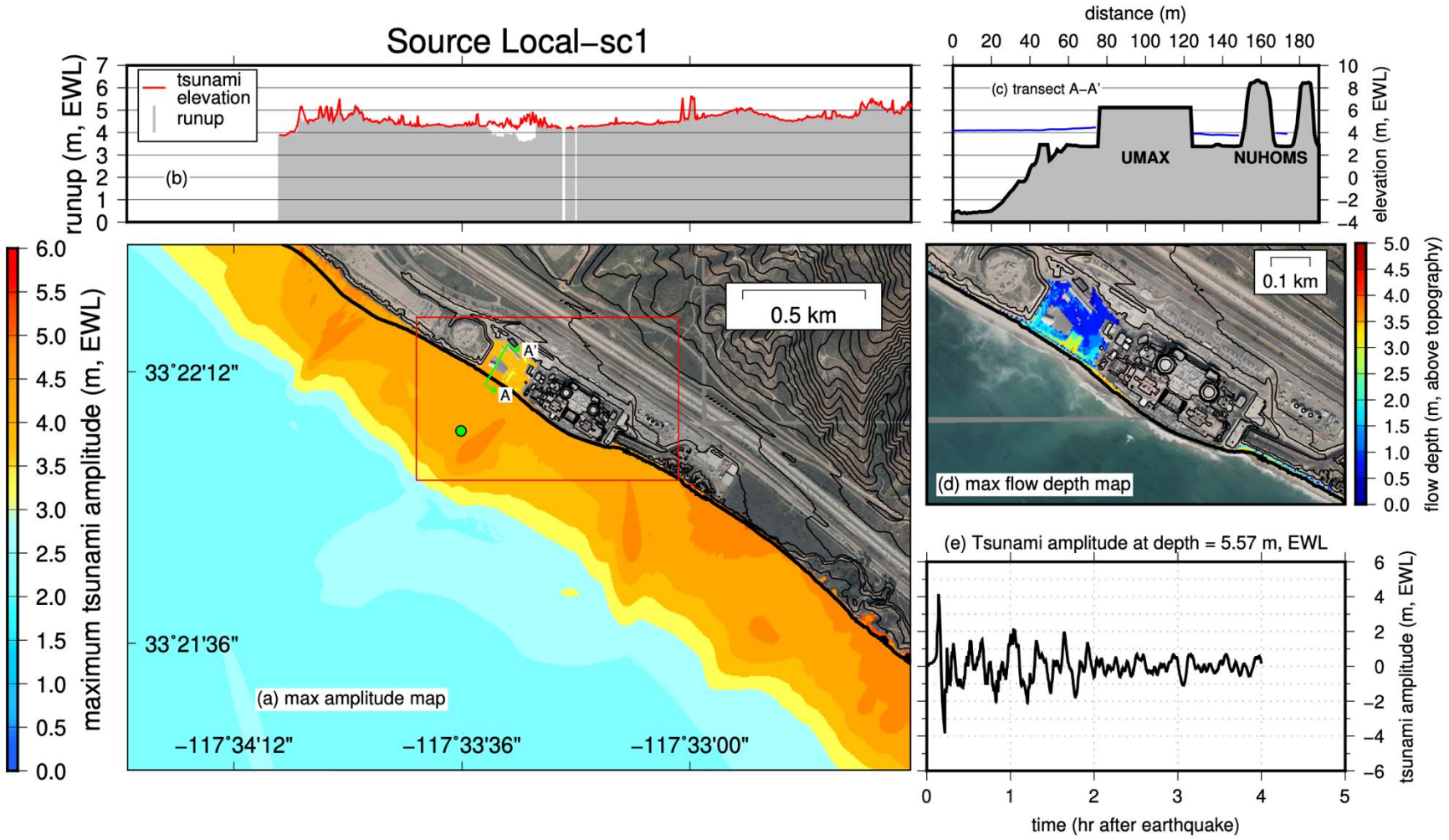


Figure 8-18. Numerical simulation results for the near-field seismic source Local-sc1. (a) Maximum tsunami amplitude across the domain of grid C. (b) Maximum runup and tsunami elevation distribution across the coastline in grid C. (c) Transect of maximum tsunami elevation across the SONGS site - see (a) for position of transect. (d) Maximum flow depth distribution across the SONGS site. (e) Time series of free surface elevation just offshore the SONGS site - time series extracted from the location shown with the green dot in (a).

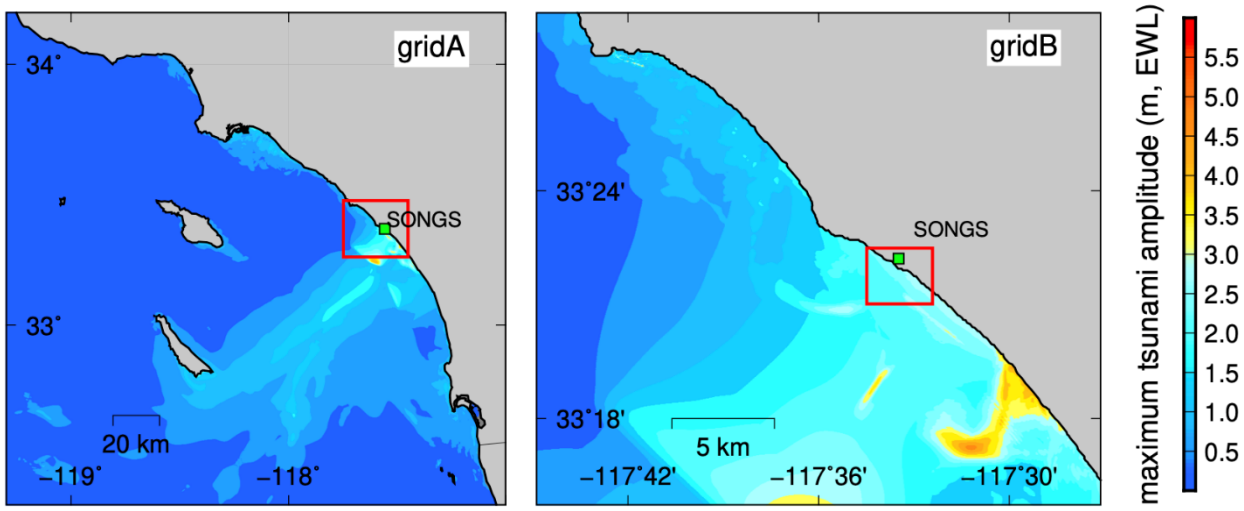


Figure 8-19. Maps showing the maximum tsunami amplitudes inside the domains of grids A and B during the numerical simulation of the near-field source Local-sc2 - see Table 7-5 for information on the sources.

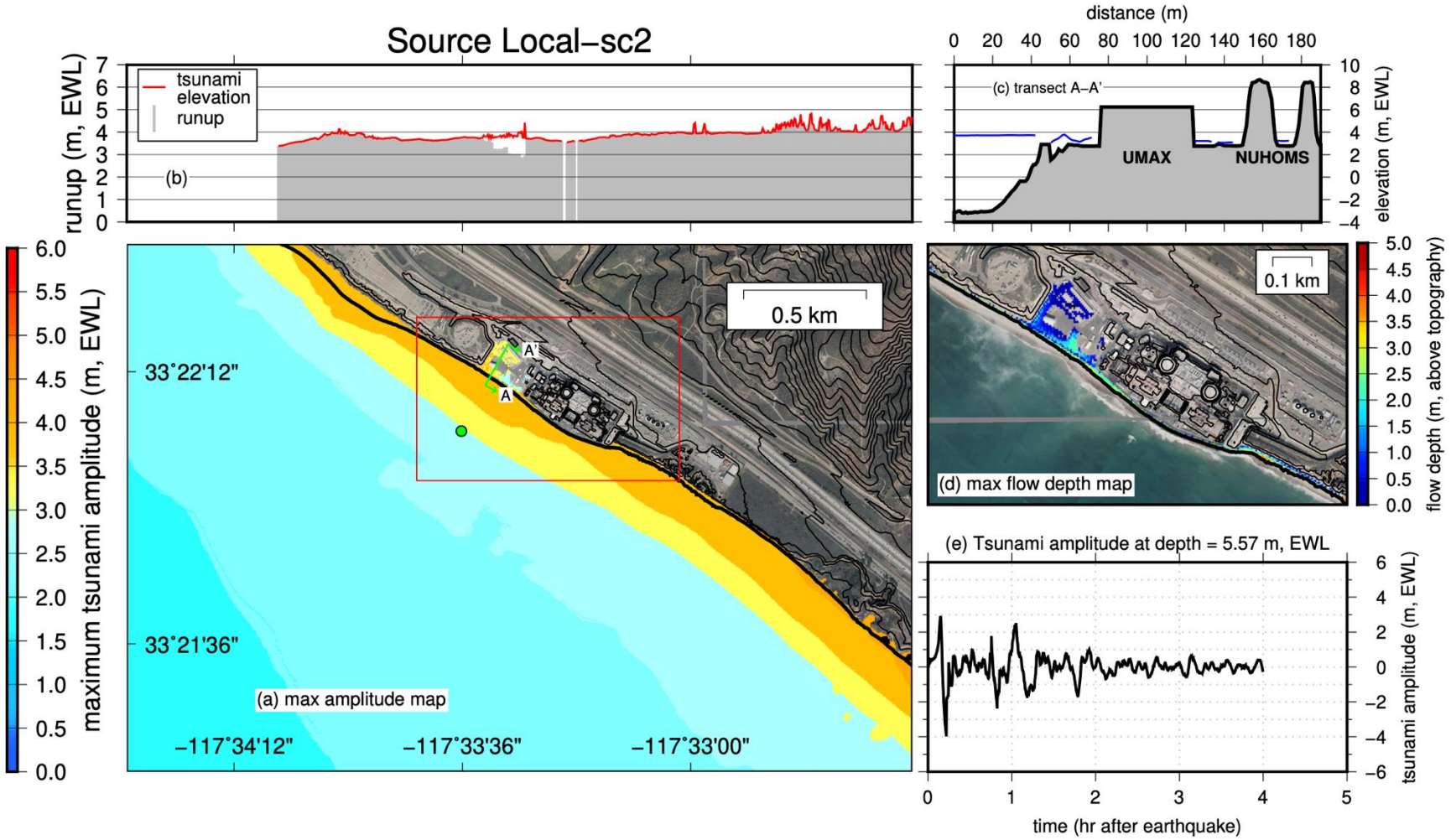


Figure 8-20. Numerical simulation results for the near-field seismic source Local-sc2. (a) Maximum tsunami amplitude across the domain of grid C. (b) Maximum runup and tsunami elevation distribution across the coastline in grid C. (c) Transect of maximum tsunami elevation across the SONGS site - see (a) for position of transect. (d) Maximum flow depth distribution across the SONGS site. (e) Time series of free surface elevation just offshore the SONGS site - time series extracted from the location shown with the green dot in (a).

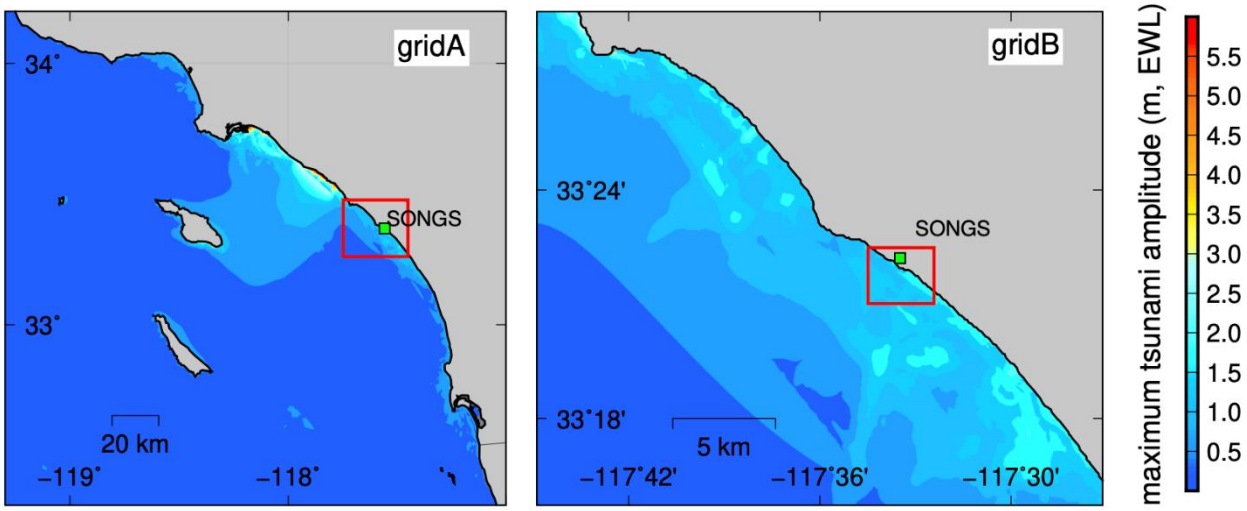


Figure 8-21. Maps showing the maximum tsunami amplitudes inside the domains of grids A and B during the numerical simulation of the near-field source Local-sc3 - see Table 7-5 for information on the sources.

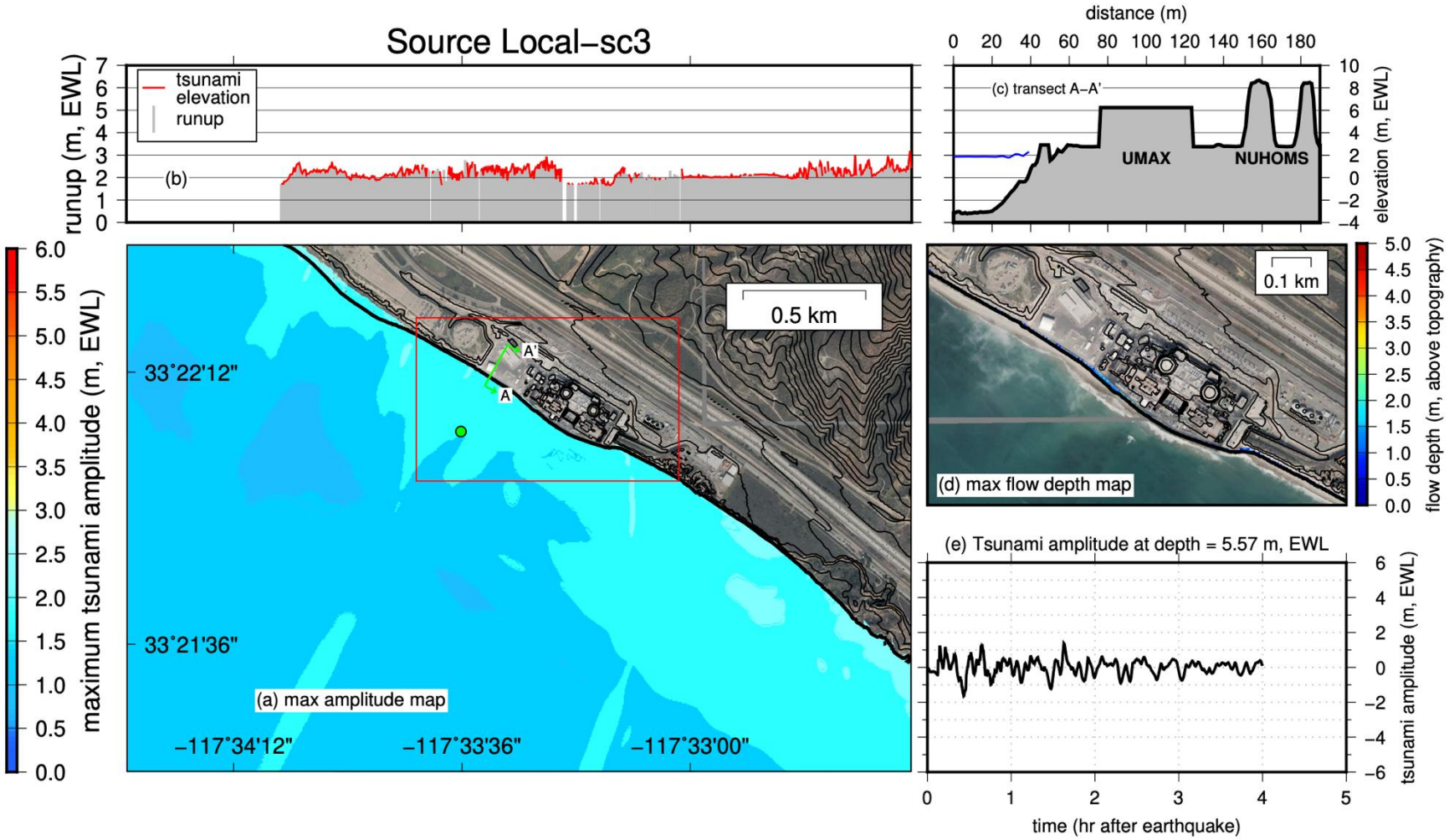


Figure 8-22. Numerical simulation results for the near-field seismic source Local-sc3. (a) Maximum tsunami amplitude across the domain of grid C. (b) Maximum runup and tsunami elevation distribution across the coastline in grid C. (c) Transect of maximum tsunami elevation across the SONGS site - see (a) for position of transect. (d) Maximum flow depth distribution across the SONGS site. (e) Time series of free surface elevation just offshore the SONGS site - time series extracted from the location shown with the green dot in (a).

9.0 RESULTS SUMMARY

The numerical results are summarized in Table 9-1. The largest tsunami amplitudes offshore, and the largest tsunami impact around the NUHOMS ISFSI from the sources studied resulted from the simulation of the Eastern Aleutian source EA-sc3, which is similar to the Eastern Aleutian source modeled by Shi et al. (2016). Source EA-sc3 produces maximum tsunami elevation and maximum flow depth values of ~9.1 m (MLLW) and ~2.8 m (above ground), respectively, around the NUHOMS ISFSI, which is ~3.7 m above ground.

From the three worst-case local seismic sources considered, the simulation of source Local-sc1 produces the highest offshore wave amplitudes (7.3 m, MLLW) and tsunami impact around the NUHOMS ISFSI, with maximum tsunami elevation of ~7.2 m (MLLW) and maximum flow depth of ~1.2 m (above ground).

Table 9-1. Table of maximum and minimum amplitudes occurring at the node offshore the SONGS site (with coordinates −117.56004°W, 33.36782°N), and the maximum tsunami elevation (TE) and flow depth (FD) values inside the NUHOMS polygon for all simulated tsunami events. Maximum (absolute) values are provided in boldface.

Source Name	Wave Amplitudes Offshore at 5.6 m (EWL) Depth			Values Inside NUHOMS Polygon		
	Min (m, EWL)	Max (m, EWL)	Max (m, MLLW)	Max TE (m, EWL)	Max TE (m, MLLW)	Max FD (m)
EA-sc1	-2.7	1.9	5.1	N/A	N/A	N/A
EA-sc2	-5.3	3.3	6.5	3.4	6.5	0.6
EA-sc3	-5.1	**5.0**	**8.2**	**5.9**	**9.1**	**2.8**
EA-sc4	-3.0	2.2	5.4	N/A	N/A	N/A
EA-sc5	**-5.4**	4.7	7.9	5.5	8.7	2.7
KU-sc1	-2.7	2.0	5.2	N/A	N/A	N/A
KU-sc2	-3.0	2.6	5.8	N/A	N/A	N/A
Local-sc1	-3.9	4.2	7.3	4.0	7.2	1.2
Local-sc2	-4.0	2.9	6.1	3.4	6.6	0.4
Local-sc3	-1.7	1.4	4.6	N/A	N/A	N/A

We note that we cannot directly compare our results with Shi et al. (2016), because it is unclear if they performed inundation computations. The maximum value given in their table (Table 5) is 6.66 m (MLLW) for the Eastern Aleutians far-field seismic source.

10.0 ABBREVIATIONS

CE	Coastal Environments, Inc.
CRM	NOAA/NGDC Coastal Relief Model
DEM	Digital Elevation Model
EWL	Extreme Water Level (extreme tidal, surge and wave setup level+ sea level rise projection)
GEBCO	General Bathymetric Chart of the Oceans
ISFSI	Independent Spent Fuel Storage Installation
MHW	Mean High Water datum
MLLW	Mean Low Lower Water datum
MSL	Mean Sea Level datum
MSLR	Mean Sea Level Rise
NCEI	National Centers for Environmental Information of NOAA
NCTR	NOAA Center for Tsunami Research
NGDC	National Geophysical Data Center of NOAA
NIRC	Newport-Inglewood-Rose Canyon
NOAA	National Oceanographic and Atmospheric Administration
NRC	Nuclear Regulatory Commission
NUHOMS	Eastern ISFSI at SONGS
OPC	Ocean Protection Council
PMEL	Pacific Marine Environmental Laboratory of NOAA
PTHA	Probabilistic Tsunami Hazard Assessment
SONGS	San Onofre Nuclear Generating Station

11.0 REFERENCES

Aki, K. and P.G. Richards, 1980. *Quantitative seismology: Theory and methods* (volume 842). Freeman, San Francisco, CA.

Ambraseys, N. and C. Synolakis, 2010. Tsunami catalogs for the eastern Mediterranean, revisited. *Journal of Earthquake Engineering*, 14(3), pp. 309-330.

Arcas, D., 2015. A tsunami forecast model for Santa Monica, California. *NOAA OAR Special Report Tsunami Forecast Series PMEL-140*, 22. doi: 10.7289/V5D50JX8. URL https://doi.org/10.7289/V5D50JX8.

Atwater, B.F., 1987. Evidence for great Holocene earthquakes along the outer coast of Washington state. *Science*, 236 (4804), pp. 942-944.

Atwater, B.F., S. Musumi-Rokkaku, K. Satake, Y. Tsuji, K. Ueda, and D.K. Yamaguchi, 2016. *The orphan tsunami of 1700: Japanese clues to a parent earthquake in North America*. University of Washington Press.

Barberopoulou, A., J.C. Borrero, B. Uslu, N. Kalligeris, J.D. Goltz, R.I. Wilson, and C.E. Synolakis, 2009. New maps of California to improve tsunami preparedness. *Eos, Transactions American Geophysical Union*, 90(16), pp. 137–138. URLhttp://www.tsunamiresearchcenter.com/wp-content/uploads/2010/10/2009EOS_TsunamiMaps. pdf.

Barberopoulou, A., M.R. Legg, B. Uslu, and C.E. Synolakis, 2011. Reassessing the tsunami risk in major ports and harbors of California: San Diego. *Natural Hazards*, 58(1), pp. 479-496.

Beauducel, F., 2011. *Okada: Surface deformation due to a finite rectangular source*. MATLAB Central File Exchange. Last updated on 2011-03-06. URL https://www.mathworks.com/matlabcentral/fileexchange/ 25982-okada-surface-deformation-due-to-a-finite-rectangular-source.

Bird, P., 2003. An updated digital model of plate boundaries. *Geochemistry, Geophysics, Geosystems*, 4(3).

Borrero, J.C., 2002. *Tsunami hazards in southern California*. PhD thesis.

Borrero, J.C., J.F. Dolan, and C.E. Synolakis, 2001. Tsunamis within the eastern Santa Barbara channel. *Geophysical Research Letters*, 28(4), pp. 643-646.

Borrero, J.C., M.R. Legg, and C.E. Synolakis, 2004. Tsunami sources in the southern California Bight. *Geophysical Research Letters*, 31(13), L13211.

Brothers, D.S., K.L. Maier, J.W. Kluesner, J.E. Conrad, and J.D. Chaytor, 2019. The Santa Cruz basin submarine landslide complex, southern California: Repeated failure of uplifted basin sediment. *Journal of Sedimentary Research*, 17 (1), pp. 117-134.

Clarke, S.H., H.G. Greene, M.P. Kennedy, and J.G. Vedder, 1987. Geologic map of the inner-southern California continental margin. *California Continental Margin Geologic Map Series*, Area 1 of 7, sheet 1 of 4, scale 1:250,000, California Division of Mines and Geology.

Derakhti, M., R.A. Dalrymple, E.A. Okal, and C.E. Synolakis, 2019. Temporal and topographic source effects on tsunami generation. *Journal of Geophysical Research: Oceans*, 124(7), pages 5270-5288.

Eisner, R.K., J.C. Borrero, and C.E. Synolakis, 2001. *Inundation maps for the State of California*. NOAA/Pacific Marine Environmental Laboratory. http://www.tsunamiresearchcenter.com/wp-content/uploads/2010/11/2001ITS_CalinundationMaps.pdf.

Fletcher, J.M., O.J. Teran, T.K. Rockwell, M.E. Oskin, K.W. Hudnut, K.J. Mueller, R.M. Spelz, S.O. Akciz, E. Masana, G. Faneros, et al., 2014. Assembly of a large earthquake from a complex fault system: Surface rupture kinematics of the 4 April 2010 El Mayor-Cucapah (Mexico) mw 7.2 earthquake. *Geosphere*, 10(4), pages 797-827.

GEBCO, 2021. Gebco 2021 grid. URL https://doi.org/10.5285/c6612cbe-50b3-0cff-e053-6c86abc09f8f.

Geopentech, 2010. *Probabilistic tsunami hazard analysis report, draft*. Prepared for Southern California Edison, May 16.

Grant, L.B., L.J. Ballenger, and E.E. Runnerstrom, 2002. Coastal uplift of the San Joaquin hills, southern Los Angeles basin, California, by a large earthquake since AD 1635. *Bulletin of the Seismological Society of America*, 92(2), pp. 590-599.

Hamling, I.J., S. Hreinsd´ottir, K. Clark, J. Elliott, C. Liang, E. Fielding, N. Litchfield, P. Villamor, L. Wallace, T.J. Wright, et al., 2017. Complex multifault rupture during the 2016 m w 7.8 Kaikoura earthquake, New Zealand. *Science*, 356(6334).

Hanks, T.C. and H. Kanamori, 1979. A moment magnitude scale. *Journal of Geophysical Research: Solid Earth*, 84(B5), pages 2348-2350.

Hauksson, E., W. Yang, and P.M. Shearer, 2012. Waveform relocated earthquake catalog for southern California (1981 to June 2011). *Bulletin of the Seismological Society of America*, 102(5), pages 2239-2244.

Houston, J.R., 1980. *Type 19 flood insurance study: Tsunami predictions for southern California (*volume 80). U.S. Army Corps of Engineers Waterways Experiment Station.

Houston, J.R. and A.W. Garcia, 1974. *Type 16 flood insurance study: Tsunami predictions for Pacific coastal communities* (volume 74). U.S. Army Corps of Engineers Waterways Experiment Station.

Janenko, N.N., 1971. *The method of fractional steps (*volume 160). Springer.

Johnson, J.M., K. Satake, S.R. Holdahl, and J. Sauber, 1996. The 1964 Prince William sound earthquake: Joint inversion of tsunami and geodetic data. *Journal of Geophysical Research: Solid Earth*, 101(B1), pages 523-532.

Kirby, S., E.L. Geist, W.H.K. Lee, D. Scholl, and R. Blakely, 2006. *Tsunami source characterization for western Pacific subduction zones: A preliminary report.* Tsunami sources workshop.

Kirby, S., D. Scholl, R.E. von Huene, and R. Wells, 2013. *Alaska earthquake source for the SAFRR tsunami scenario: Chapter B in the SAFRR (Science Application for Risk Reduction) tsunami scenario*. Technical report, US Geological Survey.

Legg, M.R., 1985. *Geologic structure and tectonics of the inner continental borderland offshore Northern Baja California, Mexico (Wrench Faults, San Diego, Ensenada).* PhD thesis, University of California, Santa Barbara.

Legg, M.R., V. Wong-Ortega, and F. Suarez-Vidal, 1991. Geologic structure and tectonics of the inner continental borderland of northern Baja California. In Dauphin, P., and G. Ness, editors, *The Gulf and Peninsular Province of the Californias. American Association of Petroleum Geologists Memoir* #47, pages 145-177.

Legg, M.R. and M.J. Kamerling, 2003. Large-scale basement-involved landslides, California Continental Borderland. In *Landslide Tsunamis: Recent Findings and Research Directions*, pages 2033–2051. Springer.

Legg, M.R., J.C. Borrero, and C.E. Synolakis, 2004. Tsunami hazards associated with the Catalina fault in southern California. *Earthquake Spectra*, 20(3), pages 917-950.

Legg, M., C. Sorlien, C. Nicholson, M. Kamerling, and G. Kuhn, 2018. Potential for large complex multi-fault earthquakes offshore southern California. In *Proceedings of the 11th National Conference in Earthquake Engineering, Earthquake Engineering Research Institute, Los Angeles, CA.*

Maloney, J.M., N. Driscoll, G. Kent, S. Duke, T. Freeman, J. Bormann, R. Anderson, and H. Ferriz, 2016. Segmentation and step-overs along strike-slip fault systems in the inner California borderlands: Implications for fault architecture and basin formation. *Applied Geology in California, Environmental Engineering Geologists*, 26, pages 655-677.

McCarthy, R.J., E.N. Bernard, and M.R. Legg, 1993. The Cape Mendocino earthquake: A local tsunami wakeup call? In *Coastal Zone'93*, pages 2812-2828. ASCE.

McCulloch, D.S., 1985. Evaluating tsunami potential. *USGS Prof. Paper*, 1360, pages 374-413.

NOAA/NGDC, 2003. *U.S. Coastal Relief Model* (volume 6, southern California). NOAA/ National Centers for Environmental Information. doi: 10.7289/V500001J. https://doi.org/10.7289/V500001J.

NOAA/NGDC, 2010. *One-third arc-second NAVD 88 coastal digital elevation model, San Diego, CA.* NOAA/National Centers for Environmental Information. https://*www*.ncei.noaa.gov/metadata/geoportal/rest/metadata/ item/gov.noaa.ngdc.mgg.dem:3542/html#.

Okada, Y., 1985. Surface deformation due to shear and tensile faults in a half-space. *Bulletin of the Seismological Society of America*, 75(4), pages 1135-1154.

Ocean Protection Council, 2018. State of California sea level rise guidance, 2018 update. *California Natural Resources Agency Ocean Protection Council.* 84 pages.

Percival, D.B., D. Arcas, D.W. Denbo, M.C. Eble, E. Gica, H.O. Mofjeld, M.C. Spillane, L. Tang, and V.V. Titov, 2009. Extracting tsunami source parameters via inversion of dart buoy data. NOAA technical memorandum. *OAR PMEL-144*, p. 22.

Rivero, C. and J.H. Shaw, 2011. *Active Folding and Blind Thrust Faulting Induced by Basin Inversion Processes, Inner California Borderlands*.

Rivero, C., J.H. Shaw, and K. Mueller, 2000. Oceanside and Thirty-Mile Bank blind thrusts: Implications for earthquake hazards in coastal southern California. *Geology*, 28(10), pages 891-894.

Satake, K., K. Shimazaki, Y. Tsuji, and K. Ueda, 1996. Time and size of a giant earthquake in Cascadia inferred from Japanese tsunami records of January 1700. *Nature*, 379(6562), pages 246-249.

Shi, F., J.T. Kirby, and L. Young, 2016. *SONGS Calculations for Probable Maximum Tsunami.* Technical report, CH2M Hill, Calculation No. 458144-CALC-004.

Smith, W.H.F. and D.T. Sandwell, 1994. Bathymetric prediction from dense satellite altimetry and sparse shipboard bathymetry. *Journal of Geophysical Research: Solid Earth*, 99(B11), pages 21803-21824.

Soloviev, S.L., 1970. Recurrence of tsunamis in the pacific. *Tsunamis in the Pacific Ocean*.

Sorlien, C.C., J. T. Bennett, M.-H. Cormier, B. A. Campbell, C. Nicholson, and R. L. Bauer, 2016. Late-Miocene-Quaternary fault evolution and interaction in the southern California Inner Continental Borderland. *Geosphere*, 11, pages 1111-1132.

Synolakis, C.E., D. McCarthy, V.V. Titov, and J. Borrero, 1998. Evaluating the tsunami risk in California. In *California and the World Ocean'97: Ocean Resources, An Agenda for the Future*, pages 1225-1236. ASCE.

Synolakis, C.E., J.-P. Bardet, J.C. Borrero, H.L. Davies, E.A. Okal, E.A. Silver, S. Sweet, and D.R. Tappin, 2002a. The slump origin of the 1998 Papua New Guinea tsunami. *Proceedings of the Royal Society of London, Series A: Mathematical, Physical and Engineering Sciences*, 458(2020), pages 763-789.

Synolakis, C.E., J. Borrero, and R. Eisner, 2002b. Developing inundation maps for southern California. In *Solutions to Coastal Disasters' 02*, pages 848-862.

Synolakis, C.E., 2003. Tsunami and seiche. *Earthquake Engineering Handbook*, 9:1–9.

Synolakis, C.E. and E.N. Bernard, 2006. Tsunami science before and beyond Boxing Day 2004. *Philosophical Transactions of the Royal Society A: Mathematical, Physical and Engineering Sciences*, 364(1845), pages 2231-2265.

Synolakis, C.E., E.N. Bernard, V.V. Titov, U. Kânoğlu, and F.I. Gonzalez, 2008. Validation and verification of tsunami numerical models. In *Tsunami Science Four Years After the 2004 Indian Ocean Tsunami*, pages 2197-2228. Springer.

Synolakis, C.E. and U. Kânoğlu, 2015. The Fukushima accident was preventable. *Philosophical Transactions of the Royal Society A: Mathematical, Physical and Engineering Sciences*, 373(2053), 20140379.

Thio, H.K., P. Somerville, and J. Polet, 2010. *Probabilistic tsunami hazard in California*. Pacific Earthquake Engineering Research Center, Peer Report 2010/108. University of California, Berkeley. http://peer.berkeley. edu/publications/peer_reports.html.

Titov, V.V. and C.E. Synolakis, 1995. Modeling of breaking and nonbreaking long-wave evolution and runup using vtcs-2. *Journal of Waterway, Port, Coastal, and Ocean Engineering*, 121(6), pages 308-316.

Titov, V.V. and C.E. Synolakis, 1997. Extreme inundation flows during the Hokkaido-nansei-oki tsunami. *Geophysical Research Letters*, 24(11), pages 1315-1318.

Titov, V.V. and C.E. Synolakis, 1998. Numerical modeling of tidal wave runup. *Journal of Waterway, Port, Coastal, and Ocean Engineering*, 124(4), pages 157-171.

Titov, V.V., H.O. Mofjeld, F.I. Gonzalez, and J.C. Newman, 1999. *Offshore forecasting of Alaska-Aleutian subduction zone tsunamis in Hawaii.* NOAA Technical Memorandum, ERL PMEL-114, PMEL, Seattle, WA, 2.

Titov, V.V., C.W. Moore, D.J.M. Greenslade, C. Pattiaratchi, R. Badal, C.E. Synolakis, and U. Kˆanoˇglu, 2011. A new tool for inundation modeling: Community modeling interface for tsunamis (commit). *Pure and Applied Geophysics*, 168(11), pages 2121-2131.

Titov, V., U. Kânoğlu, and C. Synolakis, 2016. Development of most for real-time tsunami forecasting. *Journal of Waterway, Port, Coastal, and Ocean Engineering*, 142(6), 03116004.

Uslu, B., 2008. *Deterministic and probabilistic tsunami studies in California from near and far field sources*. PhD thesis, University of Southern California.

APPENDIX A

NOAA/PMEL UNIT SOURCE PARAMETERS

NOAA/PMEL UNIT SOURCE PARAMETERS

This section lists the earthquake parameters of the NOAA/PMEL unit sources used to define the far-field sources as listed by Arcas (2015). Table A-1 lists the earthquake parameters of the NOAA/PMEL unit sources used with the Eastern Aleutians far-field sources, and Table A-2 lists the unit sources used with the Kuril far-field sources. All unit sources used have a rake angle of 90^o, rupture length L = 100 km and rupture width W = 50 km. Longitude/Latitude correspond to the coordinates of the center of the down-dip edge of the unit sources. The Depth parameter corresponds to the depth of the up-dip edge of the unit sources.

Table A-1. Earthquake parameters for the Aleutian-Alaska-Cascadia Subduction Zone (acsz) NOAA/PMEL unit sources (Arcas, 2015).

Unit Source Name	Longitude (°E)	Latitude (°N)	Strike (°)	Dip (°)	Depth (km)
acsz-a25	196.434	54.076	250.0	15.0	17.94
acsz-b25	196.693	53.6543	250.0	15.0	5.0
acsz-a26	197.897	54.36	253.0	15.0	17.94
acsz-b26	198.12	53.93	253.0	15.0	5.0
acsz-a27	199.434	54.596	256.0	15.0	17.94
acsz-b27	199.62	54.16	256.0	15.0	5.0
acsz-a28	200.882	54.83	253.0	15.0	17.94
acsz-b28	201.108	54.4	253.0	15.0	5.0
acsz-a29	202.261	55.133	247.0	15.0	17.94
acsz-b29	202.565	54.72	247.0	15.0	5.0
acsz-a30	203.604	55.509	240.0	15.0	17.94
acsz-b30	203.997	55.12	240.0	15.0	5.0
acsz-w30	201.9901	56.9855	239.5195	15.0	69.12
acsz-x30	202.3851	56.6094	239.8491	15.0	56.24
acsz-y30	202.7724	56.232	240.1722	15.0	43.82
acsz-z30	203.1521	55.8534	240.4869	15.0	30.88
acsz-a31	204.895	55.97	236.0	15.0	17.94
acsz-b31	205.34	55.598	236.0	15.0	5.0
acsz-w31	203.0825	57.374	234.544	15.0	69.12
acsz-x31	203.5408	57.0182	234.9266	15.0	56.24
acsz-y31	203.9904	56.6607	235.3043	15.0	43.82
acsz-z31	204.4315	56.3016	235.669	15.0	30.88
acsz-a32	206.208	56.473	236.0	15.0	17.94

acsz-b32	206.658	56.1	236.0	15.0	5.0
acsz-w32	204.4129	57.8908	234.324	15.0	69.12
acsz-x32	204.8802	57.5358	234.716	15.0	56.24
acsz-y32	205.3385	57.1792	235.1002	15.0	43.82
acsz-z32	205.788	56.821	235.4756	15.0	30.88
acsz-a33	207.537	56.975	236.0	15.0	17.94
acsz-b33	207.993	56.603	236.0	15.0	5.0
acsz-w33	205.7126	58.3917	234.2356	15.0	69.12
acsz-x33	206.1873	58.0371	234.6375	15.0	56.24
acsz-y33	206.6527	57.6808	235.0298	15.0	43.82
acsz-z33	207.1091	57.3227	235.4119	15.0	30.88
acsz-a34	208.9371	57.51237	236.0	15.0	17.94
acsz-b34	209.4	57.14	236.0	15.0	5.0
acsz-w34	206.9772	58.8804	233.4678	15.0	69.12
acsz-x34	207.4677	58.5291	233.8837	15.0	56.24
acsz-y34	207.9485	58.176	234.2919	15.0	43.82
acsz-z34	208.4198	57.8213	234.6891	15.0	30.88
acsz-a35	210.2597	58.04408	230.0	15.0	17.94
acsz-b35	210.8	57.7	230.0	15.0	5.0
acsz-w35	208.0204	59.3199	228.8144	15.0	69.12
acsz-x35	208.5715	58.9906	229.2854	15.0	56.24
acsz-y35	209.1122	58.659	229.7465	15.0	43.82
acsz-z35	209.6425	58.3252	230.1971	15.0	30.88
acsz-a36	211.3249	58.65653	218.0	15.0	17.94
acsz-b36	212.0	58.38	218.0	15.0	5.0
acsz-w36	208.5003	59.5894	215.592	15.0	69.12
acsz-x36	209.1909	59.3342	216.1822	15.0	56.24
acsz-y36	209.8711	59.0753	216.7637	15.0	43.82
acsz-z36	210.5412	58.8129	217.3327	15.0	30.88
acsz-a37	212.2505	59.272	213.71	15.0	17.94
acsz-b37	212.9519	59.0312	213.71	15.0	5.0
acsz-x37	210.1726	60.0644	213.0379	15.0	56.24
acsz-y37	210.8955	59.8251	213.6592	15.0	43.82
acsz-z37	211.6079	59.582	214.2669	15.0	30.88
acsz-a38	214.6555	60.1351	260.08	15.0	17.94

acsz-b38	214.8088	59.6927	260.08	15.0	5.0
acsz-y38	214.3737	60.9838	259.0313	15.0	43.82
acsz-z38	214.5362	60.5429	259.0313	15.0	30.88
acsz-a39	216.5607	60.248	267.04	15.0	17.94
acsz-b39	216.6068	59.7994	267.04	15.0	5.0

Table A-2. Earthquake parameters for the Kamchatka-Kuril-Japan-Izu-Mariana-Yap Subduction Zone (kisz) NOAA/PMEL unit sources (Arcas, 2015).

Unit Source Name	Longitude (°E)	Latitude (°N)	Strike (°)	Dip (°)	Depth (km)
kisz-a4	160.7926	53.1087	210.0	29.0	26.13
kisz-b4	161.3568	52.9123	210.0	25.0	5.0
kisz-a5	160.0211	52.41125	218.0	29.0	26.13
kisz-b5	160.5258	52.1694	218.0	25.0	5.0
kisz-a6	159.1272	51.70338	218.0	29.0	26.13
kisz-b6	159.6241	51.4615	218.0	25.0	5.0
kisz-a7	158.2625	50.95486	214.0	29.0	26.13
kisz-b7	158.7771	50.73519	214.0	25.0	5.0
kisz-a8	157.4712	50.24591	218.0	31.0	27.7
kisz-b8	157.9433	50.00888	218.0	27.0	5.0
kisz-a9	156.6114	49.55835	220.0	31.0	27.7
kisz-b9	157.0638	49.31087	220.0	27.0	5.0
kisz-a10	155.7294	48.8804	221.0	31.0	27.7
kisz-b10	156.169	48.62782	221.0	27.0	5.0
kisz-a11	154.8489	48.18207	219.0	31.0	27.7
kisz-b11	155.2955	47.93978	219.0	27.0	5.0
kisz-a12	153.9994	47.47286	217.0	31.0	27.7
kisz-b12	154.4701	47.23201	217.0	27.0	5.0
kisz-a13	153.2239	46.75639	218.0	31.0	27.7
kisz-b13	153.6648	46.51936	218.0	27.0	5.0
kisz-a14	152.3657	46.15145	225.0	23.0	24.54
kisz-b14	152.7855	45.8591	225.0	23.0	5.0
kisz-a15	151.4663	45.59629	233.0	25.0	23.73
kisz-b15	151.8144	45.27119	233.0	22.0	5.0